Max-Planck-Institut für Astrophysik

Steps toward a consistent NLTE treatment of the radiative transfer in Type Ia Supernovae

Daniel Nikolaus Sauer

Vollständiger Abdruck der von der Fakultät für Physik der Technischen Universität München zur Erlangung des akademischen Grades eines

Doktors der Naturwissenschaften

genehmigten Dissertation.

Vorsitzender:	Univ.-Prof. Dr. L. Oberauer
Prüfer der Dissertation:	
	1. Hon.-Prof. Dr. W. Hillebrandt
	2. Univ.-Prof. Dr. M. Lindner

Die Dissertation wurde am 21. März 2005 bei der Technischen Universität München eingereicht und durch die Fakultät für Physik am 11. Mai 2005 angenommen.

Contents

The important thing is not to stop questioning.
— Albert Einstein

1 Introduction

Since ancient times people have witnessed the appearances of bright transient phenomena that accompany the violent death of stars. These "new stars" — *novae, supernovae* — some of them bright enough to be visible even during daylight, have fascinated astronomers and scholars all over the world. Long before the advent of telescopes, reports of observations, some of which are accurate enough to allow the reconstruction of the light curve of the object (Stephenson & Green 2002, Green & Stephenson 2003), were prepared. The first modern European astronomers who reported the systematic observation of supernovae were Tycho Brahe in 1572 (Brahe 1573) and Johannes Kepler in 1604.

It was another 300 years before more serious and systematic research on supernovae was published by Ernst Hartwig. On August 20th, 1885 he first discovered a supernova outside our own galaxy in the Andromeda galaxy M31 (cf. Hartwig 1898). A measure for the tremendous brightness of this object became apparent after Lundmark (1920) estimated the distance to the Andromeda galaxy to be 7×10^5 ly: Hartwig's supernova had been several 1000 times brighter than normal novae.

The term "supernova" was actually introduced later by Baade & Zwicky (1934b) who made the first clear distinction to classical novae. Supernovae were found to be among the most powerful events in the universe — with luminosities at maximum light of $\sim 10^{42} - 10^{43}\,\mathrm{erg\,s^{-1}}$, comparable to the luminosity of an entire galaxy. The total release of energy in these events can reach values between 10^{51} to 10^{53} erg.

With only a few observations available, supernova events seemed to show only slight variation in their peak brightness and fairly similar post-maximum spectra. This led Wilson (1939) and Zwicky (1939) to consider using these extremely bright objects as distance indicators. In the following years more detailed spectral observations of different supernovae revealed that, while some objects show strong Balmer-lines in their spectra near maximum light, others do not seem to contain any visible hydrogen at all. This led Minkowski (1941) to suggest distinguishing between two different classes for these events: the objects with hydrogen spectral features are called Type II supernovae, the ones without hydrogen are referred to as Type I. However, it still remained unclear whether these objects had the same origin or if the spectral distinction reflected the presence of different physical mechanisms leading to their respective appearance.

Although Baade & Zwicky (1934b,a) and Zwicky (1939) already suggested the potentially important role of the transition of a normal star to a neutron star in supernova events, it was 1960 before Hoyle & Fowler (1960) discussed the two basic processes leading to the phenomenon of supernovae. They concluded that in Type I supernovae a star reaches a

state of high electron degeneracy that is unstable with regard to thermonuclear burning. The resulting thermonuclear explosion leads to the complete disruption of the star leaving no compact remnant. This picture has been refined by the suggestion of Truran et al. (1967) and Colgate & McKee (1969) that the light curves of these objects are primarily powered by the radioactive decay of ^{56}Ni synthesized during the explosion. On the other hand, the scenario for Type II supernovae involves a heavier star with a mass of more than about eight solar masses, which forms a core that collapses leaving a neutron star or a black hole behind. The heavier stars subject to undergo a core collapse at the end of their nuclear burning cycles generally possess extended hydrogen envelopes that form the prominent spectral features of hydrogen.

1.1 Current classification of supernovae

With the growing amount of observational data, it became clear that the two major classes were not sufficient to describe the supernova phenomenon adequately. Subsequently, more sub-classes in the two main-classes were established. A more systematic allocation to the various subclasses — in particular for Type I supernovae — was made by Wheeler & Harkness (1990). A sketch of the classification scheme is shown in Figure 1.1.

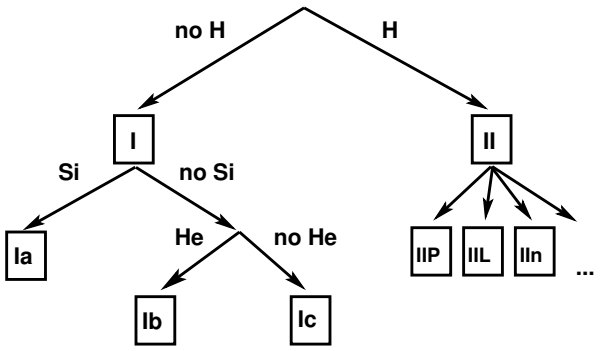

Figure 1.1: Classification scheme for supernovae.

The main classes are Type I and Type II based on whether or not the spectrum shows any hydrogen features. In the Type I class, objects without hydrogen features, a further distinction is made into the classes Ia (SN Ia), that also do not show helium but have a prominent feature of singly ionized silicon at early epochs (Si II $\lambda\lambda$6347,6371)[1]. The other Type I classes are Ib and Ic objects, where the Ib show helium features and the Ic do not. (In a sense Ic objects are those that do not fit into any other class.)

Within Type II supernovae, objects that show hydrogen in the spectrum, various objects with different characteristics concerning spectra and light curve shapes exist. The nomen-

[1] λ followed by a number denotes a wavelength in Å.

clature here mostly refers to the shape of the light curve, but is not as clearly defined as for Type I supernovae. Additionally, some objects have been observed to change their type as time proceeded (Filippenko 1988).

This supernova classification scheme relies entirely on observed features and does not take into account theoretical considerations concerning different explosion mechanisms. More details on the spectral properties of the various sub-classes can be found, for instance, in Filippenko (1997).

From the theory side, supernovae are now distinguished into two fundamentally different types of explosions. For Type Ia Supernovae, the generally agreed upon framework is the thermonuclear explosion of a white dwarf (WD) with a low mass close to the Chandrasekhar mass of $M_{\mathrm{Ch}} \approx 1.4 M_{\odot}$. The explosion does not leave any compact object behind.

All other objects — Type II and Ib/c — are thought to be formed by the collapse of the compact iron core of a highly evolved star with larger mass. The differences in appearance of these objects are primarily due to different evolution histories of the progenitor stars. Depending on previous mass losses or accretion from a binary companion, the stars have different composition in the outer layers, which are ejected in the supernova explosion. In this framework, the objects that do not show hydrogen or helium, empirically assigned to Type I, originate from stars that have lost their outer envelopes in previous outbursts or nova explosions (Nomoto et al. 1995).

Recently, several high energetic Type Ic supernovae, sometimes referred to as "Hypernovae," have been observed in the context of the afterglow of long Gamma-ray-bursts (GRB), which provides strong evidence for a connection between core-collapse supernovae and GRBs (see for instance Iwamoto et al. 1998, Mészáros 2003).

1.2 Astrophysical relevance of SN Ia

The primary emphasis of this work was to investigate radiative transport in SN Ia envelopes, although the concepts are applicable to any kind of supernova. This section will therefore focus on the role of this class of supernovae in an astrophysical context.

The rising interest in SN Ia-science during the last decade is due to a number of reasons. In spite of the substantial progress made in both observational and theoretical aspects, many questions concerning the physical mechanisms are still unanswered. So far, there is not a complete picture of the evolution of the progenitor star through the explosion to the late time post-explosion era of SN Ia. In particular, the open questions concern the nature of the progenitors, their pre-explosion evolution, and the exact mechanism of the explosion (see Section 2).

Stellar evolution and metal enrichment of the universe

SN Ia interact with their environment and influence the evolution and appearance of galaxies and the interstellar medium. Leibundgut (2000) has summarized some of the effects that make SN Ia astrophysically important objects. First, SN Ia are thought to be the main producer of iron in the universe and can therefore be used as a clock for the metal[2] enrichment of matter in the universe. The relatively long lifetimes of SN Ia progenitor stars compared to the much more massive — and therefore short-lived — progenitors of core-collapse supernovae result in a distinct relationship between α-elements and iron-group-elements; this allows estimates of the rates of supernovae in the past history of the universe (Renzini 1999). The energy released in SN Ia plays an important role in the heating of the interstellar medium, specifically in elliptical galaxies (Ciotti et al. 1991).

Since SN Ia form the endpoint of a major stellar evolution channel, they provide important information on binary fraction of stars and the evolution of binary systems in our galaxy and, as a function of look-back time, the evolution of binary systems in the history of the universe (Iben & Tutukov 1994, 1999, Ruiz-Lapuente & Canal 1998). SN Ia, together with other types of supernovae, also play an important role in the early evolution of galaxies by influencing the star formation rate and removal of gas from galaxies (see for instance Burkert & Ruiz-Lapuente 1997, Ferrara & Tolstoy 2000).

Type Ia supernovae as lighthouses for cosmology

The most spectacular application of SN Ia in recent years has been their use for distance measurements in cosmology. The findings of two independent groups investigating SN Ia up to redshifts[3] $z \sim 1$ (Riess et al. 1998, Perlmutter et al. 1999) suggest that the expansion of the universe is accelerating. A review on the cosmological implications from SN Ia-data can be found in Leibundgut (2001).

The findings employ the fact that SN Ia can be used as "standard candles," that is, bright objects of known luminosity, which allow one to conclude on the distance between object and the observer by measuring the object's apparent luminosity. Although the original hypothesis that SN Ia are perfect standard candles (i.e., all SN Ia have the same luminosity at a given epoch) did not hold as more and better data became available, it nevertheless turned out that it is possible to "standardize" the peak brightness. This can be done using empirical relationships between observed features that are independent of distance, e.g., the shape of the light curve and the absolute luminosity (Phillips 1993, Hamuy et al. 1996b, Riess et al. 1996, Perlmutter et al. 1997). An essential key to firmly establish these relationships was provided by the large and very homogeneous data sets of multifilter light curves of the Calán/Tololo search (Hamuy et al. 1996a) and the Harvard-Smithonian Cen-

[2] In astrophysics commonly all elements heavier than He are called metals.

[3] The redshift z corresponds to the amount of energy that a photon traveling through space has lost due to the expansion of the universe. It is commonly used as a distance measure.

ter for Astrophysics (CfA) (Riess et al. 1999b). Nearby objects in these searches were used to determine the necessary corrections to the light curve shapes. Using these corrections, the local objects ($z \lesssim 0.1$) precisely follow a straight line in the Hubble-diagram, which gives the relationship between the distance in redshift versus the apparent brightness of an object of known absolute brightness.

The standard model of cosmology[4] is based on two assumptions: on large scales the universe is isotropic and homogeneous (this is referred to as the "cosmological principle"). The line element distances between two objects with the comoving spatial coordinates r, θ and time t is described by the Robertson-Walker-metric

$$ds^2 = dt^2 - a^2(t)\left(\frac{dr^2}{1-kr^2} + r^2 d\theta^2 + r^2 \sin^2\theta \, d\phi^2\right). \tag{1.1}$$

Given a simple topology, the curvature term k takes the values $-1, 0, 1$ for an open, flat, or closed universe, respectively. The dynamic evolution is determined by the scale factor $a(t)$, which describes the radius of curvature of the universe over time. Using this metric, the Friedmann equation follows from the $(0, 0)$ component of Einstein's field equations by adopting the energy momentum tensor of an ideal fluid:

$$H^2 := \left(\frac{\dot{a}}{a}\right)^2 = \frac{8\pi}{3} G\rho - \frac{k}{a^2} \tag{1.2}$$

where G is Newton's gravitational constant and ρ is the total energy density of the universe. This defines the Hubble-parameter H describing the expansion rate. In terms of the Hubble-parameter, the Friedman equation can be rewritten as

$$\frac{k}{H^2 a^2} = \frac{\rho}{3H^2/8\pi G} - 1 = \Omega - 1 \tag{1.3}$$

introducing the ratio of density ρ to critical density $\rho_c := \frac{3H^2}{8\pi G}$. Thus, a flat universe with $k = 0$ has $\Omega = 1$. Assuming that the universe is composed of different components contributing to the total energy density, each component has the fraction

$$\Omega_i = \frac{\rho_i}{3H^2/8\pi G} \tag{1.4}$$

of the critical density and an equation of state relating density ρ_i and pressure p_i by $w_i = p_i/\rho_i$. The equation of state parameter w_i is 0 for normal matter and $\frac{1}{3}$ for photons. From these equations one can derive an expression for the luminosity distance D_L defined as the apparent brightness of an object as a function of redshift. Taking into account all effects of time dilation and energy decrease due to the cosmological redshift, a numerically

[4] More details on cosmological models with a cosmological constant can be found in, for example, Carroll et al. (1992). An extensive article on cosmology with supernovae can be found in Perlmutter & Schmidt (2003).

integrable equation can be derived (see Carroll et al. 1992, Leibundgut 2001). Considering only terms up to the second order in z gives

$$D_L = \frac{c}{H_0}\left(z + z^2\tfrac{1}{2}(1 - q_0) + O(z^3)\right) \tag{1.5}$$

with the Hubble constant at present H_0 and the "deceleration parameter"

$$q_0 = \tfrac{1}{2}\sum_i \Omega_i(1 + 3w_i). \tag{1.6}$$

From Eq. (1.5) it can be seen that in the nearby universe, D_L scales linearly with redshift, while in the more distant universe, q_0 introduces a dependence on the amount and the properties of the matter in the universe.

The surprising result that the expansion of the universe accelerates is based on the finding that supernovae at high redshifts appear to be dimmer than their nearby counterparts. In the cosmological standard model, this accelerated expansion can only be achieved by introducing an energy species that has $w_i < 0$ (i.e., a negative pressure), referred to as "Dark Energy" or the cosmological constant[5] Λ (Weinberg 1989, Carroll et al. 1992). Tonry et al. (2003) compiled the latest results of the observation of 172 SN Ia by the High-z Supernova Search Team (Schmidt et al. 1998). In Figure 1.2, the left panel shows the apparent luminosities versus redshift in a residual Hubble diagram where an empty universe ($\Omega_M = 0$ and $\Omega_\Lambda = 0$) has been subtracted. The filled black dots represent binned median values for clarity. The solid curves represent the expected dependence for a flat universe with $\Omega_M = 0.1$, $\Omega_\Lambda = 0.7$ (top line), an open universe ($\Omega_M = 0.3$, $\Omega_\Lambda = 0$), and an Einstein-de Sitter universe ($\Omega_M = 1.0$, $\Omega_\Lambda = 0$, bottom line). The right panel in Figure 1.2 shows the confidence contours for the combination of values for Ω_M and Ω_Λ. The bigger, darker ellipses represent the supernova data alone; the smaller contours result from additional constraints based on results from the large-scale structure Two Degree Field (2dF) Redshift Survey (Percival et al. 2001). Values for cosmological parameters derived from the measurement of the cosmic microwave background anisotropy by the Wilkinson Microwave Anisotropy Probe (WMAP) (Spergel et al. 2003) are also consistent with the supernova data. By combining the results of the various methods, the fractions of matter density and dark energy are currently determined to be $\Omega_M = 0.3$ and $\Omega_\Lambda = 0.7$.

Because the conclusions drawn from these results are serious enough to question well-established theories in cosmology, alternatives to explain the dimming of SN Ia at high redshifts also have to be considered. In Leibundgut (2001) some concerns are discussed in more detail. For instance the dimming could be explained by absorption due to some "grey" dust (i.e., dust absorption that does not have a significant impact on the spectral appearance of SN Ia (Aguirre 1999)) or one could think of attenuation of light due to gravitational lensing effects. Another explanation could be variation in the explosion mechanism

[5] This depends on the point of view whether the additional term in Eq. (1.2) is contributed to the metric or the energy momentum tensor. It is also not necessary to keep it a constant contribution in time, which leads to the so called Quintessence cosmological models (Caldwell et al. 1998).

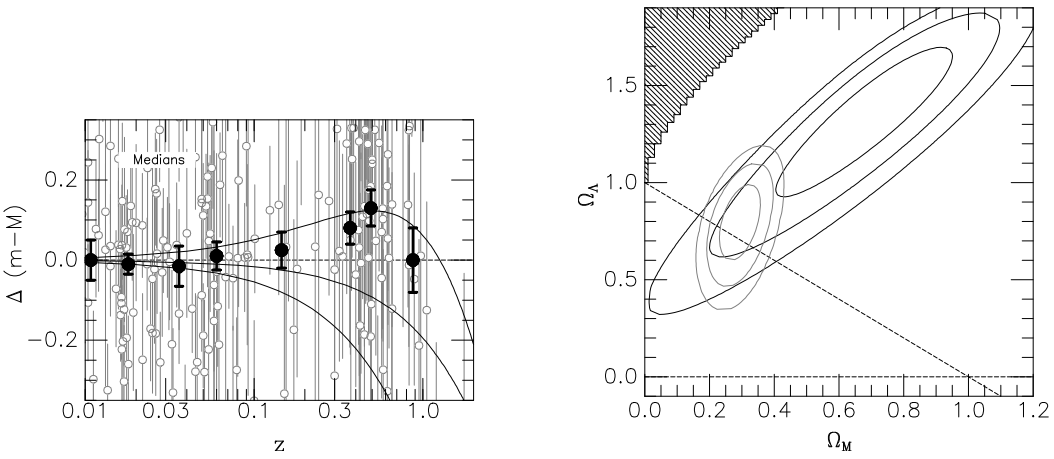

Figure 1.2: *Left:* SN Ia luminosities (relative to the Hubble diagram of an empty universe) versus redshift. The filled black dots mark binned median values for a better overview. *Right:* Confidence contours for combinations of Ω_M and Ω_Λ from SN Ia data alone (bigger ellipses) and together with the prior from the 2dF survey (Percival et al. 2001). (Figures from Tonry et al. (2003).)

due to a different metallicity of the environment in earlier stages of the universe leading to a different light curve shape (see also Röpke & Hillebrandt (2004)). None of these effects can be ruled out entirely; however, all would become more serious with higher redshift, which conflicts with the evidence found by Riess et al. (2004) that at higher redshifts $z \gtrsim 1$, supernovae become relatively brighter again. This hints at an epoch of deceleration as predicted by the cosmological models and could provide a clear sign that the dimming is in fact due to the expansion history of the universe.

Besides these concerns, one should keep in mind that these results rely on the purely empirical correlation between light curve shapes and absolute luminosities. Even though these relationships are well established, the different correction methods are not consistent (Leibundgut 2004). In addition, the observed colors at peak brightness seem to be different for nearby SN Ia compared to distant ones (Leibundgut 2001). This emphasizes the necessity to confirm the normalization methods using a theoretical framework based on a profound understanding of the physics of SN Ia. Only with a theoretical understanding of the details of the explosion mechanism and the processes which lead to the observed properties of SN Ia can potential systematic errors in the luminosity calibration techniques be minimized.

1.3 Objectives of this work

The complexity of the physics involved in supernova explosions generally make it difficult to obtain a consistent picture of all aspects of the problem. The problems that have to be

addressed range from the evolution of the progenitor systems, to the explosion hydrodynamics including all relevant nucleosynthesis reactions, to the generation and transport of radiative energy in the ejected matter that can be directly compared to observations.

The need to understand more details of the physical processes in SN Ia, in particular, is emphasized by the impact of the results mentioned in the previous section; these results rely on the assumption that nearby SN Ia have similar properties to distant SN Ia, which cannot be observed in detail. In addition, the distant objects are highly red-shifted such that the wavelength bands do not coincide with local observations anymore. In particular, the rest-frame UV part of the spectrum, which becomes visible in the optical and infrared range, is not explored in detail due to the absence of systematic observations of nearby objects in the UV range, which cannot be taken from the ground.

An international collaboration called the SN-factory (Aldering et al. 2002) launched an extensive observational program that has been taking data since 2004 with the goal of minimizing the statistical errors in the determination of cosmological parameters by increasing the number of low-redshift supernova observed. Because the hydrodynamic explosion models have been improved in recent years to a level of predictive power, the *European Supernova Collaboration (ESC)*, funded by the Research Training Network *"The Physics of Type Ia Supernovae"* of the European Union, was established in 2002. This collaboration focuses on only a few nearby objects, but aims to provide very high quality photometric and spectroscopic data with comprehensive coverage over all epochs. A special emphasis has been put on the very early epochs, just a few days after explosion, because the outermost layers, which carry important information for constraints on the progenitor system, are only visible at that time. Recently, Stehle et al. (2004) performed an extensive analysis of the spectral data gathered by the ESC using a fast, but approximate, description of the radiative transfer. Linking the established hydrodynamic explosion models to the light curves and spectra observed by the ESC, however, requires a fully consistent radiative transfer model that covers all relevant physics.

In the long term, the current project aims to set up a radiative transfer model that takes into account the details of the full non-equilibrium physics. This will allow us to achieve the following objectives:

- Perform quantitative analysis of observed supernova spectra to obtain physical parameters such as temperatures and element abundances

- Investigate the impact of variation of physical parameters on observed spectral features to provide observational tools that can be used to determine the physical conditions in supernovae (in particular with respect to relationships that can be used to calibrate the peak brightness of SN Ia)

- Provide reliable predictions of how properties of different theoretical explosion models affect the observed spectral features (in particular to analyze the outcome of the explosion models for Type Ia (Reinecke et al. 2002a,b, Röpke & Hillebrandt 2005),

but also Type II supernovae (Kifonidis et al. 2003, Scheck et al. 2004), computed at the Max-Planck-Institute for Astrophysics in recent years)

- Judge the quality of the approximations used by Stehle et al. (2004) in their fast method to avoid an overinterpretation of the results and provide additional improvements to the approximations for a physically more correct description without losing the advantage of a very fast analysis

The current work provides the basic steps toward incorporating the supernova-relevant physics into the WM-basic stellar atmosphere code of Pauldrach et al. (2001). To achieve a consistent description of the radiative transfer in supernovae, this stellar atmosphere code, developed at the Universitätssternwarte München to analyze the spectra of hot stars with radiatively driven winds (see Pauldrach 2003, and references therein), has been adapted to the physical conditions in expanding supernova envelopes. This code provides a solution of the radiative transfer in the observer's frame using an opacity sampling technique to obtain a good starting condition; the final iterations are performed on the basis of an exact (but computationally more expensive) solution of the radiative transfer in observer's frame. This method is entirely equivalent to the comoving frame solution employed by other codes. Due to the pre-iteration, however, our method is significantly less resource-intensive and takes only a fraction of the computational time on a single processor machine. In spite of the steadily increasing computer power, a full comoving-frame calculation still requires a significant amount of time and the use of such methods for a systematic analysis of the growing amount of supernova data, spectra, and light curves is limited.

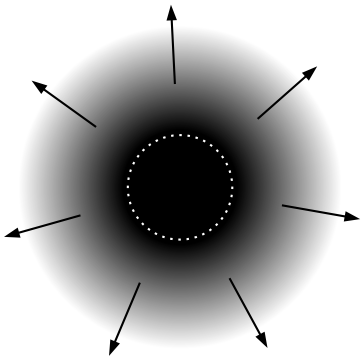

Figure 1.3: Illustration of the photospheric assumption for the calculation of supernova spectra in early epochs. The dotted circle indicates the "photosphere" where the pseudo-continuum becomes optically thick.

Most current approaches for spectral synthesis of SN Ia at early epochs treat the supernova ejecta as a photosphere with a superimposed expanding atmosphere (see Figure 1.3). (A photosphere is usually defined as the radius at which a certain mean optical depth is reached.) In this way, the supernova model can use techniques known from stellar atmosphere modeling and be solved in a steady-state approximation by calculating "snap-shots" of a certain epoch. As will be discussed in detail later, the assumption of a photosphere is problematic because, in contrast to stellar atmospheres where the photosphere is formed

by an optically thick continuum, the line opacity of SN Ia greatly dominates over continuum opacity in most parts of the spectrum. Consequently, the SN Ia photosphere is formed by a "pseudo-continuum" of a large number of overlapping metal lines. In contrast to stellar photospheres, the radial location of this "pseudo-photosphere" is strongly frequency-dependent. This fact, however, makes it more difficult to set the boundary of the region of the ejecta, which is explicitly treated in the radiative transfer. In the worst case, the choice of an unphysical boundary condition leads to spurious results in the synthetic spectrum in wavelength regions where the approximation breaks down (Stehle 2004). This problem becomes more serious in later epochs of the object under consideration. Therefore, one goal of the current work is to provide a theoretical framework for a boundary approximation that is more consistent with the physical conditions under consideration.

Another issue addressed in this work is the solution of radiative transfer with a Doppler-broadened opacity sampling technique for situations where the line opacities dominate over the continuum throughout the entire atmosphere and the continuum itself does not accumulate sufficient optical depth. This technique is used in our models as the starting point for the exact calculation. The general problem is that the envelope becomes locally optically thick at a frequency where a line transition is present, but is optically thin at adjacent frequencies where no or only weak line transitions occur. Even in the spatial regions of the "pseudo-photosphere" the spatio-frequencial behavior is still locally influenced by the radially varying frequencial Doppler-shift of the line opacities. Thus, the mitigating circumstances of stellar atmospheres — an optically thick continuum with Doppler-shifts approaching zero in the photosphere — unfortunately do not apply to supernova atmospheres. These conditions require an improved method for the radiative transfer solution because the standard scheme has not yet been suitable for the adverse behavior of the opacity as a function of radius and frequency in supernova atmospheres.

Organization of this thesis

This work is organized as follows. Chapter 2 gives an overview of the observational and theoretical status of SN Ia science. The general observed properties are discussed followed by an outline of theoretical explosion models and radiative transfer models. In Chapter 3 the fundamental theoretical concepts of radiative transfer in stellar atmospheres are introduced. In Chapter 4 the numerical concepts employed in the code used in this work are explained in more detail. In Chapter 5 the supernova-specific modifications are discussed. In particular, an improved theoretical concept for the inner boundary of radiative transfer in SN Ia is discussed. As a first application, studies of the explosion models recently computed at the Max-Planck-Institute for Astrophysics are described in Chapter 6. Chapter 7 provides a summary of the work and an outlook on future work.

2 Observational and theoretical aspects of supernovae

This chapter gives a brief outline of the current status of SN Ia science. First, the observed properties of these objects are considered. An overview of the theoretical models for the explosion mechanism is given and possible explanations for observed properties are discussed. For more detailed descriptions of the observations see, for instance, Filippenko (1997) and Leibundgut (2000). An overview of the theoretical concepts can be found in Hillebrandt & Niemeyer (2000).

2.1 Observed properties of SN Ia

Overall SN Ia form a fairly uniform group of objects with very similar properties. The increasing amount of observational data gathered in the last decade showed, however, that within this overall homogeneity there is significant variation among different objects.

Light curves

Observation of light curves in different bandpass filters provides essential information on the energetics of supernovae at different epochs. Figure 2.1 shows a schematic picture of *B*-band light curves of different supernova types. Generally, Type I Supernovae have light curves showing a steep increase to peak luminosity followed by a steep decline that eventually turns into a slower exponential decline at late epochs. Type II-L Supernovae (L for linear) also show a roughly exponential decline law after maximum, however, slower than Type I Supernovae. Type II-P events (P for plateau) tend to stay at almost peak luminosity for a few months before declining at later times. Also indicated in Figure 2.1 is the light curve of SN1987A, a peculiar Type II Supernova that exploded in the Large Magellanic Cloud (LMC). It is currently the best studied supernova due to the proximity of the event.

SN Ia have distinct light curves that are similar in most objects. They show a fast rise to maximum within about 18 to 20 days in *B*-band. Overall most SN Ia seem to reach their maximum light in redder filter bands somewhat earlier than in the *B*-band, although there are exceptions, such as SN1991bg (Contardo et al. 2000). Initially after maximum, a steeper decline occurs that is followed by a second maximum in *I* and redder light curves

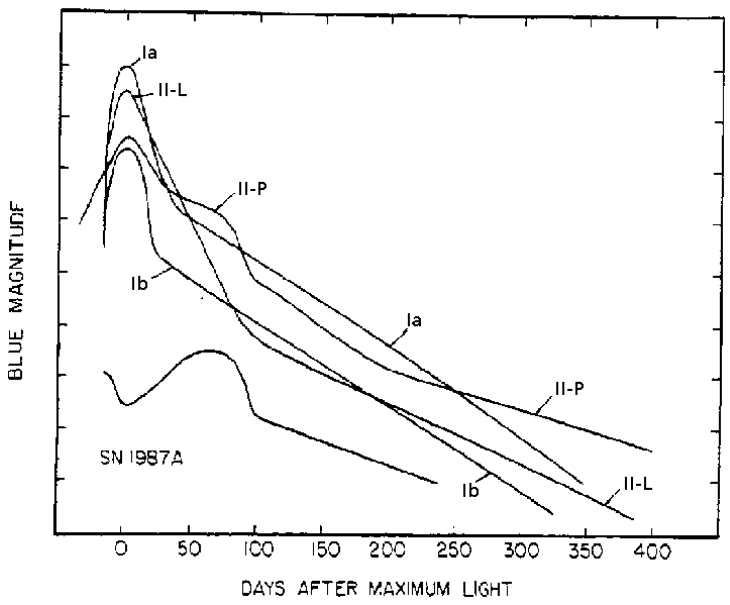

Figure 2.1: Schematic light curves of different types of supernovae (from Wheeler & Harkness (1990))

(Suntzeff 1996, Meikle 2000). This second maximum is pronounced differently in different objects and filters. After about 50 days, the light curves of most SN Ia become very similar and follow a steady exponential decline in luminosity (Leibundgut 2000). Observers usually refer to the maximum point of the light curve in *B*-band as the zero point, while theorists usually use the time of the explosion as the zero point. (The explosion time, however, cannot be observed directly.) As an example, Figure 2.2 shows the light curves of SN2003er in different filters (Pignata et al. 2004).

For physical applications, it is important to know the total flux of all wavelength bands at a given epoch. The total flux is provided by bolometric light curves. Considering the very different characteristics in different wavelength bands, the bolometric light curves are not directly accessible. Usually bolometric light curves are considered to be the sum over the wavelength bands from near-UV to IR (they are called UVOIR), which explicitly excludes the contribution of emerging γ-rays to the energetics (Vacca & Leibundgut 1996, Turatto et al. 1996, Contardo et al. 2000)

The peak brightness is an important quantity for the analysis and, in particular, for the application of SN Ia as distance indicators. For SN Ia overall, the peak brightness scatters very little (about 0.5 magnitudes in the *B* and *V* bands) even before corrections are applied (Leibundgut 2000). A typical bolometric luminosity at maximum light is $10^{43}\,\mathrm{erg\,s^{-1}}$ with a range from $\sim 2\times10^{42}\mathrm{erg\,s^{-1}}$ for faint objects (1991bg-like) to $> 2\times10^{43}\,\mathrm{erg\,s^{-1}}$ for bright ones (1991T-like) (Contardo et al. 2000).

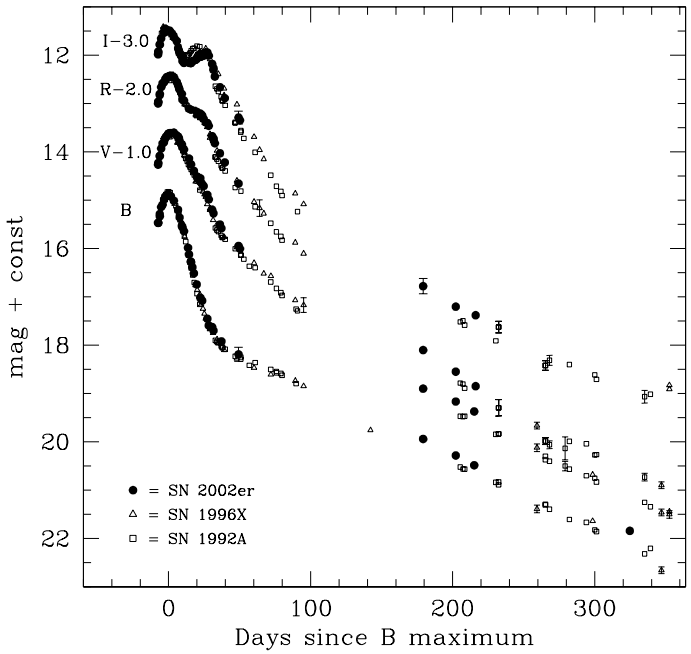

Figure 2.2: Light curve of SN2003er in different passband filters in comparison to the corresponding light curves of SN1996X (Salvo et al. 2001) and SN1992A (Suntzeff 1996) (from Pignata et al. 2004).

Spectra

As already mentioned in Section 1.1, the spectral features, in particular the appearance of H lines, are the main criterion used to distinguish between different types of supernovae. Figure 2.3 shows characteristic spectra of different types of supernovae near maximum. The most important line identifications used for classification are indicated.

In early epochs, supernova spectra are characterized by strong and broad absorption features that typically show significant P-Cygni profiles[1]. The evolution of the spectra is characterized by the changing influence of the various absorption and emission features. In the pre-maximum phase, the spectra of SN Ia are dominated by strong absorption features of singly ionized intermediate mass elements such as oxygen, silicon, and sulfur. Most

[1] P-Cygni profiles are features that consist of a, relative to the rest-wavelength, blue-shifted absorption trough and a red-shifted emission peak. They are formed if strong lines occur in an optically thin region of a fast expanding atmosphere. The absorption in the underlying continuum is caused by the opacity in the material that moves toward the observer, while the emission comes from material on the opposite side that moves away from the observer. This was first observed in stars with expanding atmospheres, such as P-Cygni after which the effect is named.

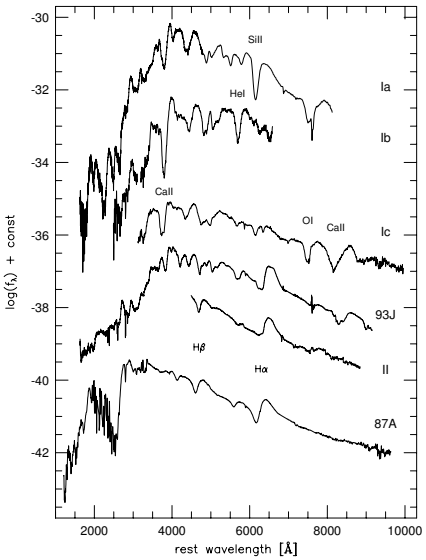

Figure 2.3: Near maximum spectra for different types of supernovae (Wheeler & Benetti 2000)

prominent here is the Si II doublet $\lambda 6347, 6371$ that causes the characteristic deep absorption feature at ~ 6100 Å. Other important lines include the Ca II lines at $\lambda\lambda 3934, 3968$ and $\lambda 8579$, Mg II $\lambda 4481$, S II $\lambda\lambda 5468, 5612, 5654$ and O I $\lambda 7773$. Near maximum the densely clustered lines from iron-group elements become more and more prominent and, after about 2 weeks after maximum light, dominate the spectrum. At this point the spectrum starts to gradually change into an emission line spectrum. Around one month after maximum, the supernova enters the nebular phase where the continuum entirely vanishes and the spectrum shows classical nebular lines from forbidden line transitions.

In the nebular phase, one can see that the relative line strengths of [Co III] to [Fe III] lines decrease following the half-life of the radioactive decay ^{56}Co$\rightarrow^{56}$Fe (Kuchner et al. 1994). This observation and the fact that the late light curve also follows this decay law confirms the hypothesis that virtually all radiative energy emitted by SNe Ia is produced by the radioactive decay ^{56}Ni$\rightarrow^{56}$Co$\rightarrow^{56}$Fe (Colgate & McKee 1969).

All lines show strong Doppler-shifts indicating that the ejected material travels at high velocities. From relatively unblended lines, one can deduce velocities of up to 20 000 km s^{-1} while most lines lay between 10 000 and 15 000 km s^{-1} (Branch et al. 1982). It is also characteristic that different lines have different velocities and are hence formed at different depths in the ejecta.

The other two Type I objects, Type Ib/c Supernovae, do not show the prominent Si II $\lambda\lambda 6347, 6371$ feature. The distiction between Ib and Ic objects is based on the presence of optical He I lines, in particular He I $\lambda 5876$. At late times Ib/c spectra, in contrast to SN Ia spectra, show only a few iron-group lines, but relatively unblended emissions of

intermediate mass elements.

The early time spectra of SN II show prominent H II features with a wide range of variation for the strengths especially for the Hα line. This line keeps dominating until late times, while the rest of the spectrum is similar to Ib/c spectra, but with narrower lines. In general, Type II spectra show significant heterogeneity among different events.

As an example of a very well covered sequence of SN Ia spectra, Figure 2.4 shows the spectral evolution of SN2003du (Stanishev 2005). It clearly shows the Si II absorption feature at $\sim$ 6100, which shifts from blue to red with time as the region where the line is formed recedes to lower velocities deeper inside the ejecta.

In the UV range, the spectra of different types of supernovae show significant differences. Due to strong line blocking of iron-group elements (mostly Fe II and Co II lines) all Type I supernovae show a strong lack of flux compared to a thermal spectrum.

In SN Ia the flux in the infrared part of the spectrum is also diminished while Ib/c spectra closely follow a black-body spectrum in that range.

Empirical relations for luminosity calibration of SN Ia

Up to the end of the 1980s, SN Ia were thought to be fairly perfect standard candles, i.e., all have the same peak luminosity. With more detailed observational programs it became clear that there is variation within this homogeneous group. With systematic analysis of observational data, however, various observed properties have been found to correlate with the peak luminosity of the light curve. Thus, based on entirely empirical correlations, it is possible to obtain information on the absolute brightness and retain the use of SN Ia as standard candles. Most important is the correlation between the linear decline rate versus luminosity (Phillips 1993), that has been used in a variety of approaches including the Δm_{15} method (Hamuy et al. 1996b, Phillips et al. 1999), the multi-color-light curve shape corrections (Riess et al. 1996, 1998), and the stretch factor (Perlmutter et al. 1997). All these corrections employ different parameterizations of the light curve shape and are based on the fact that SN Ia observed in the Hubble flow generate a better fit to the Hubble line in the Hubble diagram.

Other parameters that correlate to the luminosity include the rise time to maximum light (Riess et al. 1999a), line strengths of prominent absorption features (Nugent et al. 1995b, Riess et al. 1998), velocities of line features (Mazzali et al. 1998, Benetti et al. 2004), and properties of the host galaxy (e.g., Filippenko 1989, Hamuy et al. 1996a, Branch et al. 1996, Schmidt et al. 1998)

It should be mentioned that the empirical methods for calibration of the peak brightness reproduce partly significantly different results. In particular the assumptions on correction for dust within the host galaxy of the supernova (Leibundgut 2000) are critical. Most of these empirical relations still miss a clear theoretical explanation that could help to exclude potentially wrong conclusions.

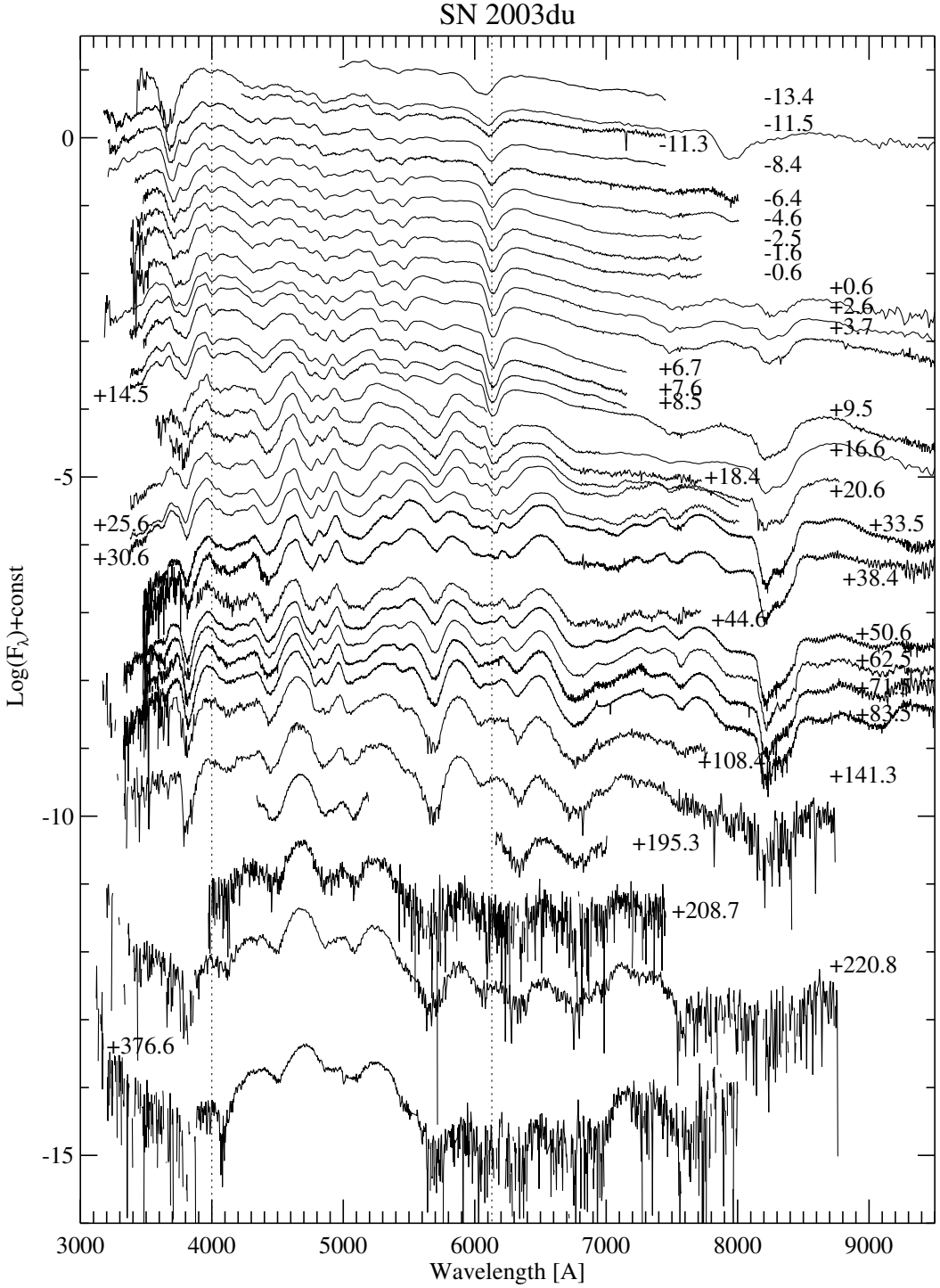

Figure 2.4: Sequence of optical spectra of SN2003du. The spectra are vertically shifted by an arbitrary amount. The numbers at the individual spectra refer to the epoch before and after maximum light. (Stanishev 2005).

2.2 Theoretical models for SN Ia explosions

This section gives a brief outline of theoretical supernova models. The progenitor scenarios and current models for the hydrodynamics of the explosion are introduced as this forms the basic ingredient of the radiative transport models. (For a review on explosion models see e.g., Hillebrandt & Niemeyer (2000).) Then the radiative transfer models for light curves and spectra are discussed.

2.2.1 Progenitor scenarios

The question of the progenitors of SN Ia is still a controversial topic. Differences in the progenitors may be the key to the observed diversity of Type Ia Supernovae (see, e.g., Nomoto et al. 2003, Röpke & Hillebrandt 2004). A solution to these longstanding issues is important for several reasons. One reason is to determine the conditions leading to the ignition of the thermonuclear burning, which is needed to constrain the initial conditions for realistic explosion models.

The major problems in determining the correct scenario — or scenarios — are that SN Ia are rare events and the white dwarfs proposed as the most likely progenitors are faint objects with long evolutionary time scales of several Gyrs. This makes it very difficult to address the open questions directly with observations. Instead, indirect measurements and hints in spectra and light curves have to be used. For extensive reviews of this topic, refer to Nomoto et al. (1994), Branch et al. (1995), and Livio (2000).

Type Ia Supernovae generally appear in spiral arms as well as elliptical galaxies, with a weak indication that they might be more frequent in young stellar populations (Bartunov et al. 1994). The fact that SN Ia occur in elliptical galaxies rules out more massive stars as potential progenitors. There seems to be a correlation, however, between the peculiar, non-standard events and the galaxy type (Hamuy et al. 1996a), which may indicate the possibility that more than one progenitor scenario is required to explain the phenomenon.

Single lower-mass stars usually blow off their outer envelopes by strong winds forming a planetary nebula. The remaining WD does not have the possibility for further evolution and will slowly cool down. The absence of X-ray emission in remnants of SN Ia exclude a connection to neutron stars or black holes. The lack of hydrogen and helium, the most abundant elements in the universe, hints strongly toward a star that disposed of most of its envelope in previous outbursts. The currently favored scenarios involve a white dwarf in a binary system that slowly accrets mass.

The constraints on the composition of the white dwarf come from nucleosynthesis considerations and the abundance of the object itself comes from stellar evolution arguments. Various possibilities have been discussed. The most likely candidates are C–O white dwarfs with masses close to the Chandrasekhar mass ($M_{\mathrm{Ch}} \approx 1.4\,M_{\odot}$). The thermonuclear explosion of these objects releases about 10^{51}erg of energy.

The appealing aspect of this scenario is that the Chandrasekhar mass provides an almost natural explanation for the observed homogeneity of SN Ia. Slight variations in that scheme may account for peculiar events. Other possibilities that are not ruled out yet include sub-Chandrasekhar mass WDs, which may also be an explanation for a certain class of peculiar objects. In this scenario a WD well below M_{Ch} accrets helium from a companion star until a shell of $\sim 0.3\,M_{\odot}$ has been accumulated on top of the C–O core. The He layer is then ignited and triggers an off-center explosion of the C–O core (Arnett 1996). Other possible configurations, usually discussed in the context of M_{Ch} C–O WDs, are close binary systems consisting of two low-mass WDs that approach each other due to the loss of energy by gravitational wave radiation (referred to as the "double degenerate" scenario) (Iben & Tutukov 1984, Webbink 1984, Woosley et al. 2004). One of the stars eventually breaks up and forms an accretion disc around the other star, which eventually exceeds M_{Ch} (Benz et al. 1990, Mochkovitch et al. 1997). The advantage of this configuration is the complete absence of hydrogen in the system. Observationally, however, most systems that can merge within a Hubble time do not have enough mass to reach M_{Ch} (Livio 2000). Also it is unclear how this class of progenitors would be able to reproduce the homogeneity of SN Ia because the two merging stars are unlikely to have similar masses. Moreover it has been argued that the most likely outcome of this scenario is a O–Ne–Mg WD that would collapse further to a neutron star (see, e.g., Nomoto & Iben 1985, Woosley & Weaver 1986); this probably rules out the occurrence of a standard SN Ia.

The most widely accepted model for normal SN Ia is the single degenerate scenario where a WD accretes hydrogen-rich material from a main-sequence star, until it reaches M_{Ch}. Peculiar events occur due to variations in the evolutionary history of the system. The most serious problem in this scenario is that the accretion process has to proceed within a very small range of accretion rates to avoid He-flashes that decrease the accreted mass (Nomoto 1982b, Nomoto & Kondo 1991). After a few thousand years of slow and quiet burning, temperature fluctuations near the center of the WD trigger an explosive carbon burning, which evolves into a thermonuclear runaway that eventually disrupts the entire WD (Whelan & Iben 1973, Nomoto 1982a, Han & Podsiadlowski 2004). Observational support for this scenario comes from the recently identified companion star of Tycho's supernova SN1572 (Ruiz-Lapuente et al. 2004).

Potential progenitor systems have been found in recent years; their numbers, however, are too low to explain the observed rates of SN Ia (Cappellaro et al. 1999). (Although, recently Pauldrach et al. (2004) suggested a potential connection to the central stars of planetary nebulae.)

2.2.2 Explosion hydrodynamics in SN Ia

The fundamental theoretical questions concerning the explosions of SN Ia need to explain the general appearance of these events, in particular, the observed homogeneity, but also the intrinsic variability. What are the progenitor stars, how do they evolve to become a

SN Ia and what is the explosion mechanism? How are the observed characteristics formed? In particular, how reliable are the empirical relations used to calibrate the luminosity? To shed light on these questions, extensive numerical models of the hydrodynamics of the explosions, the evolution of potential progenitor stars, and the transport of radiation through the expanding ejected material are carried out. The models are constrained by the observed properties of SN Ia including element abundances, explosion energetics, explosion rates, the overall homogeneity, and variability. The goal is to obtain models from physical arguments that contain as few non-physical parameters as possible.

The currently most accepted scenario is the thermonuclear explosion of a C–O white dwarf (Woosley et al. 1986, and references therein). At first the contracting core of the WD undergoes a phase of slow carbon burning while it becomes convectively unstable. This causes temperature fluctuation to grow and locally reach run-away conditions. This ignites a thermonuclear burning front of explosive carbon burning that travels outwards as a sub-sonic deflagration wave and disrupts the star entirely. The explosion has to proceed sub-sonicly through most of the WD; supersonic burning (detonation) is known to produce a smaller fraction of intermediate mass elements than is required because the high densities and temperatures favor the generation of iron group elements. Citing observational constraints, some authors argue that the deflagration front has to turn into a detonation as it reaches the outer layers (delayed detonation) to sweep up remaining unburned material and to obtain the observed explosion energies (e.g., Livne & Arnett 1993, Höflich et al. 2004). The physical processes, however, that should trigger such a deflagration-detonation-transition (DDT) are unclear. The C–O WD scenario is only one possible model and it still has problems explaining all observed properties. It is also imaginable that more than one mechanism is involved. For instance sub-Chandrasekhar-models, where the ignition is triggered by some external event, could account for some of the sub-luminous 1991bg-like events.

The phenomenological 1d-deflagration model W7 (Nomoto et al. 1984, Thielemann et al. 1986) and similar models by Woosley & Weaver (1994) have been shown to reproduce the observed element abundance distributions and velocities fairly accurately. In 1-dimensional models, however, the burning speed is a free parameter that cannot be explained from physical arguments; it is determined from turbulence in the fluid, which is intrinsically 3-dimensional.

For a few years, three-dimensional explosion models have been developed by different groups (Reinecke et al. 2002a,b, Gamezo et al. 2003, 2004, Röpke & Hillebrandt 2005). In the group at Max-Planck-Institute for Astrophysics (MPA) (Reinecke et al. 2002a,b, Röpke & Hillebrandt 2005) special emphasis was put on setting up a detailed sub-grid model for the turbulent flame speed, that was used in the large scale simulation of the explosion (Röpke et al. 2003, 2004a,b, Schmidt et al. 2004).

The most important hydrodynamic effect in SN Ia explosions is the Rayleigh-Taylor instability. This instability is driven by the buoyancy of bubbles of hot, burned material with respect to the surrounding denser unburned fuel (Müller & Arnett 1982, Niemeyer

& Hillebrandt 1995). The instability makes small perturbations grow and causes the hot bubbles to float upward, while unburned material falls toward the center. At the layers between the differently directed streams, shear instabilities (Kelvin-Helmholtz instability) cause turbulent velocity fluctuations that form a cascade from the scales of the macroscopic flows down to the microscopic scales where they are dissipated (Kolmogorov scale). The turbulence wrinkles and distorts the flame, which increases the surface area of the flame and hence the total energy generation rate.

An important aspect for the spectra and light curve models is that the mushroom-like structures appearing in these 3d-models are able to mix the burning products throughout the envelope such that even iron-group elements can occur far out in low density regions. This has significant impact on the γ-ray deposition rate and opacities within the ejecta. Therefore, synthetic spectra of 3d-explosion models should reveal different properties compared to the 1d models. Studying these effects is a long-term goal of this project.

2.2.3 Radiative transfer

Light curve models

In the present understanding, the light emission of SN Ia is almost entirely powered by the radioactive decay products of ^{56}Ni (Truran et al. 1967, Colgate & McKee 1969). The nuclear burning reactions in the explosion produce ^{56}Ni that is unstable to electron capture and decays to ^{56}Co with a half-life of $t_{1/2} = 6.075\,\mathrm{d}$. ^{56}Co is also unstable with $t_{1/2} = 77.233\,\mathrm{d}$ and decays further to stable ^{56}Fe (Tuli 2000). Via excitation and ionization processes within the ejecta, a large fraction of the emitted γ-energy is converted to optical and infrared photons and emitted in these wave-bands.

A variety of theoretical light curve models have been developed for Type I and Type II Supernovae (e.g., Colgate et al. 1980, Arnett 1980, 1982, Sutherland & Wheeler 1984, Woosley et al. 1986, Höflich et al. 1995, Pinto & Eastman 2000a,b). Important outcomes of the studies in Arnett (1980) and Arnett (1982) were that the maximum bolometric luminosity of the light curve is proportional to the total mass of ^{56}Ni synthesized in the explosion ("Arnett's law"), and that the width of the light curve $\Delta\tau_{\mathrm{LC}}$ is a function of the ejected mass M, the kinetic energy released in the explosion E_{kin}, and the grey mean opacity for optical photons κ_{opt} as follows:

$$\Delta\tau_{\mathrm{LC}} \propto \kappa_{\mathrm{opt}}^{1/2} M^{3/4} E_{\mathrm{kin}}^{-1/4}. \tag{2.1}$$

These relationships have been found to be relatively independent of density profiles and opacity.

More detailed analytic models of light curves of SN Ia have been presented by Pinto & Eastman (2000a). They study the sensitivity of the light curve appearance to the properties of the explosion mechanism. In Pinto & Eastman (2000b) they further discuss the applicability of different mean opacities in light curve calculations. They conclude that to

distinguish subtle effects of different explosion mechanisms, a fully time-dependent solution for the radiative transport is needed. They also argue that the correlation between the peak brightness and the width of the light curve cannot be explained by a single parameter, but is probably caused by a combination of different explosion parameters.

Recently, Sorokina & Blinnikov (2003) derived broad-band UBVI and bolometric light curves for several explosion models using a multi-energy radiation hydrodynamics code that solves the time-dependent angular moment equations for the radiation field in fixed energy bins. While they treat the radiation in non-equilibrium, the state of the gas (occupation numbers for atomic level populations and ionization) is assumed to be in LTE. The line opacities are taken into account following the concept of expansion opacity by Eastman & Pinto (1993).

Synthetic spectra

In the past decades synthetic spectra of SN Ia have been modeled by different groups with a variety of approaches. A complete radiative transfer model for SN Ia would require consistent, time-dependent solutions of the populations of all atomic levels, the continuum, and line transfer, as well as the radioactive decay of ^{56}Ni and ^{56}Co including the treatment of energy deposition by the decay products. Because the solution of time-dependent radiative transfer in three dimensions, including the full coupling of radiation and matter, is not yet feasible, various simplifications have to be implemented depending on the purpose of the model.

Early models by Branch et al. (1985) entirely neglect the continuum transfer and the energy deposition by γ-rays; they use parametrized level populations based on the assumption of resonant line scattering. More recently, based on the same approach, Fisher et al. (1997, 1999) and Fisher (2000) use the highly parametrized LTE spectrum synthesis code SYNOW for line identification in supernova spectra. The advantage of this approach is that, due to the parameterization, the computational effort is very low and thus allows an "online" analysis of observed spectra. This approach, however, is not suitable to gain a deeper understanding of the non-equilibrium physics causing the spectral features observed. This method also requires knowledge of and experience with the physics of spectral formation in supernovae to avoid over-interpretation of the results.

Another approach used by Mazzali et al. (1993), Mazzali & Lucy (1993) (and subsequent publications) solves the radiative transfer by employing a Monte-Carlo procedure and an approximate description of NLTE effects based on a modified version of the LTE-Saha-equation, a technique that was originally introduced by Abbott & Lucy (1985). The solution of the radiative transfer is carried out using the approximation of a negligible continuum transfer, which treats only the part of the ejecta above a given photosphere where line opacities dominate. This approach allows a fairly accurate reproduction of most spectral features and has been successfully used to determine the basic properties of observed spectra. The advantage of this description is that it allows a prompt analysis; the code is very

fast because the approximation of NLTE effects does not require expensive iteration cycles for occupation numbers that are consistent with the radiation field. The method benefits from the circumstance that most of the observed lines in SN Ia are scattering lines which are strong enough to dominate the respective level transition such that continuum transfer effects are negligible for lines. Thus, an approximate description of the NLTE ionization balance already accounts for most of the visible NLTE effects.

Using this method, Stehle et al. (2004) have carried out a detailed study of the radial composition structure of some well-observed SN Ia by modeling a time sequence of spectra. The study uses the property of supernovae that as the line-forming region recedes deeper into the ejecta, the respective element abundances at these radii in velocity space leave imprints on the spectra, while the low-density regions further out do not affect the spectral features significantly.

For all models where continuum transfer is neglected, problems arise in the red and infrared wavelength regions where this assumption is not appropriate anymore. In these wavelength bands, the number of strong lines decreases significantly and the chosen approximation for the "photosphere" imposed at the lower boundary becomes visible in the spectrum. Additionally, to gauge the quality of the approximations made, it is necessary to compare the outcome of these models with those from a more detailed treatment of the involved NLTE effects.

To compute models that do not suffer from major approximations one has to take into account the effects of non-equilibrium physics in detail. The problem then becomes more computationally expensive because the processes in the gas influence the radiation field, which in turn determines the processes themselves. This computation requires iteration cycles to adjust the radiation field and the gas quantities (ionization, level occupation, and temperature structure) consistently. Only more elaborate models, however, provide reliable estimates for the effects of different explosion models and progenitor systems on the emergent spectrum.

For more than a decade, models including most of the relevant non-equilibrium physics in supernova ejecta have been developed and applied to a variety of problems. Eastman & Pinto (1993) use a method to simplify the treatment of the opacities and emissivities from the large number of overlapping lines in supernova ejecta. To derive a mean opacity and emissivity from the contribution of weak lines this method, based on the concept of "expansion opacities" originally introduced by Karp et al. (1977), is employed; stronger lines are explicitly treated in a more detailed way.

Nugent et al. (1997, 1995a) and Lentz et al. (2001) use the radiative transfer code PHOENIX (Hauschildt & Baron 1999, and references therein), which includes the NLTE rate equations for a variety of ions coupled to a solution of the comoving frame radiative transfer and also treats energy deposition by γ-rays. This is achieved, however, at the expense of computational time needed to obtain a consistent model. Therefore, this approach is of limited use for the analysis of a series of spectra within a reasonable time frame.

The WM-basic code employed in the current work, which will be described in more detail later, provides a consistent solution for the full NLTE rate equations; it solves the radiative transfer in the observer's frame in detail. With regard to the method used, the code is computationally more efficient than the comoving frame approach. It was designed to analyze spectra of hot stars with radiatively driven winds and an earlier version of this code has already been used to investigate the effects of line blocking in SN Ia quantitatively by Pauldrach et al. (1996). They used a consistent method to describe the line blocking, however, it did not take the effects on the temperature structure into account. In this work the current improved version of the WM-basic code has been further adapted to treat the radiative transfer in supernovae in a more sophisticated way.

3 Theoretical basis of radiative transfer in supernovae

This chapter gives a brief overview of the physics of radiative transfer in stellar atmospheres as a basis and introduction to the terminology used in the later discussion. A more detailed description can be found in standard textbooks, e.g., Mihalas (1978), Mihalas & Weibel-Mihalas (1984), and Rybicki & Lightman (1979). The theory applied in this work has been developed for expanding stellar atmospheres and is based on the assumptions of *homogeneity, spherical symmetry,* and *stationarity*[1]. Even if the assumption of stationarity in a supernova might sound very restrictive, for spectral models treating only the outermost low-density regions of the expanding envelope, these approximations are generally justified because the interaction time scales of the photons are still much shorter than the expansion time scale. An schematic overview of the physics treated here is given in Figure 3.1.

As seen in the outcome of 3d-hydrodynamic simulations, Type Ia Supernovae appear to be only roughly spherically symmetric objects (Gamezo et al. 2003, Röpke & Hillebrandt 2005). The explosion models of SN II indicate that in such events even global asymmetries may be present (Burrows & Hayes 1996, Scheck et al. 2004, Janka et al. 2004). The justification for adopting spherical symmetry is, however, founded in the fact that no comprehensive method has been developed yet that can describe the full radiative transfer coupled to the equation of state for the gas with a feasible computational effort. Although first steps for more-dimensional radiative transfer models have been taken (see, e.g., Kasen et al. 2003, Kasen 2004, Lucy 2005), such models still contain major simplifications and do not represent a consistent solution of the NLTE radiative transfer.

3.1 LTE vs. non-LTE

In thermodynamic equilibrium (TE), the properties of gas and radiation can be described by macroscopic quantities. In this case, the state of all micro-physical processes is determined uniquely by the relations between these quantities, e.g., temperature T and particle density N. As stars emit radiation they are obviously not in the state of TE; however, in many cases it is still possible to transfer some of these properties by assuming that *locally* the conditions of TE hold. This assumption leads to the concept of *local thermodynamic*

[1] The assumption of homogeneity has been lifted by allowing a depth-dependent composition.

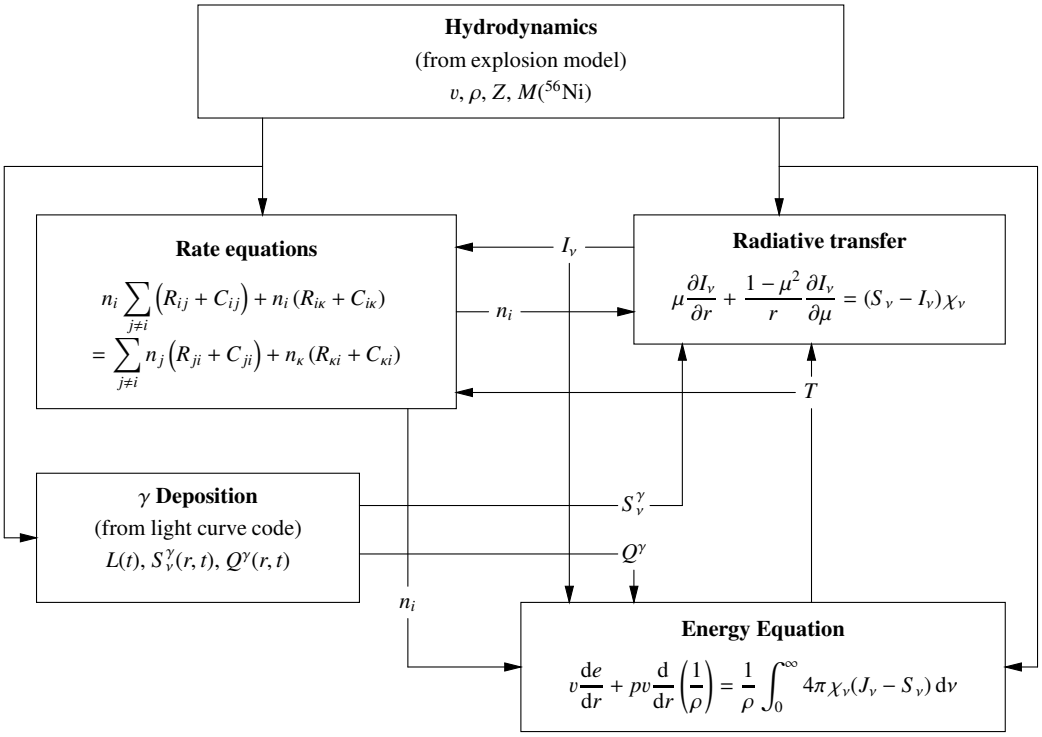

Figure 3.1: Schematic overview of the basic physical equations that have to be treated in the description of radiative transfer in expanding supernova envelopes.

equilibrium (LTE). LTE assumes that the distribution functions for massive particles follow the equilibrium values, while the radiation field is allowed to depart from the equilibrium spectral distribution (i.e., the Planck-function $B_\nu(T)$). The governing equations are the Maxwellian velocity distribution for particles

$$f(v)\, dv = \left(\frac{m}{2\pi\, k_B T}\right)^{3/2} \exp\left(-\frac{mv^2}{2k_B T}\right) 4\pi v^2\, dv \tag{3.1}$$

(with the particle mass m and particle velocity v), and the Saha-ionization equation

$$\frac{N_I}{N_{I+1}} = n_e \frac{U_I}{U_{I+1}} C T^{-3/2} \exp\left(\frac{\chi_I}{k_B T}\right) \tag{3.2}$$

that describes the total number density N_I of the ionization stage I relative to the next higher ionization stage $I+1$. $U = \sum_1^{i_{max}} g_i \exp\left(-E_i/kT\right)$ is the partition function of the respective ionization stage, the ionization potential χ_I, and a constant $C = (h^2/2\pi m k_B)^{3/2}$ ($\approx 2.07 \times 10^{-16}$ in cgs-units). The third important equation is the Boltzmann excitation formula

$$\frac{n_j}{n_i} = \frac{g_j}{g_i} \exp\left(-\frac{E_j - E_i}{k_B T}\right) \tag{3.3}$$

that determines the populations of the atomic levels $n_{i,j}$ within an ionization stage, the statistical weights $g_{i,j}$, and the respective energies above the ground state $E_{i,j}$. These three equations determine the LTE state of the gas from the macroscopic point of view. In the microscopic picture LTE means that all processes are in detailed balance, i.e., each process is exactly balanced by its inverse process.

If the conditions in the gas are such that the condition of detailed balance is not fulfilled, one speaks of *non-local thermodynamic equilibrium* or NLTE. In most cases Eq. (3.1) is still valid because even at very low densities electron collisions maintain the Maxwellian velocity distribution (see Osterbrock 1989); however, the Saha-Boltzmann-equation can no longer be used to describe the level populations correctly. In this case, the equations of statistical equilibrium, as discussed in Section 3.3.1, have to be evaluated for all species in detail.

NLTE occurs whenever the radiation field at a certain place originates from a different region with a different temperature.

The most extreme example of NLTE occurs in gaseous nebulae that are irradiated by hot stars. Here the temperature of the gas is on the order of $\lesssim 10\,000$ K, while the radiation temperature (defined as the temperature that corresponds to the total radiation energy density via $E_0 = 4\sigma_R/cT_{\mathrm{R}}^4$, where $\sigma_R = 2\pi^5 k_{\mathrm{B}}^4/15c^2h^3$ is the Stefan-Boltzmann constant[2]) is on the order of the effective temperature of the central star ($\sim 40\,000$ K). Other examples are the expanding atmospheres of luminous hot stars where the matter density is too low to maintain equilibrium by collisions. Here the radiation temperature is on the order of the gas temperature in those regions where the atmosphere becomes optically thin.

In supernova envelopes NLTE effects are dominant because the fast expanding, low density envelope is illuminated by the non-thermal emission of the down-scattered γ-photons. In early epochs this emission occurs predominantly in deep, optically thick layers, which allows the analogy to a star with a photosphere and a fast expanding envelope. In later epochs, the deposition of γ-energy within the gas directly causes a diffuse radiation field with high T_{R} in certain frequencies.

As discussed later in detail, a consistent NLTE description of supernova envelopes is particularly difficult in intermediate epochs where NLTE effects govern the properties of the gas throughout the ejecta without a real thermalization layer where conditions are close to LTE.

[2] Thus, T_{R} is the temperature that a gas in TE which emits the equivalent amount radiation energy in the given frequency would have. Thus, the radiation temperature is, in general, a frequency-dependent quantity and not necessarily a temperature that occurs anywhere in the gas.

3.2 The radiation transport equation

The transport of radiation through a medium is described by the Boltzmann equation for the phase space distribution function f_R of photons

$$\left(\frac{\partial}{\partial t} + c\boldsymbol{n}\cdot\boldsymbol{\nabla}\right) f_\mathrm{R}(\boldsymbol{r},\boldsymbol{n},\nu,t) = \left(\frac{\partial f_\mathrm{R}}{\partial t}\right)_\mathrm{ic}. \tag{3.4}$$

Here f_R denotes the number of photons per volume $\mathrm{d}V$ at the location $\mathbf{d}\boldsymbol{r}$ at the time t with a frequency $\nu \in [\nu, nu + \mathrm{d}\nu]$ and a velocity c into the solid angle $\mathrm{d}\omega$ in direction $\boldsymbol{n}$. The right-hand-side of Eq. (3.4) is the change of f caused by internal processes within the medium. The specific intensity is then defined as

$$\frac{I(\boldsymbol{r},\boldsymbol{n},\nu,t)}{ch\nu} := f_\mathrm{R}. \tag{3.5}$$

With this definition, Eq.(3.3) turns into

$$\begin{aligned}
\frac{1}{ch\nu}\left[\frac{\partial}{\partial t} + c\boldsymbol{n}\cdot\nabla\right] I(\boldsymbol{r},\boldsymbol{n},\nu,t) &= \frac{1}{h\nu}\left[\frac{\partial}{\partial ct} I(\boldsymbol{r},\boldsymbol{n},\nu,t)\right]_\mathrm{ic} \\
\left[\frac{\partial}{\partial t} + c\boldsymbol{n}\cdot\nabla\right] I(\boldsymbol{r},\boldsymbol{n},\nu,t) &= \left[\frac{\partial}{\partial t} I(\boldsymbol{r},\boldsymbol{n},\nu,t)\right]_\mathrm{ic}
\end{aligned} \tag{3.6}$$

The internal changes to the specific intensity of the radiation field are due to absorption and emission processes on atoms along the light path $\mathbf{d}\boldsymbol{s}$ that add or remove energy from the beam. Emission is given in terms of the macroscopic volume emission coefficient η_ν such that the intensity added to the beam along the path length $\mathrm{d}s$ is given by

$$\delta I^{em} = \eta_\nu \mathrm{d}s.$$

Thus η_ν has the dimensions erg cm^{-2} s Hz^{-1} sr^{-1}. The removal of energy from the beam by absorption processes is determined by the absorption coefficient χ_ν, which is defined such that

$$\delta I_\nu^{abs} = \chi_\nu I_\nu \mathrm{d}s.$$

χ_ν has the dimension cm^{-1}. (Note that this definition ensures that no more photons can be removed than are available.) These coefficients are internal properties of the gas given from microscopic processes and usually also depend on the radiation field itself.

In terms of the quantities η_ν and χ_ν, the transport equation becomes

$$\left[\frac{\partial}{\partial t} + c\boldsymbol{n}\cdot\nabla\right] I(\boldsymbol{r},\boldsymbol{n},\nu,t) = \eta(\boldsymbol{r},\boldsymbol{n},\nu,t) - \chi(\boldsymbol{r},\boldsymbol{n},\nu,t) I(\boldsymbol{r},\boldsymbol{n},\nu,t). \tag{3.7}$$

In the following, only stationary problems without explicit time dependence are discussed so that the time derivative in Eq. (3.7) vanishes.

3.2.1 Coordinate systems

The solution of the transport equation Eq. (3.7) is simplified if the system has symmetries that allow a reduction in the number of dimensions that have to be considered explicitly. Here the plane parallel and the spherically symmetric cases will be discussed. (For a discussion of other symmetries see, e.g., Pomraning (1973).)

The plane-parallel case

The simplest case to be considered is radiation transport through a plane-parallel slab of matter. This approximation is valid if the curvature is negligible, e.g., in cool stars without an extended envelope. In this case, the specific intensity I is a function of the single spatial coordinate x, the angle θ in velocity space between the x-direction and the direction of emission $\boldsymbol{n} = \mathbf{d}\boldsymbol{s}/\mathrm{d}s$ as well as frequency ν and time t. The path element $\mathbf{d}\boldsymbol{s}$ is then given by

$$\mathbf{d}\boldsymbol{s} = \mathrm{d}x\,\boldsymbol{e}_x = \mathrm{d}s\cos\theta\,\boldsymbol{e}_x.$$

Thus, the directional derivative plane-parallel coordinates are given by

$$\boldsymbol{n}\cdot\boldsymbol{\nabla} = \cos\theta\frac{\partial}{\partial x} = \mu\frac{\partial}{\partial x} \tag{3.8}$$

where the commonly used definition $\mu := \cos\theta$ has been introduced. With this result, the time-independent radiative transfer equation for plane-parallel symmetry is

$$\mu\frac{\mathrm{d}I_\nu}{\mathrm{d}x} = \eta_\nu - \chi_\nu I_\nu \tag{3.9}$$

Next we introduce the dimensionless optical path length (optical depth)

$$\begin{aligned} \mathrm{d}\tau_\nu &= -\chi_\nu(\boldsymbol{r})\,\mathrm{d}s \\ \tau_\nu(\boldsymbol{r}_1,\boldsymbol{r}_2) &= -\int_{r_1}^{r_2}\chi_\nu(\boldsymbol{r})\,\mathrm{d}s \end{aligned} \tag{3.10}$$

which in planar symmetry simplifies to

$$\tau_\nu(x,\mu) = -\int_{x_{\max}}^{x}\chi_\nu(x')\,\frac{\mathrm{d}x}{\mu} = \frac{\tau_\nu(x)}{\mu}. \tag{3.11}$$

In the following, $\tau_\nu(r)$ usually refers to the radial optical depth measured from $+\infty$ to r

$$\tau_\nu(r) = -\int_{\infty}^{r}\chi_\nu(r)\,\mathrm{d}r. \tag{3.12}$$

With the definition of the source function that describes the micro-physical processes within the gas

$$S_\nu := \frac{\eta_\nu}{\chi_\nu} \tag{3.13}$$

Eq. (3.9) turns into the commonly used form

$$\mu \frac{\mathrm{d}}{\mathrm{d}\tau_\nu} I_\nu(\tau_\nu, \mu) = S_\nu(\tau_\nu) - I_\nu(\tau_\nu, \mu) \tag{3.14}$$

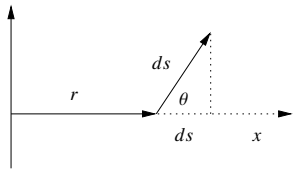

Figure 3.2: Vector **ds** in plane-parallel symmetry

Spherical symmetry

Due to the large spatial extension of supernova envelopes, the plane-parallel description is not a sufficient approximation because curvature effects are important. Thus, throughout this work spherical symmetry of the ejecta is assumed.

In polar coordinates, the specific intensity is a function of time t, frequency ν, the spatial coordinates (r, ϑ, φ), and the angular coordinates in velocity space (θ, ϕ), which describe the direction of emission relative to the radius vector $\boldsymbol{r}$. In spherical symmetry, I_ν depends only on the spatial coordinate r, the azimuthal angle θ in velocity space, frequency ν, and time t. In this case, the path element is given by

$$\mathbf{ds} = \boldsymbol{n}\,\mathrm{d}s = \mathrm{d}r\,\boldsymbol{e}_r + r\mathrm{d}\vartheta\,\boldsymbol{e}_\vartheta \tag{3.15}$$

Because I_ν is independent of the spatial angle ϑ, the spatial coordinate system can be chosen such that $\theta = -\vartheta$ to eliminate one angular coordinate (see Figure 3.3). Then the components of the velocity unity vector $\boldsymbol{n}$ are

$$\begin{aligned} n_r &= \frac{\mathrm{d}r}{\mathrm{d}s} = \cos\theta = \cos\vartheta \\ n_\vartheta &= \frac{r\mathrm{d}\vartheta}{\mathrm{d}s} = \sin\theta = -\sin\vartheta. \end{aligned} \tag{3.16}$$

With Eq. (3.16) the directional derivative in the transfer equation Eq. (3.7) in polar coordinates is

$$\boldsymbol{n} \cdot \boldsymbol{\nabla} = \cos\vartheta \frac{\partial}{\partial r} - \frac{1}{r}\sin\vartheta \frac{\partial}{\partial \vartheta} = \mu \frac{\partial}{\partial r} + \frac{1}{r}(1-\mu^2)\frac{\partial}{\partial \vartheta}. \tag{3.17}$$

Accordingly, the stationary radiative transfer equation in spherical symmetry with an isotropic source function S_ν is

$$\left(\mu \frac{\mathrm{d}}{\mathrm{d}r} + \frac{1-\mu^2}{r}\right) I_\nu(r,\mu) = \chi_\nu \left(S_\nu(r) - I_\nu(r,\mu)\right). \tag{3.18}$$

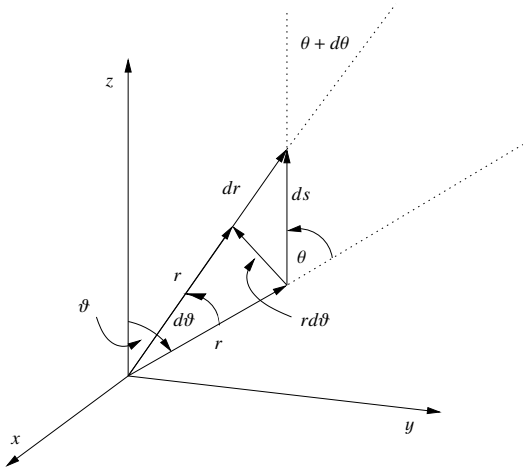

Figure 3.3: Choice of the vectors of radiative transfer in polar coordinates with spherical symmetry

3.2.2 The formal solution

Assuming that the opacities $\chi_\nu(r)$ and source function $S_\nu(r)$ are known, the planar transport equation Eq. (3.14) turns into a first order linear differential equation. For this equation, one can easily derive a *formal solution* for I_ν. For outgoing radiation at an optical depth τ_ν, this is

$$I_\nu(\tau_\nu, \mu) = \int_{\tau_\nu}^{\infty} S_\nu(\tau') e^{-(\tau'-\tau_\nu)/\mu} \frac{\mathrm{d}\tau'}{\mu} \qquad (0 \le \mu \le 1) \tag{3.19}$$

which assumes the *condition of boundedness* $\lim_{\tau\to\infty} I_\nu e^{-\tau_\nu/\mu} = 0$. For the incoming radiation ($-1 \le \mu \le 0$), one correspondingly obtains

$$I_\nu(\tau_\nu, \mu) = \int_{0}^{\tau_\nu} S_\nu(\tau') e^{-(\tau_\nu-\tau')/(-\mu)} \frac{\mathrm{d}\tau'}{(-\mu)} \qquad (-1 \le \mu \le 0) \tag{3.20}$$

which assumes that there is no incident radiation from outside the atmosphere, i.e., $I^- \equiv 0$. In this work both the differential and the integral formulation of the transport equation in spherical symmetry will be employed.

3.2.3 The moments of the transfer equation

For both mathematical and physical descriptions of radiation transport it is useful to define angle averaged quantities of the radiation field I_ν. The most important averages are the mean intensity J_ν (zeroth-order moment), the flux H_ν (first-order moment), and the second-order moment K_ν. For a one-dimensional problem where I_ν is independent of the azimuthal angle ϕ and thus

$$\oint \mathrm{d}\omega = \int_0^{2\pi} \int_{-1}^{1} \cos\vartheta \mathrm{d}\vartheta \, d\phi = 2\pi \int_{-1}^{1} \mathrm{d}\mu$$

one obtains the following definitions for the moments of the radiation field:

$$J(\boldsymbol{r},\nu,t) := (4\pi)^{-1}\oint I(\boldsymbol{r},\boldsymbol{n},\nu,t)\mathrm{d}\omega = \frac{1}{2}\int_{-1}^{1} I(\mu)\,\mathrm{d}\mu \tag{3.21}$$

$$H(\boldsymbol{r},\nu,t) := (4\pi)^{-1}\oint I(\boldsymbol{r},\boldsymbol{n},\nu,t)\,\boldsymbol{n}\mathrm{d}\omega = \frac{1}{2}\int_{-1}^{1} I(\mu)\,\mu\mathrm{d}\mu \tag{3.22}$$

$$K(\boldsymbol{r},\nu,t) := (4\pi)^{-1}\oint I(\boldsymbol{r},\boldsymbol{n},\nu,t)\,\boldsymbol{n}^2\mathrm{d}\omega = \frac{1}{2}\int_{-1}^{1} I(\mu)\,\mu^2\mathrm{d}\mu \tag{3.23}$$

The mean intensity J_ν has the dimensions of erg cm^{-2} s^{-1} Hz^{-1} and is related to the monochromatic energy density of the radiation field E_ν by

$$E_\nu = \frac{4\pi}{c}J_\nu \tag{3.24}$$

The total energy density E in egs cm^{-3} is then obtained from integrating Eq. (3.24) over all frequencies.

The *Eddington flux* H_ν has the dimensions erg cm^{-2} s^{-1} Hz^{-1}. It describes the net flow of radiant energy across an arbitrary surface per unit time. In astrophysics other definitions of the flux are also sometimes used that differ by factors of π or 4π from the definition used here: the flux $\mathcal{F}_\nu \equiv 4\pi H_\nu$ and the "astrophysical flux" $F_\nu = \pi^{-1}\mathcal{F}_\nu$. In the theoretical part of this work, the term "flux" always refers to the Eddington flux H_ν. For comparison to observation, however,

$$F_\lambda = 4\pi\, H_\nu \frac{c}{\lambda^2} \tag{3.25}$$

is plotted because that is the commonly used flux unit in the supernova community.

The second angular moment K_ν in one-dimensional problems is directly related to the radiation pressure

$$p_R(\nu) = \frac{4\pi}{c}K_\nu. \tag{3.26}$$

With these definitions, it is possible to form the angular moments of the radiative transfer equation. The zero-order moment is obtained by integrating the Eq. (3.18) over momentum space $\oint \ldots \mathrm{d}\omega = \int_0^{2\pi}\int_{-1}^{1}\ldots \mathrm{d}\mu\mathrm{d}\phi$. For spherical symmetry, this results in

$$\frac{1}{r^2}\frac{\mathrm{d}\left(r^2 H_\nu(r)\right)}{\mathrm{d}r} = \chi_\nu(r)\left(J_\nu(r) - S_\nu(r)\right). \tag{3.27}$$

It is customary to write the moment equation in spherical symmetry in terms of new variables

$$\tilde{J} := Jr^2 \tag{3.28}$$

$$\tilde{H} := Hr^2 \tag{3.29}$$

$$\tilde{K} := Kr^2. \tag{3.30}$$

Hence, the zeroth moment equation can be written as

$$\frac{\mathrm{d}\tilde{H}_\nu(r)}{\mathrm{d}r} = \chi_\nu(r)\left(\tilde{J}_\nu(r) - \tilde{S}_\nu(r)\right). \tag{3.31}$$

This describes the change in net radiative flux through a surface caused by the local source function S_ν.

In a similar manner, one gets the first-order moment with respect to direction $\boldsymbol{n}$ by multiplying Eq. (3.18) with $\boldsymbol{n}$ and integrating over all solid angles.

$$\begin{aligned} \frac{\mathrm{d}\tilde{K}_\nu(r)}{\mathrm{d}r} + \frac{1}{r}\left(3\tilde{K}_\nu(r) - \tilde{J}_\nu(r)\right) &= -\chi_\nu(r)\tilde{H}_\nu(r) \\ \frac{\mathrm{d}\tilde{K}_\nu(r)}{\mathrm{d}r} + \frac{3f_\nu(r)-1}{r}\tilde{J}_\nu(r) &= -\chi_\nu(r)\tilde{H}_\nu(r) \end{aligned} \tag{3.32}$$

In the second equation, the Eddington factor $f_\nu = K_\nu/J_\nu$ has been used. This factor provides a closure condition to the system by a relation between the zeroth and the first moment.

To rewrite these equations in the same structure as their plane-parallel analogon, a sphericality factor $q = q(\nu, r)$ is introduced:

$$\frac{\mathrm{d}(r^2 q_\nu)}{\mathrm{d}r} := r^2 q_\nu \frac{3f_\nu - 1}{r f_\nu} \qquad \Rightarrow \quad r^2 q_\nu = \exp\left(\int_1^r \frac{3f_\nu(r') - 1}{r' f_\nu(r')}\,\mathrm{d}r'\right). \tag{3.33}$$

Note that in the definition Eq. (3.33), r is relative to the inner radius r_0. This implies that for $r < r_0$, $f_\nu = \frac{1}{3}$ holds. Using Eq. (3.33), the first moment of the the transfer equation can be transformed to:

$$\frac{\mathrm{d}(r^2 q_\nu K_\nu)}{\mathrm{d}r} = -r^2 q_\nu \chi H_\nu \tag{3.34}$$

$$\Rightarrow \quad \frac{d(q_\nu f_\nu \tilde{J}_\nu)}{q_\nu \chi_\nu\,\mathrm{d}r} = -\tilde{H}_\nu \tag{3.35}$$

With the definition of a new optical depth scale $\mathrm{d}\tilde{\tau} = -q\chi\,\mathrm{d}r$, the moment equations are:

$$\frac{\mathrm{d}\tilde{H}_\nu}{\mathrm{d}\tilde{\tau}_\nu} = \frac{1}{q_\nu}\left(\tilde{J}_\nu - \tilde{S}_\nu\right) \tag{3.36}$$

$$\frac{\mathrm{d}(q_\nu f_\nu \tilde{J}_\nu)}{\mathrm{d}\tilde{\tau}_\nu} = \tilde{H}_\nu \tag{3.37}$$

$$\Rightarrow \quad \frac{\mathrm{d}^2(q_\nu f_\nu \tilde{J}_\nu)}{\mathrm{d}\tilde{\tau}_\nu^2} = \frac{1}{q}\left(\tilde{J}_\nu - \tilde{S}_\nu\right). \tag{3.38}$$

3.2.4 Diffusion approximation and Rosseland mean

In an environment of large optical depths $\tau_\nu \gg 1$ where the mean free path lengths of photons $\sim 1/\chi_\nu$ become small, the radiation field is dominated by *local* processes, i.e.,

the gas reaches LTE conditions. In this case, the transport of radiation becomes diffusive (*diffusion limit*) and the source function S_ν approaches the Planck-function

$$S_\nu(\tau) \to B_\nu(T) = \frac{2h\nu^3}{c^2}\frac{1}{e^{h\nu/k_\mathrm{B}T}-1}. \tag{3.39}$$

Therefore, S_ν can be represented as a Taylor expansion in τ_ν

$$S_\nu(\tau'_\nu) = \sum_{n=0}^{\infty}\frac{\partial^{(n)}B_\nu(\tau_\nu)}{\partial\tau_\nu^{(n)}}\frac{(\tau'_\nu-\tau_\nu^n)}{n!}. \tag{3.40}$$

(Note, that an expansion in this form assumes plane-parallel geometry, which is justified if the mean free paths of photons are much smaller than the scales where curvature effects become relevant.) Using this expansion in the formal integral solution Eq. (3.19) for $0 \le \mu \le 1$, one derives

$$I_\nu(\tau_\nu,\mu) = B_\nu(\tau_\nu) + \mu\frac{\partial B_\nu}{\partial\tau_\nu} + \mu^2\frac{\partial^2 B_\nu}{\partial\tau_\nu^2} + \ldots \tag{3.41}$$

For $\tau_\nu \gg 1$, the result for $-1 \le \mu \le 0$ is approximately the same as it differs only by terms $\sim e^{-\tau/|\mu|}$. Thus, Eq. (3.41) can be used for the entire range of the angle μ to obtain the moments

$$J_\nu(\tau_\nu) \approx B_\nu + \frac{1}{3}\frac{\partial^2 B_\nu}{\partial\tau_\nu^2} \tag{3.42}$$

$$H_\nu(\tau_\nu) \approx \frac{1}{3}\frac{\partial B_\nu}{\partial\tau_\nu} + \frac{1}{5}\frac{\partial^3 B_\nu}{\tau_\nu^3} \tag{3.43}$$

$$K_\nu(\tau_\nu) \approx \frac{1}{3}B_\nu + \frac{1}{5}\frac{\partial^2 B_\nu}{\partial\tau_\nu^2}. \tag{3.44}$$

Hence, the approximate solutions of the radiation transport equation in the limit of large optical depth is

$$J_\nu = 3K_\nu = B_\nu \tag{3.45}$$

and

$$H_\nu = -\frac{1}{3}\frac{\partial B_\nu(T)}{\partial\tau_\nu} = -\frac{1}{3}\frac{1}{\chi_\nu}\frac{\partial B_\nu}{\partial T}\frac{\mathrm{d}T}{\mathrm{d}r}. \tag{3.46}$$

In this case, the Eddington factor is just $f_\nu \equiv \frac{1}{3}$. More details on the diffusion limit can be found in Mihalas & Weibel-Mihalas (1984, p.350ff)

Another quantity that is important in this context is the *Rosseland mean opacity* χ_Ross defined by

$$\frac{1}{\chi_\mathrm{Ross}} = \frac{\int_0^\infty \frac{1}{\chi_\nu}\frac{\partial B_\nu}{\partial T}\,\mathrm{d}\nu}{\int_0^\infty \frac{\partial B_\nu}{\partial T}\,\mathrm{d}\nu}. \tag{3.47}$$

From this weighted mean opacity, the so-called grey temperature of a medium (here assumed to be plane-parallel) where the diffusion limit holds can be derived by

$$T_{\text{grey}}^4 = \frac{3}{4} T_{\text{eff}}^4 \left(\tau_{\text{Ross}} + \frac{2}{3} \right) \tag{3.48}$$

where the effective temperature T_{eff} is defined such that the total luminosity is given by $L = 4\pi R^2 \sigma_B T_{\text{eff}}^4$. (Usually the radius R is set as $R = R(\tau_{\text{Ross}} = 2/3)$ and σ_B is the Stefan-Boltzmann constant; see Section 4.2.4 for more details on the determination of the temperature structure.)

3.3 Statistical equilibrium — Rate equations and occupation numbers

Opacities and emissivities of the gas are determined by the occupation numbers of all relevant atomic energy levels of the gas. Since the densities in supernova envelopes can become very low while still significantly affecting the spectrum, collisional processes are not frequent enough to establish LTE conditions. As significant deviations from LTE occur, it is necessary to compute the occupation numbers explicitly considering all relevant interaction of light and matter (cf. Section 3.1).

3.3.1 Statistical equilibrium

The rate of change in the number of particles in a certain state n_i in a volume is given by the net rate of flow of particles in state i into the volume and the net rate of transitions into the state i from all other states j. Assuming a stationary state, the sum of all transitions $n_i P_{ij}$ that de-populate a certain level i must hence be balanced by the sum of all transitions $n_j P_{ji}$ that populate the level i. Thus, the condition of *statistical equilibrium* in a stationary medium is

$$\frac{\partial n_i}{\partial t} = \sum_{j \neq i} n_j P_{ji} - n_i \sum_{j \neq i} P_{ij} - n_i (\boldsymbol{\nabla} \cdot \boldsymbol{v}) = 0. \tag{3.49}$$

Here n_i denotes the number density of atoms of a certain element in state i (i.e., the occupation number of level i) and P_{ij} is the rate coefficient that describes the transition probability per unit time for a transition from state i to state j. For the time being, the advection term $n_i(\boldsymbol{\nabla} \cdot \boldsymbol{v})$ is set to zero in the calculations performed here. This is justified because the time scales of the flow are much larger than typical transition timescales and therefore the advection terms are negligible. Note, however, that this term can become relevant for modeling effects such as the recombination front in Type II Supernovae at maximum light (Eastman & Pinto 1993). With this consideration Eq. (3.49) takes the form

$$n_i \sum_{j \neq i} P_{ij} = \sum_{j \neq i} n_j P_{ji}. \tag{3.50}$$

As long as charge exchange collisions or molecules are not relevant, the solution of this equation system can be carried out element by element. The summations have to include all excitations, de-excitations (i and j within the same ionization stage) as well as ionization and recombination processes (i and j in different ionization stages) of all levels of all relevant ionization stages. Eq. (3.50) leads to a redundant system of equations for each element, which has to be closed by replacing one of the equations by the additional constraint of particle conservation $\sum_i n_i = N$, where $N = \rho Y/A$ is the number density of the respective element. (Here, ρ is the mass density, Y is the abundance as mass fraction, and A is the atomic weight of the element.) The electron number density can be derived by summation over all ionization stages of all elements and the requirement of charge conservation.

Concerning the transition probabilities P_{ij}, one distinguishes between radiative transitions (R_{ij}) that directly involve the radiation field and collisional transitions (C_{ij}) that are associated with collisions between electrons and ions. Depending on the initial and the final state of the electron, one further discriminates between bound-bound, bound-free, and free-free transitions. As mentioned in Section 3.1, in TE each process is exactly balanced by its inverse process (detailed balance).

In the following, the upper level of bound-free processes (ionization and recombination) is denoted with κ. This is, in principle, the ground state of the next higher ionization stage plus an averaged contribution of the free-electron distribution. For ions where the ionization cross-sections to excited states of the next ionization stage are relevant, these ionizations are taken into account.

True and scattering processes

Considering the possible interaction of radiation with matter, an important distinction between two different qualities of interaction processes has to be emphasized (see Mihalas & Weibel-Mihalas 1984, § 72). Processes that transfer energy from the radiation field into the pool of kinetic energy of electrons are called “true” or “thermal” absorption and emission processes. In these processes, radiative energy is taken out of the radiation field and converted into thermal energy in the matter (or vice versa: radiative energy is created at the expense of thermal energy from the electron pool). An example of a true process is photoionization, where a photon transfers its energy to a bound electron and lifts it above the ionization potential of the ion. The electron obtains the kinetic energy corresponding to the photon energy minus the ionization energy. Another example is a photo-excitation process of an ion that is subsequently de-excited by ion-electron collisions transferring the excitation energy to the kinetic energy of the electrons. True processes couple the local (kinetic) gas temperature to the radiation field and determine the spectral properties. In particular regarding the energy deposition by γ-rays, it is important to note that only true processes are capable of transferring high energetic photons into low energy wavelengths.

In contrast to true processes, in pure scattering processes photons are essentially absorbed

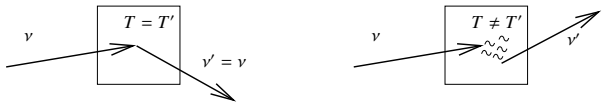

Figure 3.4: Illustration of the difference between *scattering* (left panel) and *true* processes (right panel).

and immediately re-emitted by the same transition (generally into a different direction) *without* significantly changing the photon energy[3]. Here no connection between the radiation field and the local temperature is established and the spectral characteristics of the re-emitted radiation are not changed. An important example of a pure scattering process is electron scattering (Thomson or Compton scattering) that is frequency-independent and isotropizes the incoming radiation without affecting its spectral properties. With regard to Type I Supernovae, it is important to note that in an atmosphere of pure Thomson-scattering that is irradiated from some central source of radiation, the gas temperature would be entirely irrelevant to the spectrum. The emission intensity for scattering processes depends on the intensity of the incoming radiation and almost not on the thermal conditions of the gas. Due to the fact that the radiation field re-emitted at one point generally originates from a different point, scattering processes have a fundamentally *non-local*, and therefore NLTE, character.

In reality the processes are not either exclusively true or scattering processes, but rather a mixture of both because collisional and radiative processes operate simultaneously. Thus, a *realistic model of expanding atmospheres has to treat both channels consistently.* To obtain a realistic picture, it is therefore necessary to derive a *consistent* solution of the radiative transfer *and* the rate equations for statistical equilibrium.

Radiative bound-free transitions

The rate coefficients for photoionization processes $R_{i\kappa}$ are given by

$$R_{i\kappa} = \int_{\nu_{i\kappa}}^{\infty} \frac{4\pi\,\alpha_{i\kappa}(\nu)}{h\nu} J_\nu \,\mathrm{d}\nu \tag{3.51}$$

where $\nu_{i\kappa}$ denotes the threshold frequency. In the code used here, the parameterization of photoionization cross-sections $\alpha_{i\kappa}$ in Seaton's approximation is employed:

$$\alpha_{i\kappa}(\nu) = \alpha_{i\kappa}\left(\beta_{i\kappa}\left(\frac{\nu}{\nu_{i\kappa}}\right)^{s_{i\kappa}} + (1-\beta_{i\kappa})\left(\frac{\nu}{\nu_{i\kappa}}\right)^{s_{i\kappa}-1}\right) \tag{3.52}$$

[3] In the general case, the re-emission is characterized by a redistribution function that describes the probability of the absorption of a photon of energy ν, the direction $\mathbf{n}$, and the emission of a photon of frequency ν' into the direction $\mathbf{n}'$. In this work, we generally assume *complete redistribution* for lines, meaning that the emission is isotropic and the energy is randomly distributed over a line profile. See Mihalas (1978, Ch. 2 and 13) for a more detailed discussion of scattering.

The parameters $\alpha_{i\kappa}$, $\beta_{i\kappa}$, and $s_{i\kappa}$ are fitted to reproduce the cross-sections from detailed calculation. Resonances in the cross-sections due to auto-ionizations and di-electronic recombinations are treated separately as line transitions to the ionized state κ (see Mihalas & Hummer 1973, Pauldrach et al. 1990). The inverse rate, the recombination rate, has a contribution from spontaneous and induced recombination processes:

$$R_{\kappa i} = \left(\frac{n_i}{n_\kappa}\right)^* \int_{\nu_{i\kappa}}^{\infty} \frac{4\pi\,\alpha_{i\kappa}(\nu)}{h\nu} \left(\frac{2h\nu^3}{c^2} + J_\nu\right) e^{-\frac{h\nu}{kT}}\,\mathrm{d}\nu \tag{3.53}$$

where

$$\left(\frac{n_i}{n_\kappa}\right)^* = n_e \frac{g_i}{g_\kappa} e^{h\nu_{i\kappa}/k_B T} \frac{1}{2} \left(\frac{h^2}{2\pi m_e k_B T}\right)^{3/2} \tag{3.54}$$

is the ratio of occupation numbers in LTE given by the Saha-Boltzmann factor with the statistical weights g_i and g_κ of the respective states.

Radiative bound-bound transitions

The transition coefficients of radiative bound-bound (line) transitions between the lower level i and an upper level j are given by the relations

$$R_{ij} = B_{ij} \int_0^\infty \phi_{ij}(\nu) J_\nu\,\mathrm{d}\nu \tag{3.55}$$

$$R_{ji} = A_{ji} + B_{ji} \int_0^\infty \phi_{ij}(\nu) J_\nu\,\mathrm{d}\nu. \tag{3.56}$$

The quantities A_{ji}, B_{ji}, and B_{ij} are the Einstein coefficients of the transition and $\phi_{ij}(\nu)$ is the line profile function with the normalization $\int_0^\infty \phi_{ij}(\nu)\,\mathrm{d}\nu = 1$. In the code used in this work, the line profiles are described by Gauss profiles with a Doppler width corresponding to the local thermal velocity $v_{\mathrm{th}} = \sqrt{2k_B T/m}$ (where m is the mass of the ion) and a contribution of a micro-turbulence velocity v_{turb}:

$$\phi_{ij}(\nu) = \frac{1}{\sqrt{\pi}\Delta\nu_{\mathrm{D}}} \exp\left(-\frac{(\nu-\nu_{ij})^2}{\Delta\nu_{\mathrm{D}}}\right) \qquad \text{with} \qquad \Delta\nu_{\mathrm{D}} = \frac{\nu_{ij}}{c}\sqrt{v_{\mathrm{th}}^2 + v_{\mathrm{turb}}^2}. \tag{3.57}$$

Since the frequency of the line width is much smaller than the transition frequency, the transition coefficients take a form similar to those of the bound-free transitions:

$$R_{ij} = \int_{\nu_{ij}}^\infty \frac{4\pi\,\alpha_{ij}(\nu)}{h\nu} J_\nu\,\mathrm{d}\nu \tag{3.58}$$

and

$$R_{ji} = \left(\frac{n_i}{n_j}\right)^* \int_{\nu_{ij}}^\infty \frac{4\pi\,\alpha_{ij}(\nu)}{h\nu} \left(\frac{2h\nu^3}{c^2} + J_\nu\right) e^{-\frac{h\nu}{k_B T}}\,\mathrm{d}\nu \tag{3.59}$$

with the Boltzmann factor

$$\left(\frac{n_i}{n_j}\right)^* = \frac{g_i}{g_j} e^{h\nu_{ij}/k_B T} \tag{3.60}$$

that determines the LTE occupation number ratio. The cross-sections $\alpha_{ij}(\nu) = \alpha_{ij}\phi_{ij}(\nu)$ and the Einstein coefficients for these transitions are related via

$$\alpha_{ij} = \frac{\pi e^2}{m_e c} f_{ij}, \quad \alpha_{ij} = \frac{h\nu_{ij}}{4\pi} B_{ij}, \quad g_i B_{ij} = g_j B_{ji}, \quad A_{ji} = \frac{2h\nu_{ij}^3}{c^2} B_{ji} \tag{3.61}$$

with the oscillator strength f_{ij}. Usually the transition is characterized by the *gf-value* $gf = g_i f_{ij} = g_j f_{ji}$.

Difficulties computing the bound-bound rate coefficients numerically arise due to the velocity shift of the macroscopic velocity field (Puls & Hummer 1988). A straightforward integration would require a frequency grid fine enough to resolve all line profiles in detail (on the order of 10^7 frequency points). To limit the computing resources we use the Sobolev approximation (Sobolev 1957, Castor 1970) that has been generalized to take into account continuum interactions by Hummer & Rybicki (1985) and Puls & Hummer (1988). Sellmaier et al. (1993) and Santolaya-Rey et al. (1997) have shown that this formalism is an excellent approximation to the much more computationally expensive comoving frame calculations. Deviations are present only for weak lines in sub-sonic regions that, even in stellar atmospheres, do not affect the ionization structure (Santolaya-Rey et al. 1997) and are entirely irrelevant in supernovae where the velocities are much larger (see also Eastman & Pinto 1993).

The integrals in Eq. (3.58) and Eq. (3.59) can be written as

$$\bar{J} = \int_0^\infty \phi_{ij}(\nu) J_\nu \, \mathrm{d}\nu = \tfrac{1}{2} \int_{-1}^{1} \int_0^\infty \phi_{ij}(\nu) I_\nu(\mu) \, \mathrm{d}\nu \mathrm{d}\mu = \tfrac{1}{2} \int_{-1}^{1} \bar{I}(\mu) \, \mathrm{d}\mu \tag{3.62}$$

where $\bar{I}(\mu)$ is the frequency-integrated intensity in the line weighted by the line-profile. In the Sobolev-with-continuum theory (Puls & Hummer 1988), this is expressed as

$$\bar{I} = I_{\mathrm{inc}}(r, \nu(\mu), \mu) \frac{1 - e^{-\tau_S(r,\mu)}}{\tau_S(r,\mu)} + S_{ij} \left(1 - \frac{1 - e^{-\tau_S(r,\mu)}}{\tau_S(r,\mu)}\right) + (S_C - S_{ij}) U(\tau_S(r,\mu), \beta_P). \tag{3.63}$$

In this equation, I_{inc} is the incident intensity in the interaction region of the line, β_P is the escape probability (i.e., the ratio of continuum opacity to line opacity), S_{ij} is the line source function

$$S_{ij} = \frac{n_j A_{ji}}{n_i B_{ij} - n_j B_{ji}} \tag{3.64}$$

and τ_S is the Sobolev optical depth of the interaction zone of the line

$$\begin{aligned} \tau_S(r,\mu) &= \frac{\pi e^2}{m_e c} gf \frac{\left(\frac{n_i}{g_i} - \frac{n_j}{g_j}\right)}{\nu_{ij}/c} \frac{1}{\mu^2 \frac{\mathrm{d}v}{\mathrm{d}r} + (1+\mu^2)\frac{v}{r}} \\ &\equiv \frac{\chi_{ij}}{\nu_{ij}/c} \frac{1}{\mu^2 \frac{\mathrm{d}v}{\mathrm{d}r} + (1+\mu^2)\frac{v}{r}}. \end{aligned} \tag{3.65}$$

The function U resembles a correction term for the inclusion of continuum processes. It describes the probability that a photon is destroyed by absorption into the continuum before it can escape the resonance zone:

$$U(\tau,\beta) = \tau \int_{-\infty}^{\infty} \mathrm{d}x\, \varphi(x) \int_{x}^{\infty} \mathrm{d}y\, \varphi(y) e^{-\tau \int_x^y \mathrm{d}s\, \varphi(s)} \left(1 - e^{-\beta\tau(y-x)}\right), \quad \varphi(x) = \Delta\nu_\mathrm{D}\phi(\Delta\nu_\mathrm{D}x). \tag{3.66}$$

Using this, the rate coefficients can be written as

$$R_{ij} = B_{ij}\bar{J} \qquad \text{and} \qquad R_{ji} = A_{ji} + B_{ji}\bar{J} \tag{3.67}$$

where $\bar{J} = \frac{1}{2}\int_{-1}^{1} \bar{I}\,\mathrm{d}\mu$ of Eq. (3.62) is the intensity in Eq. (3.63) integrated over all solid angles.

The angular integrals

$$P_S = \tfrac{1}{2}\int_{-1}^{1} \frac{1 - e^{-\tau_\mathrm{S}(r,\mu)}}{\tau_\mathrm{S}(r,\mu)}\,\mathrm{d}\mu \tag{3.68}$$

$$\bar{U} = \tfrac{1}{2}\int_{-1}^{1} U(\tau_\mathrm{S}(r,\mu),\beta_P)\,\mathrm{d}\mu \tag{3.69}$$

can be calculated in advance for a grid of values for τ_S and β_P, and interpolated at runtime from tables. I_inc is parameterized as a piecewise linear function of angle μ similar to the procedure in Taresch et al. (1997). Given this parameterization, the integral

$$P_\mathrm{I} = \tfrac{1}{2}\int_{-1}^{1} I_\mathrm{inc}(r,\nu(\mu),\mu)\frac{1 - e^{-\tau_\mathrm{S}(r,\mu)}}{\tau_\mathrm{S}(r,\mu)}\,\mathrm{d}\mu \tag{3.70}$$

can also be pre-computed as a function of the coefficients of the parameterization (see Taresch et al. 1997). I_inc is represented as a piecewise linear function in μ in the two intervals $-1 \le \mu < \mu_c$ and $\mu_c \le \mu < 1$, where $\mu_c = \sqrt{1-(R/r)^2}$ is the angular extent of the core as seen from the current position r. The parameterization is chosen in such a way that the moments J, H, K, and N are retained.

Finally, using Eq. (3.64), the rate coefficients can be expressed as

$$R_{ij} = B_{ij}\left(P_\mathrm{I} + S_\mathrm{C}\bar{U}\right) \tag{3.71}$$

$$R_{ji} = B_{ji}\left(P_\mathrm{I} + S_\mathrm{C}\bar{U}\right) + A_{ji}\left(P_\mathrm{S} + \bar{U}\right) \tag{3.72}$$

which gives the same net rates as Eq. (3.67).

Collisional bound-bound transitions

The rate coefficients for excitations by electron collisions within a single ionization stage are given by

$$C_{ij} = n_e \int_0^\infty v\sigma_{ij}(v) f(v)\,\mathrm{d}v \tag{3.73}$$

where $f(v)$ is the electron velocity distribution function and $\sigma_{ij}(v)$ denotes the collisional excitation cross-section between level i and level j

$$\sigma_{ij}(v) = \frac{\pi\hbar^2}{v^2 m_e^2}\frac{\Omega_{ij}(E)}{g_i} \tag{3.74}$$

with the energy-dependent collision-strength parameter $\Omega_{ij}(E)$. In all cases under consideration, the velocity distribution $f(v)$ of the electron remains Maxwellian; thus, Ω_{ij} is a function of temperature. Then the integral in Eq. (3.73) can be evaluated as a function of temperature:

$$C_{ij} = n_e\left(\frac{2\pi}{k_\mathrm{B}T}\right)^{1/2}\frac{\hbar^2}{m_e^{3/2}}\frac{\Omega_{ij}(T)}{g_{ij}}e^{-h\nu_{ij}/k_\mathrm{B}T} = n_e\frac{8.629\times10^{-6}}{T^{1/2}}\frac{\Omega_{ij}(T)}{g_i}e^{-h\nu_{ij}/k_\mathrm{B}T} \tag{3.75}$$

The code used here employs tabulated values for Ω_{ij} at a temperature $T = 20\,000\,\mathrm{K}$ and a parameter giving the assumed linear dependence of $\Omega_{ij}(T)$ on the temperature. For those radiatively permitted transitions where no data are available, the van Regemorter approximate formula, as given in Mihalas (1978, p.133), is used to determine the collision strength from the oscillator strength f_{ij}

$$C_{ij} = 5.465\times10^{-11}n_e T^{1/2}(14.5\,f_{ij})\bar{g}\left(\frac{E_\mathrm{H}}{h\nu_{ij}}\right)^2\frac{h\nu_{ij}}{k_\mathrm{B}T}e^{-h\nu_{ij}/k_\mathrm{B}T}. \tag{3.76}$$

In this formula, E_H is the ionization energy of hydrogen, and $\bar{g}$ has values of 0.7 if the main quantum numbers of the connected levels are equal and 0.2 if not. For all other transitions, Eq. (3.75) is used with $\Omega_{ij}(T) = 1$ (Pauldrach 1987).

The collisional de-excitation coefficient is linked to the excitation by the LTE-occupation number ratio of the levels involved:

$$C_{ji} = \left(\frac{n_i}{n_j}\right)^* C_{ij}. \tag{3.77}$$

Collisional bound-free transitions

Ionizations and recombinations induced by electron-ion collisions are described by the Seaton approximation following Mihalas (1978):

$$C_{i\kappa} = n_e\frac{1.55\times10^{13}}{T^{1/2}}\frac{\bar{g}\alpha_{i\kappa}}{h\nu_{i\kappa}/k_\mathrm{B}T}e^{-h\nu_{i\kappa}/k_\mathrm{B}T} \tag{3.78}$$

where $\alpha_{i\kappa}$ is the photoionization cross-section at the threshold (cf. Eq. (3.52)) and $\bar{g}$ is equal to 0.1, 0.2, or 0.3 for initial ionic charges of 0, 1, or ≥ 2, respectively. The corresponding recombination coefficient is given by

$$C_{\kappa i} = \left(\frac{n_i}{n_\kappa}\right)^* C_{i\kappa}. \tag{3.79}$$

3.3.2 Opacity and emissivity

Micro-physical transition processes that contain the radiation field are closely related to the opacities and emissivities of the gas because radiative excitation and ionization processes decrease the energy in the radiation field while the corresponding de-excitations and recombinations increase the energy content of the radiation field.

Corresponding to the rate coefficients for the bound-free transitions in Eq. (3.51) and Eq. (3.53), the bound-free emissivity and opacity are given by

$$\begin{aligned}
\eta_{i\kappa}(\nu) &= n_\kappa \alpha_{i\kappa}(\nu) \left(\frac{n_i}{n_\kappa}\right)^* \frac{2h\nu^3}{c^2} e^{-h\nu/k_\mathrm{B}T} \\
\chi_{i\kappa}(\nu) &= n_i \alpha_{i\kappa}(\nu) - n_\kappa \alpha_{i\kappa}(\nu) \left(\frac{n_i}{n_\kappa}\right)^* e^{-h\nu/k_\mathrm{B}T} = n_i \alpha_{i\kappa}(\nu) \left(1 - \frac{n_\kappa}{n_i} \left(\frac{n_i}{n_\kappa}\right)^* e^{-h\nu/k_\mathrm{B}T}\right) \\
&= \frac{\eta_{i\kappa}(\nu)}{S_{i\kappa}(\nu)}
\end{aligned} \tag{3.80}$$

where $S_{i\kappa}$ is the *source function* for bound-free processes

$$S_{i\kappa}(\nu) = \frac{2h\nu^3}{c^2} \frac{1}{\frac{b_i}{b_\kappa} e^{-\frac{h\nu}{k_\mathrm{B}T}} - 1} \tag{3.81}$$

containing the *departure coefficients* $b_i = \frac{n_i}{n_i^*}$ and $b_\kappa = \frac{n_\kappa}{n_\kappa^*}$.

Similarly, the bound-bound emissivity and opacity can be determined from Eq. (3.59) and Eq. (3.58):

$$\begin{aligned}
\eta_{ji}(\nu) &= \eta_{ij}\phi_{ij}(\nu) = n_j \frac{g_i}{g_j} \alpha_{ij} \frac{2h\nu_{ij}^3}{c^2} \phi_{ij}(\nu) = \frac{h\nu_{ij}}{4\pi} n_j A_{ji} \phi_{ij}(\nu) \\
\chi_{ji}(\nu) &= \chi_{ij}\phi_{ij}(\nu) = n_i \alpha_{ij}(\nu) \phi_{ij}(\nu) \left(1 - \frac{n_j}{n_i} \frac{g_i}{g_j}\right) = \frac{h\nu_{ij}}{4\pi} \left(n_i B_{ij} - n_j B_{ji}\right) \phi_{ij}(\nu).
\end{aligned} \tag{3.82}$$

An additional source of opacity and emissivity comes from free-free transitions (Bremsstrahlung). These processes are not considered in the rate equations because all usual unbound states of electrons are considered as a single (temperature-dependent) quasi-level. This is justified because the velocity distribution remains Maxwellian. It is, however, necessary to include the free-free-transitions into the energy balance for the gas (see Section 3.4.1). The free-free opacity and emissivity depend on the number density of particular ions $n_+ = \sum_i n_i$ (summation over all levels of the ionization stage) and the electron density n_e by

$$\begin{aligned}
\chi_\mathrm{ff}(\nu) &= n_e n_+ \alpha_\mathrm{ff}(\nu, T) \left(1 - e^{-h\nu/k_\mathrm{B}T}\right) \\
\eta_\mathrm{ff}(\nu) &= n_e n_+ \alpha_\mathrm{ff}(\nu, T) \frac{2h\nu^3}{c^2} e^{-h\nu/k_\mathrm{B}T}.
\end{aligned} \tag{3.83}$$

Since the electron gas is in thermal equilibrium, the source function of free-free processes must be the Planck-function

$$S_{\mathrm{ff}} = \frac{\eta_{\mathrm{ff}}}{\chi_{\mathrm{ff}}} = B_\nu(T). \tag{3.84}$$

The coefficient α_{ff} depends on a gaunt-factor g_{ff}, which is available from tables (see Mihalas 1978) and can then be written as

$$\alpha_{\mathrm{ff}}(\nu) = \frac{4e^6Z^2}{3ch}\left(\frac{2\pi}{2k_{\mathrm{B}}Tm_e^3}\right)^{1/2}\nu^3 g_{\mathrm{ff}}. \tag{3.85}$$

Here Z denotes the ionic charge, e is the electron charge and m_e is the electron mass. (Strictly speaking, α_{ff} alone is not a cross-section, but $n_+\alpha_{\mathrm{ff}}$ and $n_e\alpha_{\mathrm{ff}}$ are. For consistency with the corresponding quantities in bound-free and bound-bound transitions, it is denoted with α here.)

Another continuous opacity is the Thomson opacity, which is independent of frequency and temperature and origins from photon-electron scattering:

$$\chi_{\mathrm{Th}} = n_e\sigma_{\mathrm{Th}} \tag{3.86}$$

with the Thomson scattering cross-section

$$\sigma_{\mathrm{Th}} = \frac{8\pi}{3}\frac{e^4}{m_e^2c^4} \approx 6.652\times10^{-25}\,\mathrm{cm}^2. \tag{3.87}$$

Assuming complete redistribution over angles, the corresponding emissivity is given by

$$\eta_{\mathrm{Th}} = \chi_{\mathrm{Th}}J_\nu. \tag{3.88}$$

(This is only valid in the limit of low photon-energies. For the treatment of γ-ray transport, the full expression for Compton-scattering has to be considered. Also, in the presence of large thermal electron velocities, the assumption of coherent reemission for Thomson scattered photons is generally not true because the thermal velocities for electrons are much larger than for ions (Rybicki & Hummer 1994, Santolaya-Rey et al. 1997). This causes effects that can be seen in the line wings of stellar spectra. In supernova models, however, the thermal velocities are much smaller due to the low temperatures. The resulting frequency shift is therefore only on the order of a few Å, which is less than the average wavelength resolution in our sampling method.)

3.4 Energy equation and kinetic gas temperature

A crucially important quantity is the gas temperature as a function of optical depth or radius. The gas temperature T is defined as the temperature corresponding to the Maxwellian velocity distribution of the free electron gas. The energy equation of the gas can be ob-

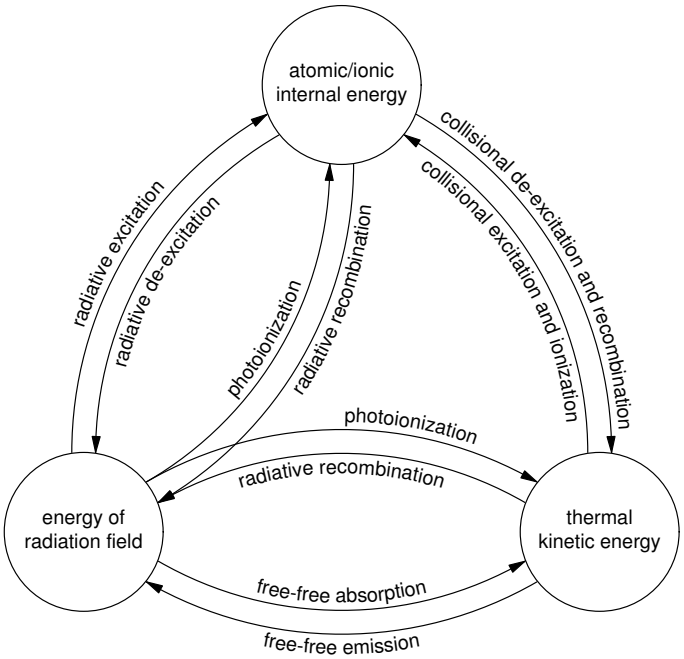

Figure 3.5: Energy transfer by micro-physical processes between the major energy pools in the gas (from Hoffmann 2004).

tained from the second moment of the Boltzmann equation

$$\frac{3}{2}Nk_{\mathrm{B}}v\frac{\partial T}{\partial r} = -Nk_{\mathrm{B}}T\frac{\partial}{\partial r}\left(r^2 v\right) + \oint\int_0^\infty (\chi_\nu - \eta_\nu)I_\nu \,\mathrm{d}\nu \,\mathrm{d}\omega + \frac{1}{r^2}\frac{\partial}{\partial r}\left(r^2 F_{\mathrm{conv}}\right) \tag{3.89}$$

where N is the number density of the gas and v is the local velocity at radius r. The first term on the right-hand side corresponds to adiabatic expansion cooling. The last term accounts for convection, which is $\equiv 0$ for supernova ejecta. The second term contains the energy of the radiation field. This radiative heating and cooling balance dominates the energy equation. The adiabatic expansion cooling may be necessary to include for supernova calculations; however, it is still orders of magnitude smaller than the dominating contributions to the energy balance from the radiation–matter interaction and should not have a significant impact on the overall ionization equilibrium. Thus, it has not been considered for now and we end up with the condition of radiative equilibrium, which expresses the requirement that the total radiative energy absorbed by the matter has to be balanced to the total energy emitted.

$$\oint\int_0^\infty (\chi_\nu - \eta_\nu)I_\nu \,\mathrm{d}\nu \,\mathrm{d}\omega \stackrel{!}{=} 0 \tag{3.90}$$

From the viewpoint of the thermal balance of the matter, this can also be seen as the condition that all energy gains Γ (in $\mathrm{erg\,cm^{-3}\,s^{-1}}$) of the electron gas are balanced by the

total energy loss Λ (cf. Hummer 1963)

$$\sum_k \Gamma_k - \sum_l \Lambda_l \stackrel{!}{=} 0. \tag{3.91}$$

Micro-physically, the absorption or emission of radiative energy will lead to heating or cooling of the gas, respectively, so that in a stationary state, the two approaches are completely equivalent. However, they may differ in their usability for numerical modeling depending on the physical conditions. Both variants will be discussed in further detail in the following. Figure 3.5 summarizes the energy transfers between the dominant energy pools by micro-physical processes.

3.4.1 Thermal equilibrium — Balance of heating and cooling

After the pioneering work of Hummer (1963) and Hummer & Seaton (1963) methods to determine the gas temperature from the heating and cooling processes of the electron gas have been used in to derive the electron gas temperature of gaseous nebulae (see, e.g., Aller 1971, Osterbrock 1989, and references therein).

In a low density environment, absorption and emission are dominated by lines, which mostly have scattering characteristics (i.e., radiative energy absorbed in a transition is emitted in the same transition). Those radiative bound-bound transitions, however, do not directly affect the kinetic energy of the gas. Therefore, in these conditions the radiative properties of the gas are dominated by processes that do not directly depend on the temperature and, thus, the radiative balance is not suitable to constrain the temperature. Here it is numerically advantageous to refer to the energy equation of matter (Pauldrach et al. 1998, Kubát et al. 1999). The energy gain (or heating) and loss (or cooling) rates are closely related to the transition rate coefficients discussed in the previous section.

Heating from photoionizations is given by

$$\Gamma^{\mathrm{R}}_{i\kappa} = \int_{\nu_{i\kappa}}^{\infty} \frac{4\pi\,\alpha_{i\kappa}(\nu)}{h\nu} J_\nu\, h(\nu - \nu_{i\kappa})\,\mathrm{d}\nu \tag{3.92}$$

which corresponds to the photoionization rate with an additional energy term $h(\nu - \nu_{i\kappa})$ in the integral that accounts for the fact that only the energy excess beyond the ionization threshold will be transferred to the free electron as kinetic energy. Analogously, the radiative bound-free cooling rate is given by

$$\Lambda^{\mathrm{R}}_{\kappa i} = \left(\frac{n_i}{n_\kappa}\right)^* \int_{\nu_{i\kappa}}^{\infty} \frac{4\pi\,\alpha_{i\kappa}(\nu)}{h\nu} \left(\frac{2h\nu^3}{c^2} + J_\nu\right) e^{-h\nu/k_{\mathrm{B}}T}\, h(\nu - \nu_{i\kappa})\,\mathrm{d}\nu. \tag{3.93}$$

The coupling between the internal energy of the ions and the thermal pool of the free electron gas is carried via collisional bound-bound transitions, while radiative bound-bound transition (lines) relate only between the radiative energy and the internal ionic energy, but

not the electron temperature. The energy transfered in collisional bound-bound and bound-free transitions corresponds to the change of internal energy of excitation or de-excitation of the ion.

$$\Gamma^{\mathrm{C}}_{i\kappa} = n_\kappa C_{\kappa i} h\nu_{i\kappa} \tag{3.94}$$
$$\Lambda^{\mathrm{C}}_{i\kappa} = n_i C_{i\kappa} h\nu_{i\kappa} \tag{3.95}$$
$$\Gamma^{\mathrm{C}}_{ij} = n_j C_{ji} h\nu_{ij} \tag{3.96}$$
$$\Lambda^{\mathrm{C}}_{ij} = n_i C_{ij} h\nu_{ij} \tag{3.97}$$

In these equations, all C_{xy} correspond to the transition rates in Eq. (3.78), (3.79), (3.76), and (3.77).

Finally, the heating and cooling by free-free-transition of a particular ionic species are given by

$$\Gamma^{\mathrm{ff}} = n_e n_+ \int_0^\infty 4\pi\alpha_{\mathrm{ff}}(\nu, T) J_\nu \,\mathrm{d}\nu \tag{3.98}$$
$$\Lambda^{\mathrm{ff}} = n_e n_+ \int_0^\infty 4\pi\alpha_{\mathrm{ff}}(\nu, T) \left(\frac{2h\nu^3}{c^2} + J_\nu\right) e^{-h\nu/k_{\mathrm{B}}T} \,\mathrm{d}\nu. \tag{3.99}$$

Net rates

For numerical reasons it can be advantageous to write the rates that contain frequency integrals as net rates. The bound-free heating and cooling in Eq. (3.92) and Eq. (3.93) can alternatively be derived from the radiation energy. By interpreting the cooling coefficient as the amount of radiative energy that is transfered from the electron gas into the radiation field one obtains, with the aid of Eq. (3.80),

$$\begin{aligned}\Lambda^{\mathrm{r}}_{i\kappa}(T) &= \oint\!\!\!\int \eta_{i\kappa}(\nu) \frac{h(\nu - \nu_{i\kappa})}{h\nu} \,\mathrm{d}\omega \,\mathrm{d}\nu \\ &= n_\kappa \left(\frac{n_i}{n_\kappa}\right)^* \int_{\nu_{i\kappa}}^\infty 4\pi\,\alpha_{i\kappa} \frac{2h\nu^3}{c^2}\, e^{-h\nu/k_{\mathrm{B}}T} \frac{h(\nu - \nu_{i\kappa})}{h\nu} \,\mathrm{d}\nu.\end{aligned} \tag{3.100}$$

In the same way, the heating coefficients are written as

$$\begin{aligned}\Gamma^{\mathrm{r}}_{i\kappa} &= \oint\!\!\!\int \chi_{i\kappa}(\nu) I_\nu \frac{h(\nu - \nu_{i\kappa})}{h\nu} \,\mathrm{d}\omega \,\mathrm{d}\nu \\ &= \oint\!\!\!\int \frac{\eta_{i\kappa}(\nu)}{S_{i\kappa}} I_\nu \frac{h(\nu - \nu_{i\kappa})}{h\nu} \,\mathrm{d}\omega \,\mathrm{d}\nu \\ &= n_\kappa \left(\frac{n_i}{n_\kappa}\right)^* \int_{\nu_{i\kappa}}^\infty 4\pi\,\alpha_{i\kappa} \frac{2h\nu^3}{c^2}\, e^{-h\nu/k_{\mathrm{B}}T} \frac{J_\nu}{S_{i\kappa}(\nu)} \frac{h(\nu - \nu_{i\kappa})}{h\nu} \,\mathrm{d}\nu\end{aligned} \tag{3.101}$$

with the source function $S_{i\kappa}$ of Eq. (3.81). In this formulation, the net rate can be derived as

$$\begin{aligned}\Gamma^{\mathrm{r}}_{i\kappa} - \Lambda^{\mathrm{r}}_{i\kappa}(T) &= n_\kappa \left(\frac{n_i}{n_\kappa}\right)^* 4\pi \int_{\nu_{i\kappa}}^{\infty} \alpha_{i\kappa} \frac{2h\nu^3}{c^2} e^{-h\nu/k_{\mathrm{B}}T} \left(\frac{J_\nu}{S_{i\kappa}(\nu)} - 1\right) \frac{h(\nu-\nu_{i\kappa})}{h\nu}\,\mathrm{d}\nu \\ &= n_\kappa \left(\frac{n_i}{n_\kappa}\right)^* 4\pi \int_{\nu_{i\kappa}}^{\infty} \alpha_{i\kappa} \frac{2h\nu^3}{c^2} e^{-h\nu/k_{\mathrm{B}}T} \left(\frac{J_\nu/B_\nu}{S_{i\kappa}(\nu)/B_\nu} - 1\right) \frac{h(\nu-\nu_{i\kappa})}{h\nu}\,\mathrm{d}\nu. \end{aligned} \tag{3.102}$$

Here in addition, the radiative quantities J_ν and $S_{i\kappa}(\nu)$ have been expressed as ratios over the Planck function B_ν to obtain a smoother function of frequency, which minimizes the interpolation errors in the numerical integration.

In a similar manner, the free-free net rate can be expressed in terms of the Planck function as $\chi^{\mathrm{ff}} = \eta^{\mathrm{ff}}/B_\nu$:

$$\begin{aligned}\Lambda_{\mathrm{ff}} &= \oint\!\!\!\oint \eta^{\mathrm{ff}}_\nu \,\mathrm{d}\omega\,\mathrm{d}\nu = n_e n_+ \int_0^\infty 4\pi\,\alpha_{\mathrm{ff}} \frac{2h\nu^3}{c^2} e^{-h\nu/k_{\mathrm{B}}T}\,\mathrm{d}\nu \\ \Gamma_{\mathrm{ff}} &= \oint\!\!\!\oint \chi^{\mathrm{ff}}_\nu I_\nu \,\mathrm{d}\nu = \oint\!\!\!\oint \frac{\eta^{\mathrm{ff}}}{B_\nu} I_\nu \,\mathrm{d}\nu \\ &= n_e n_+ \int_0^\infty 4\pi\,\alpha_{\mathrm{ff}} \frac{2h\nu^3}{c^2} e^{-h\nu/k_{\mathrm{B}}T} \frac{J_\nu}{B_\nu}\,\mathrm{d}\nu \end{aligned} \tag{3.103}$$

which leads to the net rate

$$\begin{aligned}\Gamma_{\mathrm{ff}} - \Lambda_{\mathrm{ff}} &= 4\pi\, n_e n_+ \int_0^\infty \alpha_{\mathrm{ff}} \frac{2h\nu^3}{c^2} e^{-h\nu/k_{\mathrm{B}}T} \left(\frac{J_\nu}{B_\nu} - 1\right) \mathrm{d}\nu \\ &= 4\pi\, n_e n_+ \int_0^\infty \frac{4e^6 Z^2}{2hc} \left(\frac{2\pi}{3k_{\mathrm{B}}T m_e^3}\right)^{1/2} \frac{\lambda^3}{c^3} g_{\mathrm{ff}} \frac{2hc^3}{c^2\lambda^3} e^{-h\nu/k_{\mathrm{B}}T} \left(\frac{J_\nu}{B_\nu} - 1\right) \mathrm{d}\nu \\ &= 4\pi\, n_e n_+ \int_0^\infty \frac{4e^6 Z^2}{2hc} \left(\frac{2\pi}{3k_{\mathrm{B}}T m_e^3}\right)^{1/2} \frac{g_{\mathrm{ff}}}{c^3} 2hc\, e^{-h\nu/k_{\mathrm{B}}T} \left(\frac{J_\nu}{B_\nu} - 1\right) \mathrm{d}\nu. \end{aligned} \tag{3.104}$$

3.4.2 Radiative equilibrium — Balance of emission and absorption

The requirement of radiative equilibrium, i.e., the total radiative energy that is absorbed equals the total radiative energy emitted by the gas at all loci r (e.g., Unsöld 1955, Mihalas 1978):

$$\begin{aligned}\oint_{4\pi} \mathrm{d}\omega \int_0^\infty (\chi_\nu I_\nu - \eta_\nu)\,\mathrm{d}\nu \quad &\stackrel{!}{=} 0 \\ \Rightarrow \quad \int_0^\infty \chi_\nu (J_\nu - S_\nu)\,\mathrm{d}\nu \quad &\stackrel{!}{=} 0. \end{aligned} \tag{3.105}$$

The second step assumes that χ_ν and η_ν are isotropic.

Two different forms of this constraint are commonly used: either directly Eq. (3.105) or the first angular momentum of Eq. (3.105), which leads to the condition

$$\nabla H \stackrel{!}{=} 0. \tag{3.106}$$

This flux-conservation constraint has been employed in different approaches to derive the temperature in NLTE models of stellar atmospheres (e.g., Gustafsson 1971, Santolaya-Rey et al. 1997, Pauldrach et al. 1998, 2001). These methods, however, only work in deep layers of an atmosphere at large optical depths because they require that the temperature is predominantly a function of mean optical depth. Therefore, in optically thin regions the integral formulation Eq. (3.105) is used directly.

In a low density environment where the radiation field is mostly decoupled from the temperature, it is more advantageous to use the energy balance of the matter equations because the radiative quantities may be strongly dominated by line transitions that depend only indirectly on the temperature (Kubát et al. 1999, Pauldrach et al. 2001). The application of different temperature correction methods is discussed in Section 4.2.

4 Radiative transfer models — Numerical methods

In this chapter the numerical methods used to model the physical processes discussed in the previous section are explained. An emphasis is put on the aspects that are especially relevant for the SN Ia problem. More details on the numerical implementation can be found in the works that describe the WM-basic code (Pauldrach et al. 1998, 2001, Hoffmann 2004, and references therein).

4.1 General procedure for solving the radiative transfer and rate equations

The general concept behind the code, is to obtain an approximate solution for the correct NLTE occupation numbers with a fast approach (method I) and then derive a detailed, completely consistent solution of the model (method II), which does not contain the limitations of the first method. The approximate solution has to be close enough to the final solution that only a few iterations with the more time-consuming exact method are necessary.

The computation consists of several steps, which are represented in Figure 4.1. The radiative transfer model for supernovae requires the following input:

- Hydrodynamic explosion model — This defines the relationship between radius and density at a given epoch. Generally, a homologous expansion of the ejecta is assumed; therefore, the parameters radius r and epoch t also constrain the velocity field by $v(r) = r/t$. To describe properties of the ejecta, the velocity is used as a radial coordinate because v is independent of the epoch. The relationship between density and radius also sets the optical depth scale, which defines the "photospheric radius." The hydrodynamic quantities r, v, and ρ remain fixed during the calculation of the NLTE model.

- Luminosity — The luminosity corresponds the total amount of radiative energy emitted by the object. In SN Ia the luminosity is given primarily by the energy that is deposited by the γ-rays resulting from the decay of radionuclides synthesized in the explosion. Therefore, part of the luminosity depends radially on the distribution of the respective elements in the ejecta. At the inner boundary of the computational grid an incoming luminosity has to be given to account for the ra-

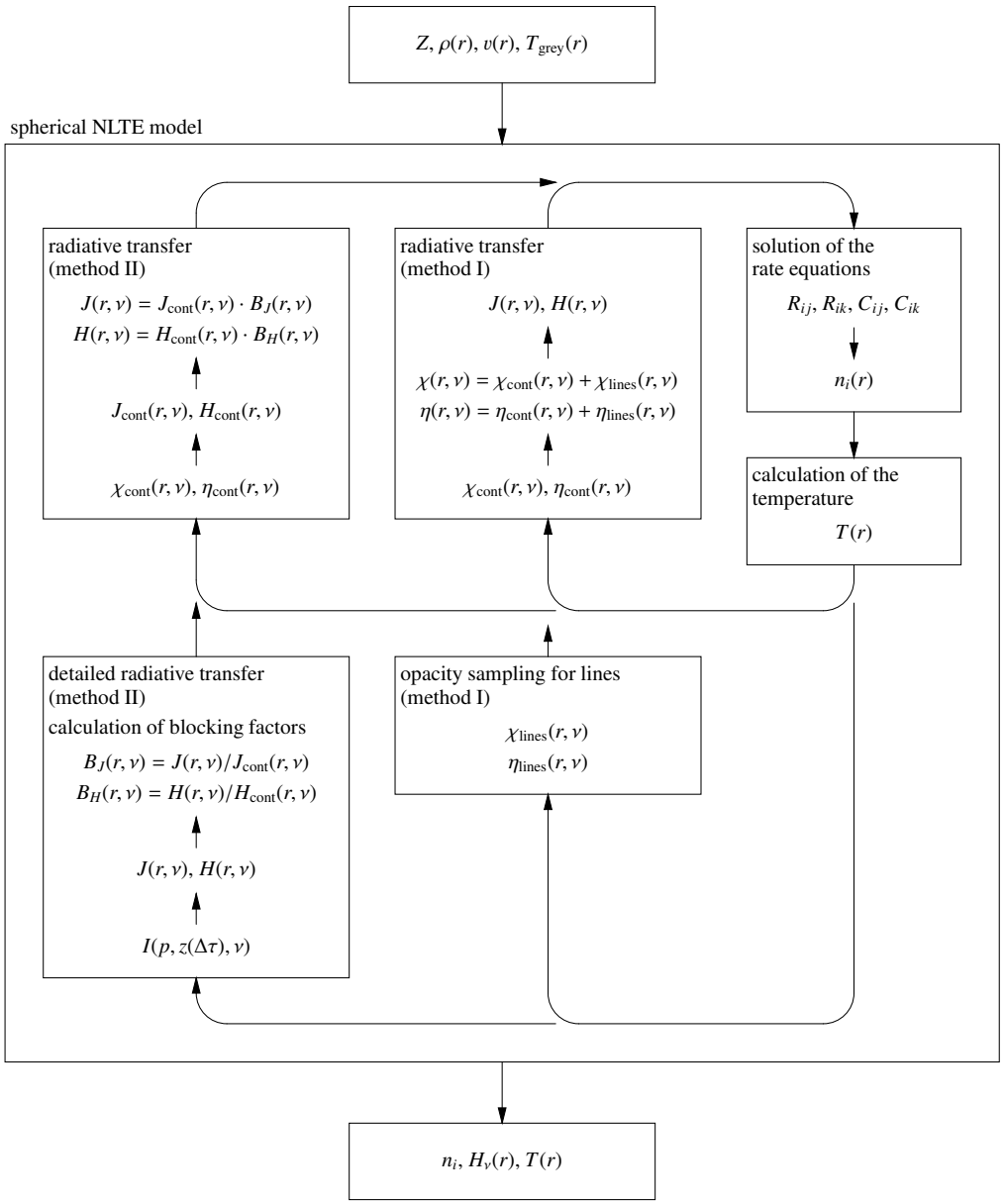

Figure 4.1: Overview of the calculation of the self-consistent NLTE and radiative transfer model. Two methods are used for the calculation of line opacities and the radiative transfer. The fast approximate solution (method I), employing a Doppler-broadened opacity sampling method is followed by a detailed and exact solution (method II) in the last iteration steps. The computationally expensive quantities shown in the lower part of the diagram are not derived in every iteration, but only once in each iteration block, which consists of up to 30 iteration cycles for the other quantities.

diative energy deposited below the boundary. (This also accounts for the photons that have been generated at earlier epochs and trapped by the large opacities.) At the current stage of the project, the energy deposition within the ejecta has not been considered, therefore the total luminosity is assumed to originate from below the boundary of the computational grid (cf. Section 4.4).

- Epoch — For homologously expanding ejecta, the epoch (i.e., the time after the explosion) determines the absolute radius and density. Because the exact time of explosion of an observed supernova is generally not known, the epoch represents an important fit parameter.
- Composition — The element abundances can be taken either from the nucleosynthesis calculations (to study the properties of a specific explosion model) or adjusted independently to fit an observed spectrum in order to determine the abundances of the object. In general, the composition in supernova ejecta is a function of radius.

A first estimate of temperature and electron density is obtained from a spherical grey model. The major part of the calculation consists of the NLTE model (discussed in more detail in the next section). In this step, the radiative transfer is iterated with the rate equations and the temperature to obtain a *consistent* solution of the radiation field, occupation numbers, opacities and emissivities, and temperature structure. Here, all contributions from all relevant ions have to be taken into account. The radiative transfer is calculated including both continuum and lines in the radiation field.

4.1.1 Iteration cycle I — Opacity sampling

The fast, approximate method is based on a *sampling technique* for opacities and emissivities. The idea behind it is to solve the radiative transfer for a *representative* sample of frequency points over the whole wavelength scale of the relevant spectral range[1]. By increasing the number of frequency points, the method converges to the exact solution. The method is described in further detail by Pauldrach et al. (1998) and Pauldrach et al. (2001).

To estimate the number of points needed to achieve a sufficiently accurate representation of the radiation transfer, resolution tests have been performed in addition to the study presented in Pauldrach et al. (2001) because the spectral properties of SN Ia differ significantly from O-stars. To obtain an estimate of the convergence for a set of test models, the integral over J_ν between 2000 Å and 7000 Å was calculated. For all models the spectral window where line blocking was considered was between 350 Å and 18500 Å. This region is significantly larger than in the standard models, which usually do not reach beyond 12000 Å

[1] In this implementation a regularly spaced, logarithmic frequency grid is used, which has the advantage that the vector indices for the adjacent grid points at a certain frequency can be trivially computed. This avoids the need to perform a computationally expensive wavelength search to obtain the value of wavelength-dependent quantities, such as the radiation field for the calculation of rate coefficients.

because the number of spectral lines capable of significantly influencing the radiation field is very low in the infrared region. Therefore, the minimum number of required points obtained from this test can be regarded as a conservative estimate for "normal" supernova calculations. As shown in Figure 4.2 the spread is already well below 5% for less than

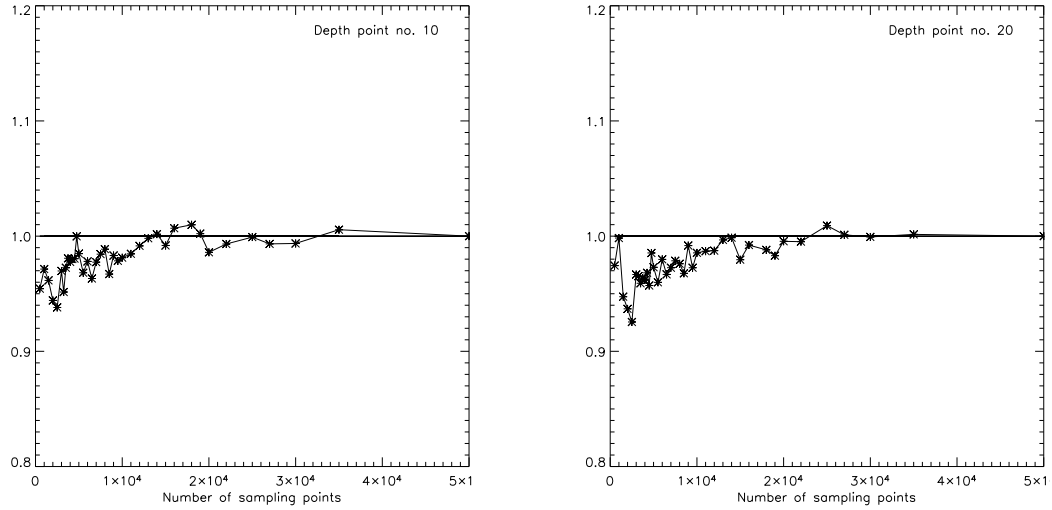

Figure 4.2: Variation of the normalized integrated radiation field between 2000 Å and 7000 Å as a function of the number of sampling points.

5000 points. A value between 4000 and 6000 is used in most calculations.

The most significant approximation in this procedure is that the angular dependence of the Doppler-shifts is neglected. Therefore, the angular variation of opacities and emissivities (in the observer's frame) are not treated correctly (Pauldrach et al. 1998). This, in particular, has the effect that the characteristic P-Cygni profiles are not reproduced because they are a direct consequence of this angular dependence. Based on the result of this approximative solution, the second iteration cycle uses a detailed formal integral solution on a micro-grid, which is able to resolve the individual spectral lines. This method is, however, computationally more costly (in particular in supernovae where, due to the large velocity gradients, significantly more lines can contribute to the opacity at a given frequency than in stellar atmospheres). Therefore, it is necessary that the first method converges the NLTE model close to the final solution. Then only few iterations of the detailed treatment are needed. This concept has been proven to be very reliable for stellar atmospheres (cf. Pauldrach et al. 1998, 2001), however the approximations are more critical in supernova envelopes (see below).

Line shifts

The large macroscopic velocity field in the expanding ejecta has a significant impact on the treatment of line opacities. In the presence of a large velocity field $v(r)$, a line of a

rest-frame frequency ν_0 also affects the radiation at other frequencies $\nu_{ij} = \nu_0(1 + v(r)/c)$. Thus, the Doppler-shift significantly increases the frequency interval that can be affected by a single line. The same effect on the other side limits the spatial area in which a photon of a certain wavelength can be absorbed by a line. (This fact is exploited by the treatment of radiative transfer in the Sobolev Approximation (Sobolev 1957, Castor 1970).) For optically thick lines, however, the overall effect is an increase of blocking compared to a static case.

The total opacity at a frequency ν is composed of the continuum opacity $\chi_c(r, \nu)$ and the line opacity $\chi_l(r, \nu)$

$$\chi(r, \nu) = \chi_c(r, \nu) + \chi_l(r, \nu). \tag{4.1}$$

The line opacity itself is a sum over all contributions of single lines at the radius and frequency under consideration

$$\chi_l(r, \nu) = \sum_{\text{lines}} \chi_{ij}(r)\phi_{ij}(r, \nu). \tag{4.2}$$

The emissivities $\eta(r, \nu)$ are considered analogously. The Doppler-shifts due to the velocity field $v(r)$ are applied to each line opacity before the summation in Eq. (4.2). In method I only the Doppler shift of the central ray is applied instead of taking into account the individual shift for each angular direction μ. Thus, for the line profile, the function

$$\phi_{ij}(r, \nu) = \frac{1}{\Delta\nu_D \sqrt{\pi}} e^{-\frac{\nu - \nu_{ij}(1+v(v)/c)^2}{\Delta\nu_D^2}} \tag{4.3}$$

is used where $\Delta\nu_D = \nu_{ij}/c \sqrt{2k_B T}$ is the Doppler width of the line. This corresponds to a *single-p-ray approximation* (i.e., to one angular impact point) for the sampling opacities and forms the most restrictive approximation of the first iteration cycle.

If one would simply shift the line opacity along the comoving frame frequency from radius point to radius point, as indicated in the upper panel of Figure 4.3, it is apparent that due to the coarse radius grid many frequency grid points would miss a specific line. (Note that the velocity field in Figure 4.3 corresponds to that of a stellar atmosphere. For homologously expanding supernova ejecta, the relationship between radius and comoving frame frequency is linear.) To overcome that problem, in Sellmaier (1996) a method was developed where the intrinsic Doppler profile of the line is convoluted with a boxcar profile $\phi_{\Delta\nu}$ that accounts for the velocity of a radial interval. The boxcar profile represents the mean profile from the velocity shifts $\Delta\nu$ of two adjacent radius points of an interval and closes the gap in the frequency grid. For two frequency points ν_1 and ν_2 corresponding to successive radius points, it can be expressed in terms of the Heaviside step function Θ by

$$\phi_{\Delta\nu} = \frac{\Theta(\nu_2 - \nu) - \Theta(\nu_1 - \nu)}{2(\nu_2 - \nu_1)}. \tag{4.4}$$

The convolution $(\phi_D \circ \phi_{\Delta\nu})(\nu)$ is then

$$\phi(\nu) = (\phi_D \circ \phi_{\Delta\nu})(\nu) = \frac{\operatorname{erf}\left(\frac{\nu_2 - \nu}{\Delta\nu_D}\right) - \operatorname{erf}\left(\frac{\nu_1 - \nu}{\Delta\nu_D}\right)}{2(\nu_2 - \nu_1)}. \tag{4.5}$$

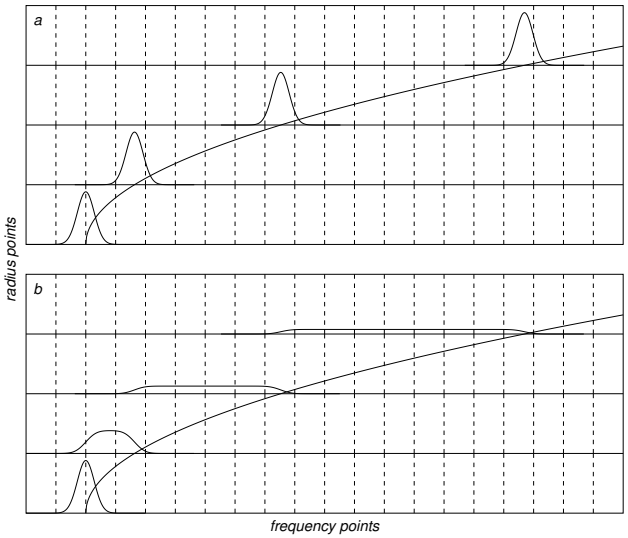

Figure 4.3: The "Doppler-spread opacity sampling" technique (lower panel) ensures that lines that would be missed by a standard opacity sampling method (upper panel) are considered correctly. The method employs a convolution of the line profile with a normalized boxcar function that has a width corresponding to the difference in Doppler-shift between two successive radius grid-points. (Note that the situation indicated here corresponds to the velocity field in a stellar atmosphere. In homologously expanding supernova ejecta radius and frequency shift have a linear relationship.) Figure from Hoffmann (2004).

As shown by Sellmaier (1996) for large velocity gradients, the integration of this opacity over a small radius interval approaches the Sobolev optical depth $\tau_{\mathrm{Sob}}(r)$ of a local resonance zone for the radial ray:

$$\Delta\tau = \int_{r_1}^{r_2} \chi_{ij}\phi(\nu)\,\mathrm{d}r \approx \chi_{ij}\frac{1-(-1)}{2(\nu_2-\nu_1)}(r_2-r_1) = \chi_{ij}\frac{r_2-r_1}{v_2-v_1}\frac{c}{\nu_{ij}} \approx \chi_{ij}\frac{c}{\nu_{ij}}\left(\frac{\mathrm{d}v}{\mathrm{d}r}\right)^{-1} = \tau_{\mathrm{Sob}} \tag{4.6}$$

(see also Pauldrach et al. 2001).

Due to the large velocity gradients in supernovae, essentially all lines are sampled making this method an exact solution (within the limit of the single-p-ray assumption). The statistical character of the sampling technique is almost entirely removed. In nature, the line opacities and emissivities would be strongly peaked inside a radius interval. Therefore, a discretized scheme would be likely to miss significant amounts of lines. The broadening used here effectively projects the line opacity and emissivity of the entire interval onto a radius grid point, such that the correct radiative transfer can be performed for the interval (see lower panel in Figure 4.3).

For the angular variation of line opacity and emissivity no applicable technique similar to the boxcar profile function exists. Therefore, the (radially correctly calculated) opacities $\chi_l(r,\nu)$ on the radial p-ray are considered to be representative for all other angles.

For the calculation of stellar atmospheres, the single-p-ray approximation has been proven to be of sufficient quality to obtain a solution of the radiative transfer that is close enough to the final solution derived with the detailed radiative line transfer calculation (method II, see below). Figure 4.4 shows the difference between the sampling method (thicker line) and the exact solution (thin line) for a stellar model. Note, that the approximation cannot reproduce the absorption and emission parts of P-Cygni profiles correctly because the P-Cygni emission is a consequence of different Doppler-shifts of a spectral line along different angular rays. Apart from that, the agreement of the two methods is good. Therefore, the sampling method provides an excellent basis for the final, computationally more expensive calculations, which then only need few iterations to converge.

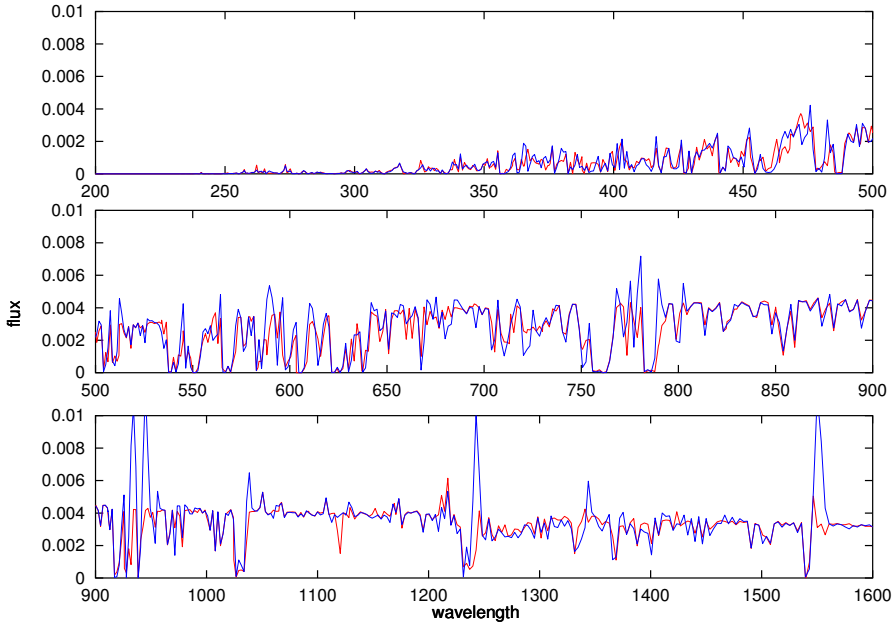

Figure 4.4: Comparison between the Doppler-spread opacity sampling method and the exact solution for a stellar atmosphere model. Shown is the EUV spectrum of the S45 super-giant model (from Pauldrach et al. 2001). The thick (red) line corresponds to the Doppler-spread opacity sampling; the thin (blue) line represents the detailed method. Due to the simplification in the sampling method to regard the line opacities and emissivities only on a single p-ray (corresponding to a single angle), this method cannot correctly reproduce the P-Cygni profiles. Nevertheless, it provides a good basis for the final iteration cycle with the detailed solution (method II) that is not affected by the single p-ray approximation.

In supernova, the single p-ray approximation is more problematic. The velocity gradients are significantly larger and are present within the entire atmosphere, in particular, in the photospheric region. Thus, significant deviations from the correct solutions also occur in the region where the radiation field can have a critical impact on the ionization equilibrium and where the majority of line opacity is formed. This approximation may lead to spuri-

ous results in the photoionization rates and prevent a convergence of the model. A more consistent description, however, is not straightforward if one wants to retain the efficiency of the method. An improvement of this procedure will not be addressed by this work; nevertheless, this issue will be resolved in the near future by our group.

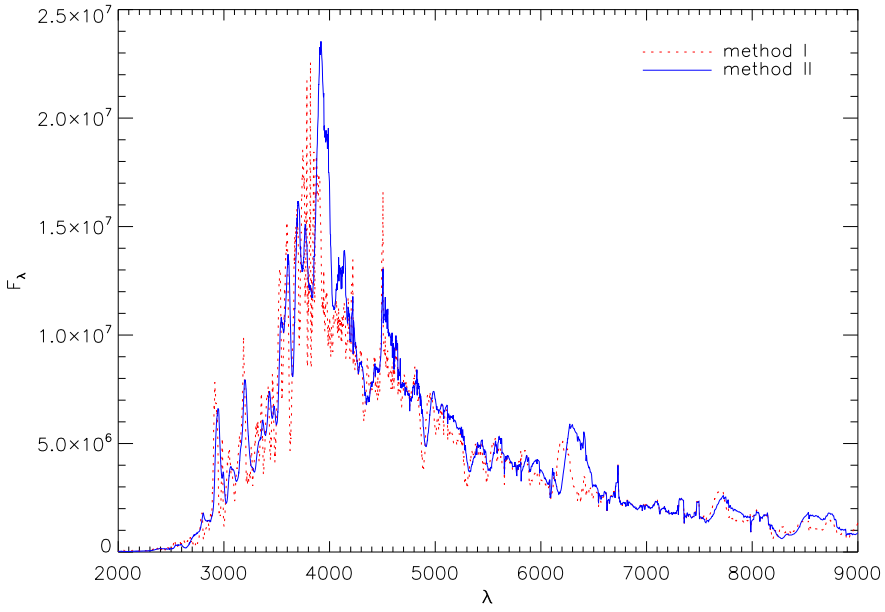

Figure 4.5: As in Figure 4.4, a comparison between the Doppler-spread opacity sampling method and the exact solution, but for a SN Ia test model. Due to the larger velocity gradients the differences in the spectrum are more serious than in the stellar model; however, the overall agreement is still acceptable.

Self-shadowing of lines

One problem arising from the treatment to sum up the opacity and emissivity of all lines in an interval is that the incident intensity needed to calculate the bound-bound transition rates from the Sobolev-with-continuum method, mentioned in Section 3.3.1, is not actually the real intensity incident to the interaction zone, but an averaged intensity over all lines affecting the interval between two radius points. If all lines in the interval have similar strengths, this is not wrong because this average is a representative mean intensity. However, if a single strong line dominates the opacity in an interval, the intensity obtained from the sampling method will be much smaller than the true intensity would be; in the calculation of the intensity, the line itself will already have affected the radiation field in the interval. Consequently, the source function of the line will be underestimated and the line will be systematically too weak compared to the amount of absorbed (or emitted) ra-

diative energy that is accounted for in the rate equation. This inconsistency can effectively lead to an unphysical loss of energy in the model.

The inconsistency is corrected by using a radiation field to determine the bound-bound rates of a dominating lines, which is not directly affected by the line itself. For the correction, a suitable interpolation of the radiation field between the previous and next radius grid points is employed[2] (Pauldrach et al. 1998).

The Feautrier algorithm — Solution of the radiative transfer equations as a two point boundary problem

For the solution of the radiative transfer in observer's frame, three similar algorithms are used. The start solution is obtained from a Rybicki-method (Rybicki 1971, Mihalas 1978, p. 158) that implicitly solves the transport equation including the Thomson scattering. Because this solution does not have a very high accuracy, an iteration for the radiation field that enters into the Thomson emissivity is done. Here, the ray-by-ray solution and the angle integrated moment equations are iterated. Both systems are solved with a Feautrier scheme (cf. Mihalas 1978, p. 156). For each frequency point, the iteration is performed twice: first for a pure continuum model and afterwards for the full problem with continuum and lines. One crucial limitation of this approach is that, strictly speaking, the Feautrier method is only applicable if the opacities and source functions vary only slowly over radius, i.e., the radial variation of the lines would have to be resolved by the grid. The sampling iteration, however, uses a coarse radial grid consisting of 41 depth points. Therefore, most lines will be present at a single grid point only.

To be able to use that algorithm, the standard procedure had to be modified (see also Section 5.3). To numerically solve the transport equation Eq. (3.18), a descretization method that obtains sufficient accuracy has to be used. The solution is carried out in the Cartesian p-z-coordinate system that is illustrated in Figure 4.6. The transformation between the r-μ and p-z-coordinates can be derived to

$$\mu = \frac{z}{r} \qquad \Rightarrow \qquad \mu = \frac{z}{\sqrt{z^2 + p^2}} \tag{4.7}$$

$$r^2 = z^2 + p^2 \qquad \Rightarrow \qquad r = \sqrt{p^2 + z^2} \tag{4.8}$$

and, therefore,

$$\mathrm{d}r = \frac{z}{\sqrt{z^2 + p^2}}\,\mathrm{d}z = \mu\,\mathrm{d}z \tag{4.9}$$

$$\mathrm{d}\mu = \left(\frac{1}{\sqrt{p^2 + z^2}} - \frac{z^2}{\sqrt{p^2 + z^2}}\right)\mathrm{d}z = \frac{1 - \mu^2}{r}\,\mathrm{d}z. \tag{4.10}$$

[2] Actually, instead of manipulating the radiation field entering the Sobolev-with-Continuum formalism, the coefficients of the employed parameterization of I_{inc} are interpolated directly.

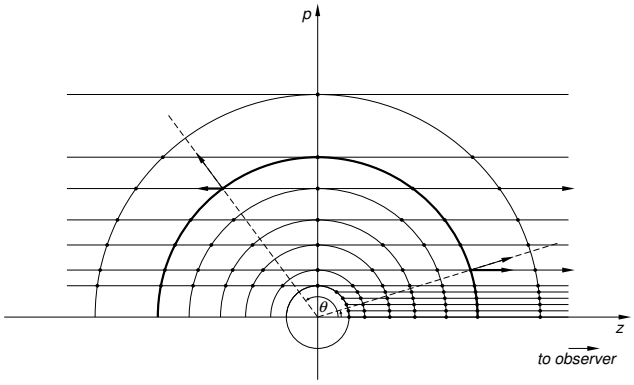

Figure 4.6: Sketch of the *p*-*z* coordinate system that is used for the solution of the radiative transfer. In this geometry, each *p*-ray corresponds to a ray in direction μ in the *r*-μ coordinate system.

In *p*-*z* coordinates, each *p*-ray corresponds to a μ-direction in spherical coordinates. To solve the transport equation in this geometry, it is useful to convert this first order differential equation with one single boundary condition into a second order differential equation with a boundary condition for each side (e.g., Mihalas 1978). For this method, introduced by P. Feautrier, the transfer equation for each *p*-ray is rewritten for the intensities in positive and negative *z*-direction

$$\frac{\mathrm{d}I^{\pm}}{\mathrm{d}\tau} = \pm(S - I^{\pm}) \quad \text{with} \quad \mathrm{d}\tau = -\chi \mathrm{d}z. \tag{4.11}$$

By introducing the new variables

$$\begin{aligned} u &= \tfrac{1}{2}\,(I^{+} + I^{-}) \quad \text{intensity-like} \\ v &= \tfrac{1}{2}\,(I^{+} - I^{-}) \quad \text{flux-like} \end{aligned} \tag{4.12}$$

Eq. (4.11) can be written as a system of two coupled differential equations

$$\frac{\mathrm{d}u}{\mathrm{d}\tau} = v \tag{4.13}$$

$$\frac{\mathrm{d}v}{\mathrm{d}\tau} = u - S. \tag{4.14}$$

After combining these two equations by eliminating v, one obtains the single second order differential equation for u with the independent variable τ:

$$\frac{\mathrm{d}^2u}{\mathrm{d}\tau^2} = u - S. \tag{4.15}$$

In the standard discretized scheme, this equation is represented as a set of difference equations – one for each radial grid point i along the ray:

$$\left.\frac{\mathrm{d}^2u}{\mathrm{d}\tau^2}\right|_{\tau_i} \approx \frac{\left.\frac{\mathrm{d}u}{\mathrm{d}\tau}\right|_{\tau_{i+1/2}} - \left.\frac{\mathrm{d}u}{\mathrm{d}\tau}\right|_{\tau_{i-1/2}}}{\tau_{i+1/2} - \tau_{i-1/2}} \approx \frac{\frac{u_{i+1}-u_i}{\tau_{i+1}-\tau_i} - \frac{u_i-u_{i-1}}{\tau_i-\tau_{i-1}}}{\frac{1}{2}(\tau_{i+1} - \tau_i) - \frac{1}{2}(\tau_i - \tau_{i-1})}. \tag{4.16}$$

This represents a linear equation system for u_i

$$A_i u_{i-1} + B_i u_i + C_i u_{i+1} = S_i \tag{4.17}$$

with the coefficients

$$\begin{aligned} A_i &= -\left(\tfrac{1}{2}\left(\tau_{i+1} - \tau_{i-1}\right)\left(\tau_i - \tau_{i-1}\right)\right)^{-1} \\ C_i &= -\left(\tfrac{1}{2}\left(\tau_{i+1} - \tau_{i-1}\right)\left(\tau_{i+1} - \tau_i\right)\right)^{-1} \\ B_i &= 1 - A_i - C_i. \end{aligned} \tag{4.18}$$

This tridiagonal matrix system can be solved efficiently by standard linear algebra solvers. In the application here, a Rybicki-type scheme (Rybicki 1971, Mihalas 1978, p. 158) is used that solves all p-rays simultaneously to implicitly account for the radiation field J that enters in the scattering part of the source function S.

The equation Eq. (4.16) contains only differences in τ that can be easily derived from the opacities χ_i at the respective grid points of the z grid from

$$\Delta\tau_{i,i-1} = -\tfrac{1}{2}(\chi_i + \chi_{i-1})(z_i - z_{i-1}). \tag{4.19}$$

The system is well behaved if opacities and source functions are slowly varying functions of z. Problems can arise if these conditions cannot be guaranteed, such as when strong ionization edges occur or a large velocity gradient shifts strong lines in frequency. Such situations can cause large variations of the opacity from grid point to grid point at a given frequency. One problematic situation discussed in Pauldrach et al. (2001) is if a point with a large source function S_i and low opacity χ_i is adjacent to a point with high opacity χ_{i+1} and low or average source function S_{i+1}. In reality, the large source function S_i should have only a small impact on the radiation field as it occurs in a low opacity region (therefore the emissivity is also small). In the solution of the equation system, however, the emission computed in this situation is on the order of

$$\Delta I \approx \bar{S}\Delta\tau \approx \tfrac{1}{2}(S_{i+1} + S_i) \cdot \tfrac{1}{2}(\chi_{i+1} + \chi_i)(z_{i+1} - z_i). \tag{4.20}$$

In this expression, the term $S_i\chi_{i+1}$ dominates under the assumed conditions, which leads to an artificially enhanced emission. This happens because physically it does not make sense to multiply the source function of one point with the opacity of another point. Source functions, as a matter of principle, are only meaningful quantities relative to the opacity at the same point. As discussed by Pauldrach et al. (2001), the method can still be used if the equation system is rewritten in z instead of τ because the z-dependence of χ can be treated correctly only in this formulation. Eq. (4.15) becomes then

$$\frac{1}{\chi}\frac{\mathrm{d}}{\mathrm{d}z}\left(\frac{1}{\chi}\frac{\mathrm{d}u}{\mathrm{d}z}\right) = u - S. \tag{4.21}$$

Carrying out the same discretization as before leads to the new difference system

$$\left.\frac{1}{\chi_i}\left(\frac{\mathrm{d}}{\mathrm{d}z}\left(\frac{1}{\chi}\frac{\mathrm{d}u}{\mathrm{d}z}\right)\right)\right|_i \approx \frac{1}{\chi_i}\frac{\left(\frac{1}{\chi}\frac{\mathrm{d}u}{\mathrm{d}z}\right)_{i+1/2} - \left(\frac{1}{\chi}\frac{\mathrm{d}u}{\mathrm{d}z}\right)_{i-1/2}}{z_{i+1/2} - z_{i-1/2}} \tag{4.22}$$

$$\approx \frac{1}{\chi_i}\frac{\frac{1}{\bar{\chi}_{i+1,i}}\frac{u_{i+1}-u_i}{z_{i+1}-z_i} - \frac{1}{\bar{\chi}_{i,i-1}}\frac{u_i-u_{i-1}}{z_i-z_{i-1}}}{\frac{1}{2}(z_{i+1}+z_i) - \frac{1}{2}(z_i+z_{i-1})}. \tag{4.23}$$

Thus, the coefficients Eq. (4.18) are now

$$\begin{aligned} A_i &= -\left(\tfrac{1}{2}\chi_i\,(z_{i+1}-z_{i-1})\,\bar{\chi}_{i,i-1}\,(z_i-z_{i-1})\right)^{-1} \\ C_i &= -\left(\tfrac{1}{2}\chi_i\,(z_{i+1}-z_{i-1})\,\bar{\chi}_{i+1,i}\,(z_{i+1}-z_i)\right)^{-1} \\ B_i &= 1 - A_i - C_i \end{aligned} \tag{4.24}$$

where the the first terms of A and B now contain the *local* opacity. For the mean opacity $\bar{\chi}$, the geometric mean

$$\bar{\chi}_{i+1,i} = \sqrt{\chi_{i+1}\cdot\chi_i} \tag{4.25}$$

generally produces reasonable results for stars. While Eq. (4.25) puts more weight on the lower of the two opacities, using the arithmetic mean

$$\bar{\chi}_{i+1,i} = \tfrac{1}{2}(\chi_i + \chi_{i+1}) \tag{4.26}$$

weights the high opacities stronger. Another caveat about using the Feautrier scheme for solving the radiative transport for conditions where the opacity is not smoothly distributed over radius is that part of the line emissions are incorrectly re-absorbed in the adjacent intervals because the source functions are defined on the grid points only. For a detailed discussion of this issue, see Section 5.3.

Boundary conditions

To close the system in Eq. (4.16) appropriate boundary conditions have to be chosen. The respective boundary equations can be obtained from an expansion of u_i in τ at the boundary points outside ($i = N$) and inside ($i = 1$):

$$u_{N-1} = u_N + (\tau_N - \tau_{N-1})\left.\frac{\mathrm{d}u}{\mathrm{d}\tau}\right|_{\tau_N} + \tfrac{1}{2}(\tau_N - \tau_{N-1})^2\left.\frac{\mathrm{d}^2u}{\mathrm{d}\tau^2}\right|_{\tau_N} \tag{4.27}$$

and

$$u_2 = u_1 + (\tau_2 - \tau_1)\left.\frac{\mathrm{d}u}{\mathrm{d}\tau}\right|_{\tau_1} + \tfrac{1}{2}(\tau_2 - \tau_1)^2\left.\frac{\mathrm{d}^2u}{\mathrm{d}\tau^2}\right|_{\tau_1}. \tag{4.28}$$

It is assumed that there is no incident radiation ($I^- \equiv 0$) at the outer boundary[3]. Thus from Eq. (4.13), one obtains

$$u = v \qquad \Rightarrow \qquad \left.\frac{\mathrm{d}u}{\mathrm{d}\tau}\right|_{\tau=0} = u. \tag{4.29}$$

With Eq. (4.15), this leads to the outer boundary condition

$$u_{N-1} = u_N + (\tau_{N-1} - \tau_N)u_N + \tfrac{1}{2}(\tau_{N-1} - \tau_N)^2(u_N - S_N) \tag{4.30}$$

and the coefficients

$$A_N = -2(\tau_{N-1} - \tau_{N-1})^{-2} \tag{4.31}$$

$$B_N = 1 + 2(\tau_{N-1} - \tau_N)^{-1} + 2(\tau_{N-1} - \tau_N)^{-2} = 1 + 2(\tau_2 - \tau_1)^{-1} - A_N. \tag{4.32}$$

At the inner boundary, rays that intersect the core ($p < R$) must be distinguished from those that do not ($p > R$). For core-rays the incident intensity has to be explicitly specified $I^+ = I_{\mathrm{core}}$, while for non-core rays a reflecting boundary $I^+ = I^-$ is used. Noting that $v = \frac{1}{2}(I^+ - I^- + I^+ - I^+) = I^+ - u$, one gets in Eq. (4.13)

$$\left.\frac{\mathrm{d}u}{\mathrm{d}\tau}\right|_{\tau_{\max}} = I_{\mathrm{core}} - u \qquad (p < R) \tag{4.33}$$

for core-rays and

$$\left.\frac{\mathrm{d}u}{\mathrm{d}\tau}\right|_{\tau_{\max}} = 0 \qquad (p > R) \tag{4.34}$$

for non-core rays. Combining Eq. (4.27), Eq. (4.15) and, Eq. (4.14) one gets

$$u_2 = u_1 + (\tau_1 - \tau_2)(I_{\mathrm{core}} - u_1) + \tfrac{1}{2}(\tau_2 - \tau_1)^2(u_1 - S_2) \quad (p < R) \tag{4.35}$$

$$u_2 = u_1 + \tfrac{1}{2}(\tau_2 - \tau_1)^2(u_1 - S_1) \quad (p > R) \tag{4.36}$$

and the coefficients

$$C_1 = -2(\tau_1 - \tau_2)^{-2} \tag{4.37}$$

$$B_1 = 1 - 2(\tau_1 - \tau_2)^{-1} + 2(\tau_1 - \tau_2)^{-2} \quad (p < R) \tag{4.38}$$

$$B_1 = 1 + 2(\tau_1 - \tau_2)^{-2} \qquad (p > R) \tag{4.39}$$

$$S_1^* = S_1 - 2(\tau_1 - \tau_2)^{-1} I_{\mathrm{core}} \qquad (p < R) \tag{4.40}$$

$$S_1^* = S_1 \qquad (p > R). \tag{4.41}$$

These boundary conditions can be expressed in terms of the z-variable analogous to the non-boundary equations. The choice of the incident intensity I_{core} at the core will be discussed in more detail in Section 5.2.

[3] Actually, at the outer boundary, an extrapolation for the I^- from radii larger than the computational grid is performed. This is not relevant for supernovae because of steep density gradients and low absolute densities in the outer region.

Solution of the moment equations

A similar system can be employed to solve the moment equations Eq. (3.36) to Eq. (3.38)

$$\frac{\mathrm{d}\tilde{H}}{\mathrm{d}\tilde{\tau}} = \frac{1}{q}\left(\tilde{J} - \tilde{S}\right) \qquad \frac{\mathrm{d}(qf\tilde{J})}{\mathrm{d}\tilde{\tau}} = \tilde{H} \tag{4.42}$$

$$\frac{\mathrm{d}^2(qf\tilde{J})}{\mathrm{d}\tilde{\tau}^2} = \frac{1}{q}\left(\tilde{J} - \tilde{S}\right) \tag{4.43}$$

where all symbols have the same meaning as in Section 3.2.3. (Again the index ν has been dropped for brevity.) The last equation, Eq. (3.38), can be written in terms of the radius r

$$\frac{1}{q\chi}\frac{\mathrm{d}}{\mathrm{d}r}\left(\frac{1}{q\chi}\frac{\mathrm{d}(qf\tilde{J})}{\mathrm{d}r}\right) = \frac{1}{q}\left(\tilde{J} - \tilde{S}\right). \tag{4.44}$$

The additional advantage here is that one can implicitly solve for the contribution of Thomson scattering to the source function S. Separating the emissions due to true processes and those due to Thomson-scattering (which is $\chi^{\mathrm{Thoms}} J$), one can write

$$S = \frac{\eta^{\mathrm{true}}}{\chi^{\mathrm{true}} + \chi^{\mathrm{Thoms}}} + \frac{\chi^{\mathrm{Thoms}}}{\chi^{\mathrm{true}} + \chi^{\mathrm{Thoms}}} J = S^{\dagger} + \beta J \tag{4.45}$$

with the definitions

$$S^{\dagger} := \frac{\eta^{\mathrm{true}}}{\chi} \qquad \text{and} \qquad \beta := \frac{\chi^{\mathrm{Thoms}}}{\chi}. \tag{4.46}$$

Using this in Eq. (4.44) gives

$$\frac{1}{\chi}\frac{\mathrm{d}}{\mathrm{d}r}\left(\frac{1}{q\chi}\frac{\mathrm{d}(qf\tilde{J})}{\mathrm{d}r}\right) = \tilde{J}(1-\beta) - \tilde{S}^{\dagger} \tag{4.47}$$

which can be discretized by

$$-\frac{1}{\chi_i(r_{i+1} - r_{i-1})}\left(\frac{f_{i+1}q_{i+1}\tilde{J}_{i+1} - f_i q_i \tilde{J}_i}{\overline{q\chi}_{i+1,i}(r_{i+1} - r_i)} - \frac{f_i q_i \tilde{J}_i - f_{i-1}q_{i-1}\tilde{J}_{i-1}}{\overline{q\chi}_{i,i-1}(r_i - r_{i-1})}\right) + (1-\beta)\tilde{J}_i = S_i^{\dagger}. \tag{4.48}$$

where $\overline{q\chi}_{i+1,i}$ are again appropriate means of the product $q\chi$ at adjacent grid points. However, the system still needs the Eddington factors $f_\nu = K_\nu / J_\nu$ as an external input obtained from the ray-by-ray solution. The coefficients of the equation system

$$\mathcal{A}_i \tilde{J}_{i+1} + \mathcal{B}_i \tilde{J}_i + C_i \tilde{J}_{i-1} = \mathcal{K}_i \tag{4.49}$$

become

$$\mathcal{A}_i = -\frac{f_{i+1}q_{i+1}}{\frac{1}{2}\chi_i(r_{i+1} - r_{i-1})\overline{q\chi}_{i+1,i}(r_{i+1} - r_i)} \tag{4.50}$$

$$C_i = -\frac{f_{i-1}q_{i-1}}{\frac{1}{2}\chi_i(r_{i+1} - r_{i-1})\overline{q\chi}_{i,i-1}(r_i - r_{i-1})} \tag{4.51}$$

$$\mathcal{B}_i = \frac{f_i q_i}{\frac{1}{2}\chi_i(r_{i+1} - r_{i-1})}\left(\frac{1}{\overline{q\chi}_{i+1,i}(r_{i+1} - r_i)} - \frac{1}{\overline{q\chi}_{i,i-1}(r_i - r_{i-1})}\right) + (1-\beta) \tag{4.52}$$

$$\mathcal{K}_i = \tilde{S}^{\dagger}. \tag{4.53}$$

At the boundaries, the system is closed by employing factors similar to the second Eddington factor[4]

$$h := \frac{\int_0^1 u(\mu)\,\mu \mathrm{d}\mu}{\int_0^1 u(\mu)\,\mathrm{d}\mu} \tag{4.54}$$

with $u(\mu)$ from the solution of the ray-by-ray solution. At the outer boundary, since $u(\tau = 0) \equiv v(\tau = 0)$, this is just

$$h(\tau = 0) = \left.\frac{H}{J}\right|_{\tau=0}. \tag{4.55}$$

Thus, the outer boundary equation is

$$\left.\frac{\mathrm{d}(fq\tilde{J})}{\mathrm{d}\tilde{\tau}}\right|_{\tau=0} = h(\tau = 0)\tilde{J}(\tau = 0). \tag{4.56}$$

The inner boundary ($r = R$) is treated similarly; however, because $\int u\,\mu \mathrm{d}\mu \neq H$, I_{core} from the ray-by-ray solution has to be employed here as well, noting that

$$H(\tau_{\max}) = \int_0^1 v\,\mu \mathrm{d}\mu = \int_0^1 I_{\mathrm{core}}\,\mu \mathrm{d}\mu - \int_0^1 u\,\mu \mathrm{d}\mu. \tag{4.57}$$

This results in

$$\left.\frac{\mathrm{d}(fq\tilde{J})}{\mathrm{d}\tilde{\tau}}\right|_{\tau_{\max}} = R^2 \int_0^1 I_{\mathrm{core}}\,\mu \mathrm{d}\mu - h(\tau_{\max})\tilde{J}. \tag{4.58}$$

The coefficients at the outer boundary are

$$\mathcal{C}_N = -\frac{f_{N-1}q_{N-1}}{\overline{q\chi}_{N,N-1}(r_{N-1} - r_N)} \tag{4.59}$$

$$\mathcal{B}_N = \frac{f_N q_N}{\overline{q\chi}_{N,N-1}(r_{N-1} - r_N)} + h_N \tag{4.60}$$

$$\mathcal{K}_N = \tilde{S}^{\dagger} \tag{4.61}$$

and at the inner boundary are

$$\mathcal{A}_1 = -\frac{f_2 q_2}{\overline{q\chi}_{1,2}(r_2 - r_1)} \tag{4.62}$$

$$\mathcal{B}_1 = \frac{f_1 q_1}{\overline{q\chi}_{1,2}(r_2 - r_1)} + h_1 \tag{4.63}$$

$$\mathcal{K}_1 = \int_0^1 I_{\mathrm{core}}\,\mu \mathrm{d}\mu. \tag{4.64}$$

The latter choice of coefficients is also revised in Section 5.2. The solution of this tridiagonal matrix scheme is again performed by efficient BLAS functions.

[4] The second Eddington factor is actually defined as the ratio $H(\tau = 0)/J(\tau = 0)$ at the outer boundary of an atmosphere (see Mihalas 1978, p. 157).

4.1.2 Iteration cycle II — Detailed solution of radiative line transfer

In the final iteration, a detailed radiative transfer method that does not suffer from the approximations of the first iteration cycle is used. This exact observer's frame solution is equivalent to the comoving frame solution and correctly treats the angular variation of opacities and emissivities. It spatially resolves the line profiles, which also treats multi-line effects correctly. Lifting the limitation of only radially dependent opacities requires the solution of two quadrants to allow both red and blue Doppler-shifted line opacities. While the blue shifted opacities arise from the matter approaching the observer in the first quadrant, the red shifted emissions occur in the part of the atmosphere receding from the observer (back hemisphere).

The method used here is an adaption of the method described in Pauldrach et al. (1990). It uses an integral formulation of the transfer equation and employs an adaptive micro-grid to ensure that the optical depth for each radius step does not exceed a $\Delta\tau = 0.3$. The radiative transfer equation can be approximated to a high level of accuracy by an analytic formula assuming a linear run of opacities and emissivities between the micro-grid points

$$I(\tau_0) = I(\tau_n)e^{-(\tau_n-\tau_0)} + \int_{\tau_0}^{\tau_n} S(\tau)e^{-(\tau-\tau_0)}\,\mathrm{d}\tau. \tag{4.65}$$

The integral is performed as a weighted sum on the micro-grid

$$\int_{\tau_0}^{\tau_n} S(\tau)e^{-(\tau-\tau_0)}\,\mathrm{d}\tau = \sum_{l=0}^{n-1}\left(e^{-(\tau_l-\tau_0)}\int_{\tau_l}^{\tau_{l+1}} S(\tau)e^{-(\tau-\tau_l)}\,\mathrm{d}\tau\right). \tag{4.66}$$

Each "sub-integral" is evaluated as

$$\int_{\tau_l}^{\tau_{l+1}} S(\tau)e^{-(\tau-\tau_l)}\,\mathrm{d}\tau = w_l^a S(\tau_l) + w_l^b S(\tau_{l+1}) \tag{4.67}$$

with the weights for the interval $\Delta\tau_l = \tau_{l+1} - \tau_l$

$$w_l^a = 1 - \frac{1-e^{-\Delta\tau_l}}{\Delta\tau_l}, \qquad w_l^b = \frac{1-e^{-\Delta\tau_l}}{\Delta\tau_l} - e^{-\Delta\tau_l}. \tag{4.68}$$

To resolve the line opacities and emissivities at their corresponding Doppler-shifts, all line profile functions $\phi_{ij}(\nu)$ are derived at each micro-grid point. Thus, effectively each individual line profile is resolved. The only quantities that are interpolated directly between the regular grid-points are those that vary slowly with radius, such as occupation numbers (determining the frequency-independent part of the line opacities and emissivities χ_{ij} and η_{ij}) and velocity field.

Using this method, the radiative transfer is solved twice for each frequency point: once for the continuum contribution to the opacity and emissivity and once for the total opacity/emissivity including lines and continuum. The ratios of the radiative quantities with

and without line contribution $B_J(\nu) = J_\nu / J_\nu^{\mathrm{cont}}$ and $B_H(\nu) = H_\nu / H_\nu^{\mathrm{cont}}$ are stored and used in the subsequent iteration blocks. Here only the continuum is derived following method I using B_H and B_J to obtain J_ν and H_ν relative to the new continuum. This method requires that the relevant quantities that influence the continuum transport (in particular, the temperature structure) do not change too much after the first iteration of detailed transport to avoid artificial contributions to the radiation field from this interpolation. The advantage of this method is that it allows the occupation numbers and radiation field to be iterated using only the computationally advantageous continuum transfer.

After the convergence of the model, a final run of the detailed method provides the emergent flux at the outer boundary for comparison with observed spectra.

4.2 Temperature structure

To derive a consistent temperature structure for the model, different methods can be used. The constraint for the temperature is that the total radiative energy in the atmosphere has to be conserved at all depth points. The line blocking, which is due to the presence of many optically thick lines, causes a back-reaction of the temperature called *line blanketing*. Qualitatively, the temperature gradient has to be steeper in the presence of large line opacities to still "drive" the same flux. In regions where the flux is not diffusive over the entire spectrum, no simple relationship between the temperature gradient and the flux exists. Therefore, the temperature at each depth point has to be computed explicitly.

As already mentioned in Section 3.4, two different view points exist to constrain the local gas temperature. On the one hand one can require the thermal balance of the electron gas (energy equation for the gas), on the other hand one could require the condition of radiative equilibrium (energy equation for the radiation field). Physically, both descriptions are equivalent because at the correct temperature both conditions are naturally fulfilled. Numerically, however, determining which description is more advantageous depends on the physical conditions.

4.2.1 Radiative equilibrium

In stationary stellar atmosphere models a formulation of the radiative balance between emission and absorption can be used that involves the radiative flux

$$\frac{1}{r^2}\int_0^\infty \frac{\partial r^2 H_\nu}{\partial r} \stackrel{!}{=} 0. \tag{4.69}$$

This is suitable if the total energy flux above the photosphere can be assumed to be a conserved quantity. In that case, the condition Eq. (4.69) can be used to derive the temperature at each depth point. In regions of supernova envelopes where a significant amount of γ-energy is deposited, however, this flux constraint is not fulfilled because, in those

regions, radiative energy is generated within the atmosphere. Therefore, the flux conservation methods are only of limited use for supernova envelopes.

NLTE Hopf-parameters

For optically thick regions ($\tau_{\mathrm{Ross}} \gtrsim 0.1$) in stellar models, the temperature is obtained using the "NLTE Hopf-function" described in Santolaya-Rey et al. (1997) and Pauldrach et al. (2001). This method determines the temperature structure that fulfills Eq. (4.69) from a parameterized correction function to the grey temperature (cf. Eq. (3.48))

$$T^4 = \frac{3}{4} T_{\mathrm{eff}}^4 \frac{\tilde{\tau}_{\mathrm{Ross}}}{\tau_{\mathrm{Ross}}} \left(\tilde{\tau}_{\mathrm{Ross}} + q_{\mathrm{N}}(\tilde{\tau}_{\mathrm{Ross}})\right) \tag{4.70}$$

where $\tilde{\tau}_{\mathrm{Ross}}$ is a sphericity corrected Rosseland optical depth

$$\mathrm{d}\tilde{\tau}_{\mathrm{Ross}} = -\chi_{\mathrm{Ross}} \left(\frac{R}{r}\right)^2 \mathrm{d}r \tag{4.71}$$

and q_N represents the parameterization to the spherical LTE Hopf function

$$q_{\mathrm{N}} = q_\infty + (q_0 - q_\infty) e^{-\gamma \tilde{\tau}_{\mathrm{Ross}}}. \tag{4.72}$$

The parameters q_∞, q_0, and γ are adjusted such that the total integrated flux is conserved (see Pauldrach et al. 1998). This method works reliably only as long as τ_{Ross} represents the dominating factor determining the flux. In conditions where this is not the case (e.g., by the presence of the opacity of strong saturated lines, which depends only weakly on the temperature) this method fails.

In SN Ia, the calculation τ_{Ross} is not a good representation of the frequency-dependent optical depths because the opacities vary strongly with frequency. Therefore, compared to stars, in SN Ia this method fails already at larger mean optical depths.

Flux conservation from a modified Lucy-Unsöld procedure

For the purpose of testing, we also implemented another method based on the flux conservation requirement, which follows the Lucy-Unsöld procedure (cf. Lucy (1964), see also Mihalas (1978, p. 174)). This procedure essentially derives corrections to the local temperature based on the deviation of the calculated flux from the total input flux. As in the NLTE-Hopf-parameter method, this method also implies that the flux is diffusive overall; that is, this method is also only applicable at large optical depths and for conditions where the flux is dominantly determined by the temperature gradient. For test-runs of O-star models, this method obtains the same solution as the NLTE-Hopf-parameter method. For Type Ia Supernova atmospheres, the method did not find a suitable solution for the temperature structure for the reasons given above.

4.2.2 Local radiative equilibrium

As an alternative, the formulation given in Eq. (3.105)

$$\int_0^\infty \chi_\nu (J_\nu - S_\nu)\, \mathrm{d}\nu \stackrel{!}{=} 0$$

is used directly because it does not rely on the flux between depth points but rather on the mean intensity on the grid points. (This has the additional advantage that J_ν is known to a higher degree of accuracy because it is directly calculated in the radiative transfer solution and does not depend on an interpolation between depth points.) As mentioned in Section 3.4, this is in principle equivalent to the thermal balance method; however, it tends to be numerically more stable in optically thick regions and fail in optically thin regions where the radiation field is mostly decoupled from the local temperature.

4.2.3 Thermal balance of electrons — Heating and cooling rates

In supernova envelopes, the temperature is determined from the balance of energy gain and loss to the electron gas. (This is often called "heating" and "cooling" even if these terms are somewhat misleading. It primarily determines the gain and losses of energy of the gas, but does not necessarily induce the temperature change implied.) The correct temperature is constrained by the requirement that all energy gains Γ to the gas cancel the energy losses Λ:

$$\Gamma - \Lambda = 0 \tag{4.73}$$

The rates Γ and Λ are obtained from the processes that couple to the thermal pool of the gas: free–free rates, collisional bound–free and bound–bound rates, and radiative bound–free rates. Radiative bound–bound transitions (line scattering) do not change the energy of the gas.

The basic procedure is to find the correct $T(r)$ that fulfills the balance Eq. (4.73) based on the heating and cooling rates described in Section 3.4.1. The functional dependence between the rates and the temperature is, in general, complicated because the change in temperature affects the radiation field, the occupations numbers, and the transition rates in a complex way. One way of solving this is to also derive the derivatives of Γ and Λ and solve for $\Gamma - \Lambda = 0$ with a root-finding algorithm such as the Runge-Kutta procedure. However, because the rates also contain the occupation numbers, there is no analytical expression for the needed derivatives. One can approximate this is by using a linearization approach as described by Kubát et al. (1999). To avoid time-consuming iterations, we chose a different approach and use the following algorithm: from the mismatch of heating and cooling, the general direction into which the temperature has to be adjusted is determined. Then the basic step size is given by the mismatch normalized to the sum of heating and cooling rates at each radius point. In addition, the step size in each iteration is accelerated depending on the direction of the current and the previous iteration: if both point

into the same direction, the acceleration factor is increased by 50%, while it is decreased by the same amount if two successive iterations point in different directions. To keep the iteration stable and avoid large jumps, only temperature changes of 10% from iteration to iteration are allowed. This scheme turns out to be fairly efficient and is able to determine a stable temperature within a few iterations.

The temperature at R = 1

At the innermost depth point any temperature correction that relies on local conditions is not reliable because the radiation field at this point can be expected to depend significantly on the boundary condition for the radiative transfer. In addition, if the optical depth over the whole spectrum is high, the radiation field is very close to B_ν. In this case, the heating-cooling balance cannot be used because the rates cancel at any temperature and the determination of an absolute temperature is impossible.

To overcome this problem, the temperature at the innermost point is determined directly from the temperature gradient between the first point and the second point by requiring the correct total flux to be generated at the inner boundary

$$\int_0^\infty H_\nu(R) \stackrel{!}{=} H_{\mathrm{lum}} \tag{4.74}$$

$$\Rightarrow \qquad \frac{L}{16\pi^2} \stackrel{!}{=} \int_0^\infty H_\nu^0 + \left(\tfrac{1}{2} I_\nu^0 - h J_\nu\right) \mathrm{d}\nu \tag{4.75}$$

(see Eq. (5.12)). This assumes that the primary temperature dependence of the boundary flux is described by the term $\frac{\mathrm{d}B_\nu}{\mathrm{d}T}$. This procedure incorporates the flux correction of Section 5.2.2 directly into the temperature. Note that in cases where the flux-correction would be high, the temperature at the first point is less meaningful in terms of describing the physical conditions. Therefore "unphysical" jumps in T may occur here if the frequencial H_ν^0 does not properly represent the flux that would be achieved corresponding to the physical conditions. Of course, one should try to keep this inconsistency as small as possible, for example, by going to larger optical depths. In SN Ia, however, even at large optical depths an analytic expression for the flux will not represent the physical conditions sufficiently enough to avoid some inconsistecy. It also has to be kept in mind that this method still relies on the correctness of the temperature at the second point, which may be affected by the same insufficiency as $T(R)$ if the optical depth is low.

4.2.4 Effective temperature, radius, and total luminosity

The effective temperature T_{eff} of an object is defined as the temperature of a black body spectrum that would emit the same total flux from a plane-parallel atmosphere

$$4\pi H_0 = \pi B(T_{\mathrm{eff}}) \quad \Rightarrow \quad H_0 = \frac{\sigma_R T_{\mathrm{eff}}^4}{4\pi} \tag{4.76}$$

with the total integrated flux from the object H_0 and the Stefan-Boltzmann constant $\sigma_B = 2\pi^5 k_B^4/(15h^3c^2) \approx 5.67 \times 10^{-5}\,\mathrm{erg\,cm^{-2}s^{-1}deg^{-4}}$.

The total luminosity of the object is defined as the total radiation energy emitted from the object:

$$L = 4\pi r^2\, F_0(r) = 4\pi r^2\, 4\pi H_0(r). \tag{4.77}$$

Assuming the conservation of radiative energy (i.e., not considering the additional energy input within the ejecta by γ-rays) this holds at any radius – and in particular at the photospheric radius r_{eff} referred to by T_{eff}. Thus, one can write

$$H_0(r_{\mathrm{eff}}) = \frac{\sigma_R T_{\mathrm{eff}}^4}{4\pi}. \tag{4.78}$$

For the flux at the innermost radius R of the model, it follows that

$$H_0(R) = \left(\frac{r_{\mathrm{eff}}}{R}\right)^2 \frac{\sigma_R T_{\mathrm{eff}}^4}{4\pi} = \frac{L}{16\pi^2 R^2}. \tag{4.79}$$

Note that, in contrast to the effective temperature, the total luminosity itself does not contain any information on the spectral characteristics. (Although this is less true for SN Ia than for a star because the SN Ia-spectrum is far from Planckian.)

In models of hot stars, the radius of the photosphere differs by less than a few percent from the innermost radius (however the situation may already become different in models of Wolf-Rayet stars with high mass loss). In supernova calculations, the situation can be quite different where the very shallow density structure causes the photosphere to be less meaningful than it is in stars; in supernovae, the optical depth to radius mapping varies much more strongly with wavelength. Thus, in supernova models, the innermost radius point, which has to be chosen such that a reasonable optical depth > 1 is reached in *all* wavelengths, will differ significantly from the photospheric radius. Care is needed to refer the effective temperature and related quantities to the correct radius. In practice, for flux-related quantities that refer to the effective temperature, T_{eff} has to be extrapolated to the innermost radius point[5]. In supernova models, the luminosity L is usually used as input that determines the effective temperature at $r(\tau_{\mathrm{Ross}}= 2/3)$ (which is essentially determined by the density distribution of the adopted explosion model). Thus, T_{eff} is a result of the calculation and may vary through the iterations.

4.3 Atomic data

The accuracy of the radiative transfer model and in particular of the calculated occupation numbers crucially depends on the quality of the atomic data used for the NLTE computations. Accurate atomic models are an essential prerequisite for a realistic model. The

[5] This does not necessarily have to be the physical temperature at this point because the physical conditions are most likely different.

atomic models used in this project have been mainly computed by the hot star group at the Universitätssternwarte München using the SUPERSTRUCTURE program (Eissner et al. 1974, Nussbaumer & Storey 1978), which employs the configuration-interaction approximation to determine wave functions and radiative data. So far the data include the 149 most important ionization stages of 26 elements (H to Zn, except Li, Be, B, and Sc, which are irrelevant due to their low abundances). The data contains a total number of about 5000 levels (with "packed" fine-structure levels) for which the occupation numbers are directly computed. This corresponds to more than 30 000 radiative bound-bound transitions. In addition, 20 000 individual transition probabilities for di-electronic recombinations and auto-ionizations are included in the data. For the blocking and the spectrum calculations, the individual lines of the multiplets are considered explicitly, amounting to a total of over 4 000 000 lines[6].

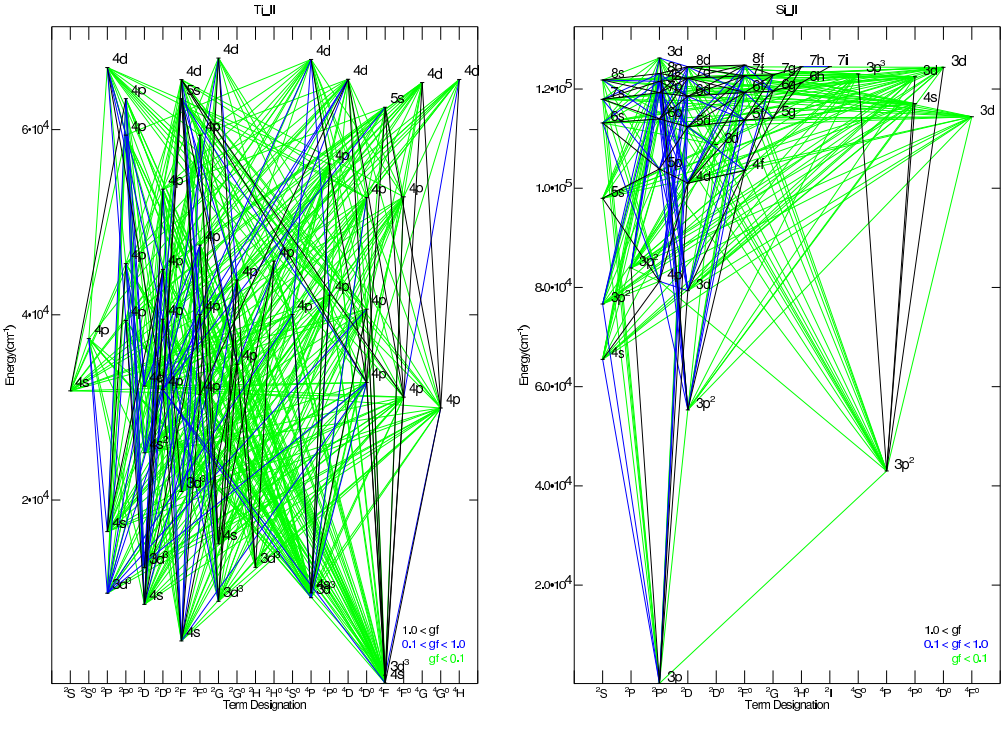

Figure 4.7: Grotrian diagram for the Ti II and Si II ions used in the NLTE calculation.

In addition, line data from the Kurucz (1992) line list have been incorporated; in total about 20 000 lines have been added to the SUPERSTRUCTURE data, in particular for ions of Mn, Fe, Co, and Ni. These lines concern transitions to even higher levels than those that

[6]The SUPERSTRUCTURE calculations use many more excited levels than the 50 explicit levels taken into account in the NLTE calculations. The long line list used for blocking includes the line transitions to highly excited levels by estimating the occupation number of the upper level from the two-level approximation relative to the known occupation number of the lower level.

have been used in the SUPERSTRUCTURE calculations. Another 4 466 lines as well as almost 2000 data sets for photoionization data have been incorporated from the Opacity project (Seaton et al. 1994, Cunto & Mendoza 1992). Additionally, 1 300 data sets of collisional data from the Iron project (Hummer et al. 1993) are used. As an example, Figure 4.7 shows the Grotrian diagram for the Ti II and Si II ions as used in the code.

For studies of supernova spectra at later epochs where nebular lines from forbidden transitions become relevant, those lines still have to be incorporated into the data base. This is currently being worked on by our group. In the current work, only early time spectra before and shortly after maximum light are considered where lines from forbidden transitions are irrelevant.

4.4 γ-ray deposition

In SN Ia the dominant source of radiative energy is the absorption of high-energetic γ-rays (and at later epochs positrons) due to the ^{56}Ni and ^{56}Co decay by the matter. Figure 4.8 shows the generation and deposition of γ-ray energy for the W7 model at 18 days after explosion. The deposition has been derived using the basic light curve code presented in Cappellaro et al. (1997). At a later stage of the project, this deposition will be implemented in the NLTE calculation by means of emission and heating terms (Hultzsch, priv. comm.).

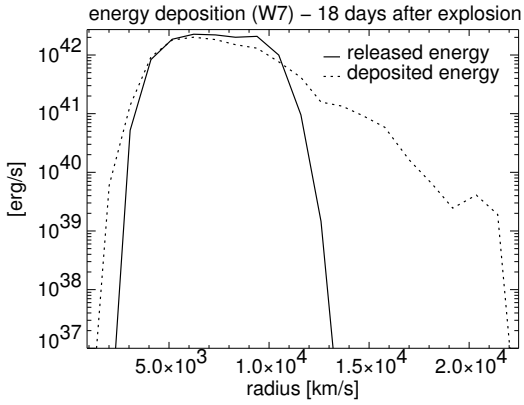

Figure 4.8: Generation and deposition of γ energy as calculated using a basic light curve code (Cappellaro et al. 1997). This deposition is currently not considered in the NLTE models.

In the current work, this additional source of radiation has been neglected; it is assumed that the entire luminosity is generated below the lower boundary of the computational grid. A prerequisite for including this energy deposition is that the model is reliably energy conserving; with the additional energy deposition, the flux in the atmosphere is intrinsically

not conserved. This flux constraint, however, is the most significant indication needed to judge the quality of energy conservation in the NLTE model. At the current stage of the project, the major difficulty is to guarantee that the energy flows between the different energy pools are correctly represented in the model (see Section 3.4); thus, we did not consider γ-ray deposition for now. As can be seen in Figure 4.8, the fraction of γ-rays that are deposited above $\sim 10\,000$ km/s is small enough for this approximation to be sufficient. Therefore, models of early epochs until around maximum will not be seriously affected by this approximation. Nevertheless, for a more detailed analysis — in particular for later epochs — this deposition will have to be considered. Additionally, the non-thermal excitation from γ-rays may affect the appearance of spectral features (Kozma & Fransson 1992, Eastman & Pinto 1993, Höflich et al. 1995).

5 Steps toward a consistent description of NLTE in supernovae

5.1 The starting point

As a first step, basic modifications to the NLTE code were necessary to incorporate supernova-specific requirements in the description of the physical conditions.

Density and radius

A basic modification was to add a routine to read in the hydrodynamic structure from the data of an external explosion model. In all cases a homologous expansion law is assumed, which is justified as soon as the interaction between particles is negligible and the matter is freely coasting. This means that the velocity v is proportional to the radius:

$$v \propto r \qquad \Rightarrow \qquad \frac{\mathrm{d}v}{\mathrm{d}r} = \text{const.} \tag{5.1}$$

Consequently, the velocity coordinate is independent of the time after explosion and is more useful for the description of the density and abundance profiles than an absolute radius coordinate. The other benefit of this simple relationship between radius and velocity is that the Doppler-shift of a photon between two volume elements is time-independent. Alternatively, mass shells $\int m\,\mathrm{d}r$ are also used, in particular for the description of hydrodynamic properties of explosion models.

The most commonly used explosion model for spectral fits of SN Ia is the one dimensional, parameterized W7 explosion model (Nomoto et al. 1984, Thielemann et al. 1986). The density of the explosion model is read as a function of radius or velocity and, if required, homologously expanded to the desired epoch. The only parts of the hydrodynamic structure that are visible in the spectrum are those that lie outside the boundary where the spectrum becomes optically thick; thus, it is not possible nor is it necessary to calculate the radiative transport for the entire object. The radius grid has to extend sufficiently deep into the ejecta to ensure that the choice of the innermost point does not influence the emergent spectrum. As discussed in Section 5.2, this choice is not straightforward in SN Ia because the “photospheric” radius is not as clearly defined as in a stellar object and varies strongly with frequency.

Composition

The next basic modification to the NLTE code was to implement the possibility of varying the composition within the ejecta, a situation that essentially never occurs in stellar winds. A stratified composition has been implemented; however, most testing has been done using a homogeneously mixed composition because for the first step a stratified abundance adds additional complications if layers with significantly different abundances of elements (in particular iron group elements) cause large jumps in the radial opacity distribution. These jumps may result in additional numerical problems that can only be solved if the homogeneous composition works reliably.

For models of epochs around and after maximum light, the effects of a stratified composition are generally small because overall the outer low density layers do not influence the spectrum anymore. In such epochs, only a few specific line features require a stratified abundance set to fit the correct widths (M. Stehle, priv. comm., see also Chapter 6).

Number of ionization stages

In spite of the much larger temperature range in hot stars, the number of relevant ionization stages that need to be considered simultaneously is smaller than in supernova. This is due to the much steeper density increase in the photosphere of stars, which keeps the degree of ionization low even at high temperatures. In the Saha equation (cf. Eq. (3.2)) the occupation of the lower ionization stage has a linear relationship with the electron density, but an inverse relationship with the temperature.

In the standard version of the WM-basic atmosphere code, only the three dominating ionization stages for each element are chosen for the calculation. For supernova models this has been increased to four, and up to five simultaneous ionization stages.

First results

Figure 5.1 shows the synthetic spectrum of one of the first models obtained after the basic adaption of the new code version. This model uses the W7 density stratification with a homogenized composition that roughly follows the W7 composition in the outer layers. It can be seen that the synthetic spectrum follows the observation reasonably well considering that this was not intended to be an exact fit to this object; the idea was rather to set up a model as a starting point for further analysis. For comparison, Figure 5.2 shows the spectrum obtained from an earlier version of the code by Pauldrach et al. (1996) who investigated the line blocking effects in the UV. (Note the logarithmic scale in this plot.)
Even though the model in Figure 5.1 already looks like a reasonable fit, some significant problems are visible in the spectrum. In the red and infrared wavelength bands, beyond the strong Si II feature, the model shows significantly more flux than the observation; in particular, it is not able to follow the slope of the pseudo-continuum in this region. Also

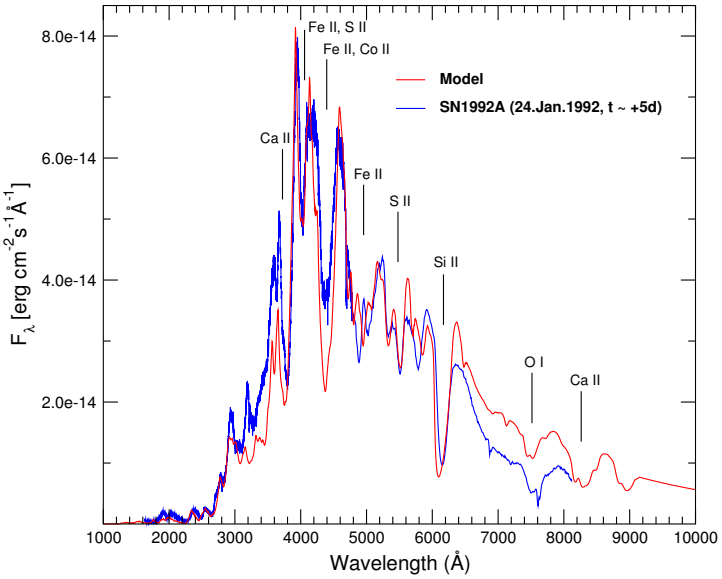

Figure 5.1: Synthetic spectrum compared to the observed spectrum of SN1992A at ~ 5 days maximum (Kirshner et al. 1993). Some important ions contributing to particular features are indicated.

the absorption features at ~4500 Å appear to be too deep in the synthetic spectrum or, with a different interpretation, the peaks are too large. (The absolute scale of the flux is not so strongly constrained. It is primarily set by the distance of the object, which is usually not known to better than a few percent.)

The interpretation of these problems is that the model fails in wavelength regions where the opacity is dominated by electron scattering throughout the ejecta. In such wavelength bands, the radiation that emerges at the outer boundary of the model is almost entirely determined by the assumption that it is used at the inner boundary: Thomson scattering only affects the direction of the radiation, but not its spectral properties. This means that all radiation observed at these wavelengths in nature has to be generated by a comparably small amount of true processes relative to pure electron scattering.

It is worthwhile to note that the offset in the red part of the spectrum is a problem that also occurs in the work of other groups using different approaches. For example, see the discussion in Stehle (2004) who adopt a fixed photosphere with a Planckian continuum at the lower boundary. The problem is also visible in Nugent et al. (1997) and Lentz et al. (2001) who use a more elaborate method for the solution of the radiative transfer than Stehle (2004). They consider the γ-ray deposition within the atmosphere, which partly covers the effects of the inner boundary because the total luminosity emitted there is only a fraction of the total luminosity emerging from the outer shells.

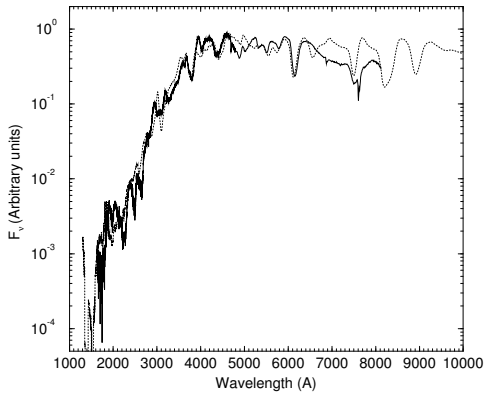

Figure 5.2: Synthetic spectrum of SN1992A by Pauldrach et al. (1996).

5.2 A modified inner boundary for the radiation transfer at NLTE conditions

5.2.1 The "photosphere" of SN Ia

A major difficulty in constructing a consistent radiative transfer model for a SN Ia is that the ejecta do not have a clear boundary like the photosphere in stars. The stellar photosphere is formed due to the exponential density increase at the bottom of the atmosphere. This forms a well defined radius because large optical depths are reached in all wavelength bands within a fairly short distance — mainly due to continuum opacity (free-free and bound-free). In all explosion models for supernovae, the ejecta show only a moderate increase of density toward the inside. Consequently, the radius at which significant optical depths are reached depends strongly on the wavelength. Figure 5.3 shows the radius at which the optical depth on the radial ray becomes larger than unity as a function of wavelength for three different objects. The left panel shows the clearly defined photosphere of a stellar atmosphere. In contrast, the "photosphere" of a SN Ia has a wide range of radii. It reaches far out in the UV wavelength regions where the lines of low metal ions dominate. The optical depth in red wavelengths of about 5000 Å where only a few lines are present is mainly due to electron scattering; $\tau = 1$ is barely reached at all. The middle panel shows the situation in a Type II supernova where the presence of the hydrogen and helium continuum provides a clear photosphere except in the UV region where the lines start to dominate the continuum further out. An additional complication for radiative transfer models of SN Ia is shown in the right panel. The prominent peak at $\sim$8000 Å are due to the Ca II IR triplet. These lines dominate the opacity throughout the atmosphere. Due to the Doppler-shift of the lines, at a given wavelength the opacity can be largest in the middle of the radius grid and drop in both directions. In addition, the overall line opacity is lower to-

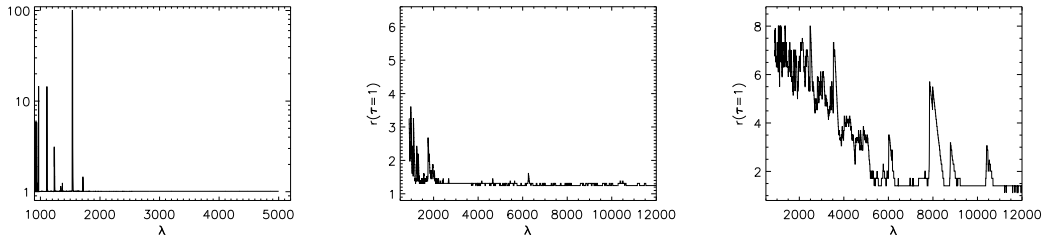

Figure 5.3: The radius (in units of the innermost radius) at which the radial optical depth from the outside in becomes larger than unity as a function of wavelength. The left panel shows the clearly defined photosphere of a stellar atmosphere (with the exception of a few strong lines). The middle panel shows a SN II atmosphere that contains hydrogen and helium. The right panel shows the situation in a SN Ia. (The radii have not been interpolated for this plot, thus at each wavelength, the first optically thick point from outside is plotted.)

ward hotter and denser regions because the lower ionization stages have significantly more lines than higher ones. Figure 5.4 shows the logarithm of the total opacity as a function of velocity and wavelengths for a SN Ia model (epoch: 25 days after explosion).

5.2.2 Diffusion approximation at the inner boundary

A significant problem for numerical radiative transfer models arises when solving the transfer equation. To solve the equation, a boundary condition at both sides of the computational grid has to be specified. At the outer boundary, the condition is that there is no incoming radiation and thus $I^- \equiv 0$. At the inner boundary, however, one has to specify the spectral characteristics of a radiation field that is consistent with the physical conditions at this region of the atmosphere. In a stellar photosphere, this boundary is clearly defined because the system reaches LTE conditions, which constrain the radiation field solely by macroscopic thermodynamic quantities. The conditions inside supernova ejecta are far from thermodynamic equilibrium, thus there is no clear analytical solution that would specify this radiation field. In addition, the properties of the ejecta are such that it does not help to just choose a smaller inner radius because the density increases too slowly to reach LTE conditions over the entire spectrum. In addition, one would also have to take into account the time-dependent trapping of photons in the wavelength region with large opacity if the mean escape time of photons increases to on the order of the expansion time scale.

The ejecta of early SN Ia form an intermediate object between an extended stellar atmosphere and a planetary nebula. For both extreme cases the choice for the inner boundary is clear. For the star, the LTE diffusion approximation (cf. Section 3.2.4) is a suitable choice. For a gaseous nebula, the incident radiation field from the illuminating star naturally defines the radiation field at the inner boundary. In SN Ia neither of these choices can be

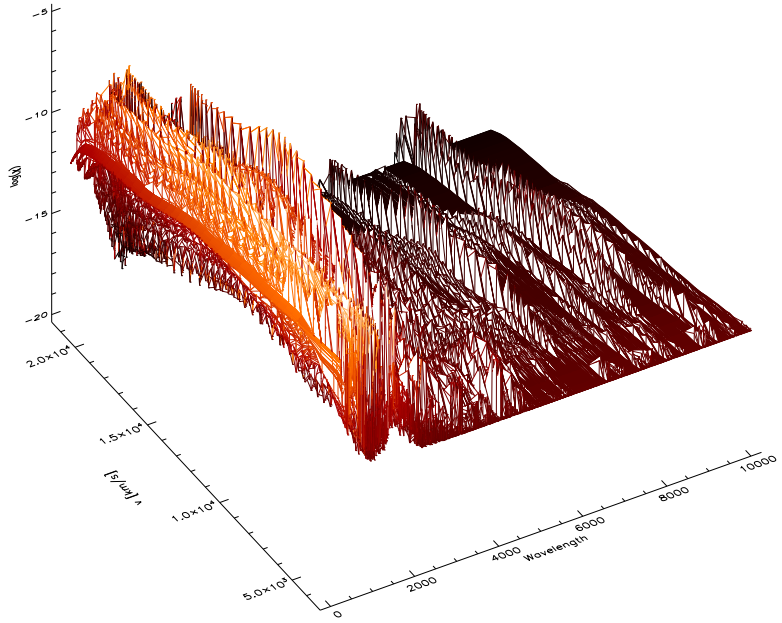

Figure 5.4: Logarithm of the total opacity in a SN Ia model (sampling iteration) versus velocity and wavelength. Note that the line opacity *decreases* toward the inside (front) because higher ionization with less lines stages dominate.

strictly applied.

In the following, we describe a method that allows some of the major assumptions that enter into the derivation of the diffusive inner boundary to be dropped and that includes some effects of NLTE.

The commonly used boundary condition for the radiative transfer is derived from the Eddington approximation, which is suitable for LTE conditions. To solve the equation system of the ray-by-ray solution, as discussed in Section 4.1.1, one has to make an assumption about the incoming radiation I_ν^+ at the core. It should be chosen such that it describes the radiation field under the present physical conditions as accurately as possible. Ideally, the expression for the boundary equation is an analytic extrapolation of the radiation field at the innermost points.

Applying a harmonic expansion for I^+ leads to the expression (see, e.g., Pomraning 1973)

$$I^+(\nu,\mu) \approx I^0(\nu) + \mathbf{I_1}(\nu) = I^0(\nu) + 3\mu I^1(\nu) \tag{5.2}$$

where the zeroth term $I^0(\nu)$ is isotropic and the first term has an angular dependence proportional to μ. Since I^1 has the characteristics of a flux, we define $H^0(\nu) \equiv I^1$. (Note that this expansion also implies that the I^0 term is assumed to dominate over the first term.)

To get an analytical expression for the two terms, the Taylor expansion of S_ν for large τ (see Eq. (3.40) in Section 3.2.4) is used

$$S_\nu(\tau'_\nu) = \sum_{n=0}^{\infty} \frac{\partial^{(n)} B_\nu(\tau_\nu)}{\partial \tau_\nu^{(n)}} \frac{(\tau'_\nu - \tau_\nu^n)}{n!} \tag{5.3}$$

which leads to the terms

$$I^0(\nu) = B_\nu(T) \qquad \text{and} \qquad I^1(\nu) = H^0(\nu) = \frac{1}{3}\frac{\mathrm{d}B_\nu(T)}{\mathrm{d}\tau} = -\frac{1}{3}\frac{1}{\chi_\nu}\frac{\partial B_\nu}{\partial T}\frac{\mathrm{d}T}{\mathrm{d}r}. \tag{5.4}$$

The expansion Eq. (5.3), and therefore Eq. (5.4), is applicable if the radiation field is thermalized (i.e., the mean free paths of photons are much shorter than any significant hydrodynamic length scale). In SN Ia, however, we know that this condition is not fulfilled over the full spectrum. Hence, the use of Eq. (5.4) leads to incorrect spectral properties of the radiation field at the inner boundary. The inconsistency between the radiation field and the physical state of the matter caused by enforcing a thermal radiation field at the core boundary leads to spurious results in the rate equations and, in particular, in the heating and cooling rates for the temperature determination. This inconsistency partially resulted in convergence problems in the temperature iteration. Therefore, part of this work focused on deriving an analytical expression for the radiation field at the inner boundary that more accurately agrees with the physical conditions in SN Ia and reproduces a better slope of the pseudo-continuum in the red and infrared wavelengths.

In the standard implementation, the (lower) boundary equations for the ray-by-ray solution (core rays) is (cf. Eq. (4.28))

$$\left.\frac{\mathrm{d}u}{\mathrm{d}\tau}\right|_{\tau_{\max}} = I^+ - u \tag{5.5}$$

and the solution of the moment equations Eq. (4.58)

$$\left.\frac{\mathrm{d}(fq\tilde{J})}{\mathrm{d}\tilde{\tau}}\right|_{\tau_{\max}} = R^2 \int_0^1 I^+ \mu \mathrm{d}\mu - h(\tau_{\max})\tilde{J} \tag{5.6}$$

are therefore given as

$$\left.\frac{\mathrm{d}u}{\mathrm{d}\tau}\right|_{\tau_{\max}} = I^0 + 3\mu H^0 - u(\tau_{\max}) \tag{5.7}$$

$$\left.\frac{\mathrm{d}(fq\tilde{J})}{\mathrm{d}\tilde{\tau}}\right|_{\tau_{\max}} = \left(\tfrac{1}{2}I^0 + H^0\right)R^2 - h(\tau_{\max})\tilde{J}(\tau_{\max}) \tag{5.8}$$

with all variables named as in Section 4.1.1, omitting the index ν.

Flux correction

To constrain the total flux at the inner boundary, the frequency integrated input flux $\int_0^\infty H_\nu^0 \,\mathrm{d}\nu$ is compared to the total input flux $H_0 = L/(16\pi^2 R^2)$ giving a (frequency-independent) scaling factor for $H^0(\nu)$ (see Mihalas 1978, p.252)

$$FC = \frac{H_0}{\int_0^\infty H_\nu^0 \,\mathrm{d}\nu} = \frac{\frac{L}{16\pi^2 R^2}}{-\frac{\mathrm{d}T}{\mathrm{d}r}\int_0^\infty \frac{1}{\chi_\nu}\frac{\mathrm{d}B_\nu(T)}{\mathrm{d}T}\,\mathrm{d}\nu}. \tag{5.9}$$

In the formulation of Eq. (5.4), this effectively represents a correction to the temperature gradient between the first two radius points. (In Section 4.2.3 the temperature of the innermost point is directly determined from the flux-correction factor.)

With respect to the moment equation for the flux at the inner boundary, however, it has to be noted that the derived flux is actually

$$H_\nu(R) = \int_0^1 \left(I_\nu^0 + 3\mu H_\nu^0\right)\mu \,\mathrm{d}\mu - h_\nu J_\nu = H_\nu^0 + \left(\tfrac{1}{2} I_\nu^0 - h_\nu J_\nu\right). \tag{5.10}$$

Thus, constraining the flux by adjusting H_ν^0 only with respect to H_0 implicitly assumes that the second term in Eq. (5.10) vanishes, which requires

$$J_\nu(R) = I_\nu^0 = B_\nu \quad \text{and} \quad h_\nu = \tfrac{1}{2}. \tag{5.11}$$

As can be seen in Figure 5.5, even for the D40 star model (cf. Pauldrach et al. 2001)

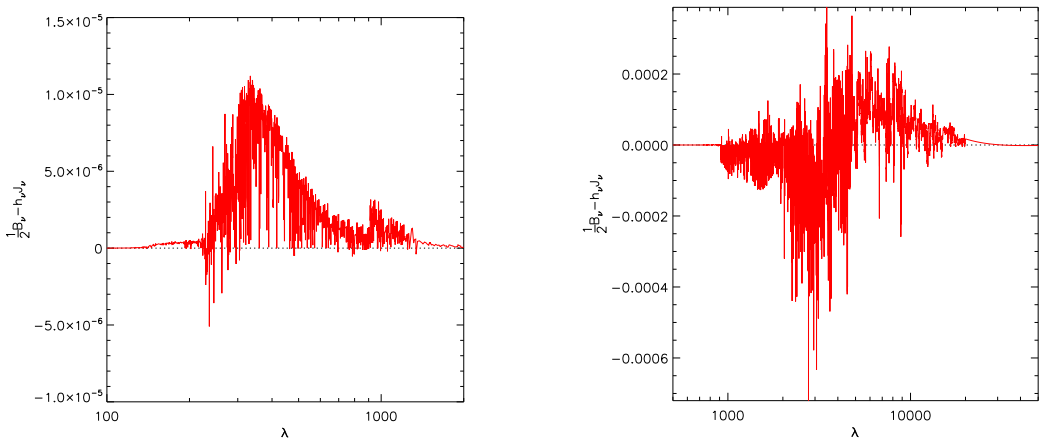

Figure 5.5: The term $\frac{1}{2}B_\nu - h_\nu J_\nu$ at the inner boundary (see text). *Left:* O-star model D40 (Pauldrach et al. 2001); *Right:* SN Ia model. Note the different y-scales in these plots.

this condition is not exactly fulfilled. In that case, even though the deviations are certainly negligible, there is a much stronger effect in SN Ia (left panel in Figure 5.5) leading to a significant discrepancy between FC and the actually derived flux. For the modifications

proposed in the next section, the level of consistency has to be such that these effects cannot be neglected. Therefore, the correct flux correction factor has to be

$$FC = \frac{\frac{L}{16\pi^2 R^2} - \int_0^\infty \left(\frac{1}{2} I_\nu^0 - h_\nu J_\nu\right) \mathrm{d}\nu}{\int_0^\infty H_\nu^0 \, \mathrm{d}\nu}. \tag{5.12}$$

With this formulation, it is now possible to achieve $FC = 1$ *and* the correct flux at $r = R$.

Note, the expression Eq. (5.10) implicitly contains the assumption of thermalization; only then is the degree of isotropy given that is necessary to make the expansion Eq. (5.2) meaningful, neglecting quadratic and higher order terms.

5.2.3 $\mathbf{I}^+$ for a non-thermal radiation field at the inner boundary

In this section, we will consider modifications to the inner boundary that allow deviations of the radiation field from thermal equilibrium conditions, which better reflects the physical situation in SN Ia. This becomes increasingly important for models of later epochs, as long as the luminosity emitted at the boundary is still significant compared to the flux originating from the γ-ray energy deposition above that boundary.

All modifications have to be carried out in such a way that, in the limit of LTE-conditions at the inner points, the standard diffusive boundary condition Eq. (5.4) is retained. While it will not be possible to determine a boundary condition entirely free of analytical approximations because the model would be not sufficiently constrained, some of the assumptions entering into Eq. (5.4) can be released without affecting the stability of the solution.

Starting from Eq. (5.2) one can release the assumption of strictly thermal conditions by allowing deviations of the terms $I^0(\nu)$ and $\mathbf{I_1}(\nu)$ from the Planck function. Thus, instead of Eq. (5.4) we set more generally

$$I_\nu^+ = J_\nu^0 + 3\mu H_\nu^0 \tag{5.13}$$

with an intensity term J_ν^0 and a flux term H_ν^0 to be determined as follows.

Instead of the expansion of S_ν, we now start from a general expression for the source function, which explicitly takes into account a contribution from Thomson scattering

$$S_\nu = (1 - \beta_\nu) B_\nu + \beta J_\nu \qquad \text{with} \qquad \beta_\nu = \frac{\chi_\nu^{\text{Thoms}}}{\chi_\nu^{\text{Thoms}} + \chi_\nu^{\text{true}}}. \tag{5.14}$$

From the moment equations in spherical symmetry Eq. (3.38), one then gets

$$\frac{\mathrm{d}^2 \left(q_\nu f_\nu \tilde{J}_\nu\right)}{\mathrm{d}\tilde{\tau}_\nu^2} = \frac{(1 - \beta_\nu)}{q_\nu} \left(\tilde{J}_\nu - \tilde{B}_\nu\right) \tag{5.15}$$

which can be solved analytically by rewriting it to

$$\frac{\mathrm{d}^2}{\mathrm{d}\tilde{\tau}_\nu^2} \left(q_\nu f_\nu \left(\tilde{J}_\nu - \tilde{B}_\nu\right)\right) = \frac{1 - \beta_\nu}{q_\nu^2 f_\nu} \left(q_\nu f_\nu \left(\tilde{J}_\nu - \tilde{B}_\nu\right)\right) \tag{5.16}$$

under the assumption that

$$\frac{\mathrm{d}^2 q_\nu f_\nu \tilde{B}_\nu}{\mathrm{d}\tilde{\tau}_\nu^2} \equiv 0 \qquad \text{and} \qquad \frac{1-\beta_\nu}{q_\nu^2 f_\nu} \approx \text{const.} \tag{5.17}$$

The first assumption can be justified by considering only up to first order terms in an expansion of $q_\nu f_\nu \tilde{B}_\nu$ in $\tilde{\tau}_\nu$. The second assumption is not strictly fulfilled, however in practice a representative mean value $\left\langle (1-\beta_\nu)/(q_\nu^2 f_\nu) \right\rangle$ is used. The general solution for J_ν in Eq. (5.16) is then derived to

$$\begin{aligned} q_\nu f_\nu \tilde{J}_\nu &= q_\nu f_\nu \tilde{B}_\nu + C_\nu \, e^{-\sqrt{\left\langle \frac{1-\beta_\nu}{q_\nu^2 f_\nu} \right\rangle} \tilde{\tau}_\nu} + C'_\nu \\ \Rightarrow \qquad J_\nu &= B_\nu + \frac{C_\nu}{q_\nu f_\nu r^2} \, e^{-\sqrt{\left\langle \frac{1-\beta_\nu}{q_\nu^2 f_\nu} \right\rangle} \tilde{\tau}_\nu} + \frac{C'_\nu}{q_\nu f_\nu r^2} \end{aligned} \tag{5.18}$$

with integration constants C_ν and C'_ν to be determined. Given the condition that $\tilde{\tau} \to \infty$, $\tilde{J}_\nu = \tilde{B}_\nu$ has to be obtained. It follows that $C'_\nu \equiv 0$.

Using this result to determine the flux term H^0 from the moment equation Eq. (3.37)

$$\left. \frac{\mathrm{d}\left(q_\nu f_\nu \tilde{J}_\nu\right)}{q_\nu \bar{\chi}_\nu \mathrm{d}r} \right|_{\tau=\tau_{\max}} = -\tilde{H}_\nu \tag{5.19}$$

leads to

$$\tilde{H}_\nu^0 = \frac{\mathrm{d}}{\mathrm{d}\tilde{\tau}_\nu}\left(q_\nu f_\nu r^2 J_\nu\right) = \frac{\mathrm{d}}{\mathrm{d}\tilde{\tau}_\nu}\left(q_\nu f_\nu r^2 B_\nu\right) - C_\nu \sqrt{\left\langle \frac{1-\beta_\nu}{q_\nu^2 f_\nu} \right\rangle} \, e^{-\sqrt{\left\langle \frac{1-\beta_\nu}{q_\nu^2 f_\nu} \right\rangle} \tilde{\tau}_\nu}. \tag{5.20}$$

For the first term one derives the expression

$$\begin{aligned} \frac{\mathrm{d}}{\mathrm{d}\tilde{\tau}_\nu}\left(q_\nu f_\nu r^2 B_\nu\right) &= \frac{\mathrm{d}(r^2 q_\nu)}{\mathrm{d}\tilde{\tau}_\nu} f_\nu B_\nu + r^2 q_\nu \left(\frac{\mathrm{d} f_\nu}{\mathrm{d}\tilde{\tau}_\nu} B_\nu + f_\nu \frac{\mathrm{d}B_\nu}{\mathrm{d}\tilde{\tau}_\nu} \right) \\ &= \left\{ -\left(\frac{3f_\nu - 1}{q_\nu \chi_\nu r} - \frac{\mathrm{d} f_\nu}{\mathrm{d}\tilde{\tau}_\nu} \right) B_\nu + f_\nu \frac{\mathrm{d}B_\nu}{\mathrm{d}\tilde{\tau}_\nu} \right\} r^2 q_\nu \\ &= \left\{ -\left(\frac{3f_\nu - 1}{\chi_\nu r} - \frac{\mathrm{d} f_\nu}{\mathrm{d}\tau_\nu} \right) B_\nu + f_\nu \frac{\mathrm{d}B_\nu}{\mathrm{d}\tau_\nu} \right\} r^2 \end{aligned} \tag{5.21}$$

making use of the definition of the sphericality factor q_ν (see Eq. (3.33))

$$\frac{\mathrm{d}(r^2 q_\nu)}{\mathrm{d}r} := r^2 q_\nu \frac{3f_\nu - 1}{r f_\nu}.$$

Note that the last line in Eq. (5.21) contains only derivatives in τ_ν, not $\tilde{\tau}_\nu$, because q_ν cancels in $\mathrm{d}\tilde{\tau}_\nu = -q_\nu \chi_\nu \, \mathrm{d}r$.

Next we consider the integration constant C_ν in Eq. (5.18). This constant can be obtained by considering that in the outer part of the atmosphere

$$j_\nu(\tilde{\tau}_0) = \left.\frac{H_\nu}{J_\nu}\right|_{\tilde{\tau}_0} \approx 2 \qquad \text{for} \quad \tilde{\tau}_0(\nu) \ll 1 \tag{5.22}$$

holds and therefore it follows that

$$\tilde{J}_\nu(\tilde{\tau}_0(\nu)) = j_\nu(\tilde{\tau}_0) \left.\frac{\mathrm{d}q_\nu f_\nu \tilde{J}_\nu}{\mathrm{d}\tilde{\tau}_\nu}\right|_{\tilde{\tau}_0}. \tag{5.23}$$

Inserting the result of Eq. (5.18) into Eq. (5.23) gives

$$\begin{aligned}\tilde{B}_\nu(\tilde{\tau}_0(\nu)) + \frac{C_\nu}{(q_\nu f_\nu)_{\tilde{\tau}_0}} e^{-\sqrt{\left\langle\frac{1-\beta_\nu}{q_\nu^2 f_\nu}\right\rangle}\tilde{\tau}_0(\nu)} &= \\ = j_\nu(\tilde{\tau}_0) \left.\frac{\mathrm{d}\left(q_\nu f_\nu \tilde{B}_\nu\right)}{\mathrm{d}\tilde{\tau}_\nu}\right|_{\tilde{\tau}_0} - j_\nu(\tilde{\tau}_0) C_\nu \sqrt{\left\langle\frac{1-\beta_\nu}{q_\nu^2 f_\nu}\right\rangle} e^{-\sqrt{\left\langle\frac{1-\beta_\nu}{q_\nu^2 f_\nu}\right\rangle}\tilde{\tau}_0(\nu)} &\end{aligned} \tag{5.24}$$

and hence the expression for C_ν

$$C_\nu = \frac{-\tilde{B}_\nu(\tilde{\tau}_0(\nu)) + j_\nu(\tilde{\tau}_0(\nu)) \left.\frac{\mathrm{d}\left(q_\nu f_\nu \tilde{B}_\nu\right)}{\mathrm{d}\tilde{\tau}_\nu}\right|_{\tilde{\tau}_0}}{\left(\frac{1}{q_\nu f_\nu}\right)_{\tilde{\tau}_0} + j_\nu(\tilde{\tau}_0)\sqrt{\left\langle\frac{1-\beta_\nu}{q_\nu^2 f_\nu}\right\rangle}} e^{\sqrt{\left\langle\frac{1-\beta_\nu}{q_\nu^2 f_\nu}\right\rangle}\tilde{\tau}_0(\nu)} \qquad \text{for} \quad \tilde{\tau}_0 \ll 1. \tag{5.25}$$

In practice, $\tilde{\tau}_0$ has been chosen so that, at the corresponding depth point, the radiation field is not entirely decoupled from matter (e.g., $\tilde{\tau}_0 \approx 0.1$). This is necessary so that the temperature in $B_\nu(T(\tilde{\tau}_0))$ at this depth point is still meaningful to characterize the radiation field. Using the result of Eq. (5.21), C_ν can be expressed as

$$C_\nu = \frac{r(\tilde{\tau}_0)^2 \left\{ j_\nu \left(\frac{\mathrm{d}f_\nu}{\mathrm{d}\tau_\nu} - \frac{3f_\nu - 1}{\chi_\nu r}\right) - 1\right\}_{\tilde{\tau}_0} B_\nu(\tilde{\tau}_0) + f_\nu(\tilde{\tau}_0) \left.\frac{\mathrm{d}B_\nu}{\mathrm{d}\tau}\right|_{\tilde{\tau}_0}}{\left(\frac{1}{q_\nu f_\nu}\right)_{\tilde{\tau}_0} + j_\nu(\tilde{\tau}_0)\sqrt{\left\langle\frac{1-\beta_\nu}{q_\nu^2 f_\nu}\right\rangle}} e^{\sqrt{\left\langle\frac{1-\beta_\nu}{q_\nu^2 f_\nu}\right\rangle}\tilde{\tau}_0(\nu)} \tag{5.26}$$

As a further approximation we adopt an expansion in $1/\tau$ for f_ν assuming that $f_\nu \to \frac{1}{3}$ for $\tau_\nu \to \infty$ to avoid mixing terms of $\frac{\mathrm{d}f_\nu}{\mathrm{d}\tau}$ and f_ν in Eq. (5.20):

$$f_\nu(1/\tau_\nu) \approx \tfrac{1}{3} + \frac{\mathrm{d}f_\nu}{\mathrm{d}(1/\tau_\nu)}(1/\tau_\nu) \qquad \Rightarrow \qquad f_\nu(\tau_\nu) \approx \tfrac{1}{3} - \frac{\mathrm{d}f_\nu}{\mathrm{d}\tau_\nu}\tau_\nu \tag{5.27}$$

Introducing this in Eq. (5.20) together with Eq. (5.21) gives a new expression for the flux at the inner boundary that has the form of the original diffusion flux plus additional correction terms that vanish for large optical depths and an isotropic radiation field:

$$H_\nu^0 = \frac{1}{3}\frac{\mathrm{d}B_\nu}{\mathrm{d}\tau_\nu} + \frac{\mathrm{d}f_\nu}{\mathrm{d}\tau_\nu}\left\{\left(\frac{3\tau_\nu}{\chi_\nu R} + 1\right)B_\nu - \tau_\nu\frac{\mathrm{d}B_\nu}{\mathrm{d}\tau_\nu}\right\} - \frac{C_\nu}{R^2}\sqrt{\left\langle\frac{1-\beta_\nu}{q_\nu^2 f_\nu}\right\rangle} e^{-\sqrt{\left\langle\frac{1-\beta_\nu}{q_\nu^2 f_\nu}\right\rangle}\tilde{\tau}_\nu}. \tag{5.28}$$

In the radiative transfer code, a slightly different form was used by solving Eq. (5.27) for $\frac{\mathrm{d}f}{\mathrm{d}\tau}$ since the gradient of the Eddington factor is numerically less accurate than f_ν itself

$$\frac{\mathrm{d}f_\nu}{\mathrm{d}\tau_\nu} \approx \left(\tfrac{1}{3} - f_\nu\right)\tau_\nu^{-1}. \tag{5.29}$$

This leads to the alternative form of

$$H_\nu^0 = f_\nu \frac{\mathrm{d}B_\nu}{\mathrm{d}\tau_\nu} + \left(\frac{1}{3} - f_\nu\right)\left(\frac{1}{\tau_\nu} + \frac{3}{\chi_\nu R}\right)B_\nu - \frac{C_\nu}{R^2}\sqrt{\left\langle\frac{1-\beta_\nu}{q_\nu^2 f_\nu}\right\rangle}\, e^{-\sqrt{\left\langle\frac{1-\beta_\nu}{q_\nu^2 f_\nu}\right\rangle}\tilde{\tau}_\nu}. \tag{5.30}$$

From Eq. (5.18) and Eq. (5.30), the final expression for the intensity at the core is then

$$\begin{aligned} I_\nu^+ = {} & B_\nu + \frac{C_\nu}{q_\nu f_\nu r^2}\, e^{-\sqrt{\left\langle\frac{1-\beta_\nu}{q_\nu^2 f_\nu}\right\rangle}\tilde{\tau}_\nu} + \\ & + 3\mu\left\{ f_\nu \frac{\mathrm{d}B_\nu}{\mathrm{d}\tau_\nu} + \left(\frac{1}{3} - f_\nu\right)\left(\frac{1}{\tau_\nu} + \frac{3}{\chi_\nu R}\right)B_\nu - \frac{C_\nu}{R^2}\sqrt{\left\langle\frac{1-\beta_\nu}{q_\nu^2 f_\nu}\right\rangle}\, e^{-\sqrt{\left\langle\frac{1-\beta_\nu}{q_\nu^2 f_\nu}\right\rangle}\tilde{\tau}_\nu}\right\}. \end{aligned} \tag{5.31}$$

5.2.4 Discussion and interpretation

The isotropic terms in Eq. (5.31) represent the standard diffusion approximation B_ν plus a correction term. Because in the enumerator of C_ν in Eq. (5.25), the B_ν-term generally dominates over the derivative term, it follows that $C_\nu \leq 0$. Therefore, J_ν^0 derived in this way will be smaller than for the standard formulation if the optical depths are low enough for the additional term to take effect. This complies with the aim of diminishing the input of radiation at the inner boundary at wavelength regions where the opacities are too low to maintain thermal conditions. For large optical depths, the exponential function brings the second term to zero and retains the standard B_ν-term.

The flux part of Eq. (5.31) also approaches the form in Eq. (5.4) because $f_\nu \to \frac{1}{3}$ for large τ; in this case, the second and third terms will also vanish. Note that due to a negative sign of C_ν, the flux term may actually *increase* compared to the original version. Physically this can be understood by recalling that a lower local radiation field J_ν at the inner boundary has to increase the nonlocal part (i.e., the flux). In the models of early epochs considered here, the first term dominates the boundary condition. Thus, the form Eq. (5.31) overall reduces the flux emerging at the outer boundary. For later epochs where the local contribution to the radiation field decreases, the situation may become different. In that case, however, the main contribution to the radiation field will be generated from the energy deposition of γ-rays anyway and the radiation from the boundary becomes insignificant. In this work, the late times have not been considered in more detail; however, this expression provides an analytic approach for further investigations in that direction.

An alternative for the zeroth term

An alternative to the analytic expression Eq. (5.18) for the isotropic term I_ν^0 can be used noting that one can directly employ J_ν at the inner boundary that is obtained from an iteration cycle between the ray-by-ray solution and the moment equations. (This iteration is done anyway to determine the Thomson emissivity.)

In the solution of the moment equations, one can solve for this term implicitly by writing the boundary equation as

$$\frac{\mathrm{d}(f_\nu q_\nu \tilde{J}_\nu)}{\mathrm{d}\tilde{\tau}_\nu} = \tfrac{1}{2}\tilde{J}_\nu + H_\nu^0 R^2 - h_\nu \tilde{J}_\nu \tag{5.32}$$

$$\Rightarrow \quad \frac{\mathrm{d}(f_\nu q_\nu \tilde{J}_\nu)}{\mathrm{d}\tilde{\tau}_\nu} - \left(\tfrac{1}{2} - h_\nu\right)\tilde{J}_\nu = H_\nu^0 R^2 \qquad \text{for} \quad \tau_\nu = \tau_\nu^{\max}. \tag{5.33}$$

An equivalent expression for the ray-by-ray solution is not as straightforward and leads to inconsistent results for J_ν in the iteration. Therefore, in the ray-by-ray solution, J_ν resulting from the moment equation is used explicitly in the boundary condition and is iterated.

Effectively, this means that the inner boundary is less strictly constrained, which bears the danger of numerical instability. To ensure that the boundary condition is still well behaved, this modification has been studied on simple test models before applying it to the radiative transfer code where coupling of too many quantities makes the study significantly more difficult.

A set of different situations is shown in Figure 5.6. The basic parameters of this toy model that are not changed are the Thomson-opacity $\chi_{\mathrm{Th}} = 1$ and the background opacity (continuum) $\chi_{\mathrm{c}} = 10^{-3}$ with a corresponding source function $S_{\mathrm{c}} = 1$. The line has a source function of $S_{\mathrm{l}} = 5$. The zeroth term of the traditional boundary condition is set $I^0 = 10$ for the first three models and $I^0 = 2$ for the last. H_0 is set equal to 0 in all cases. The radiation field is obtained by an iteration of a ray-by-ray solution with a solution of the moment equations in spherical symmetry. A Feautrier scheme similar to the one in the radiative transfer code is used. Generally, in the main code, convergence is obtained within less than 15 iterations — depending on the physical conditions and, in particular, depending on the relevance of Thomson-scattering. (For comparison, the iteration for Thomson-scattering alone usually converges within < 5 iterations.) All plots show the comparison of J as a function of radius obtained from the solution of the moment equations. The result from the traditional choice of setting $I^0 = \mathrm{const}$ (in practice $= B_\nu$) is shown with "+" symbols in red. The result using $I^0 = J$ is shown in blue with diamonds. The black dash-dotted line is the true source function (line and background). The upper left panel in Figure 5.6 shows the situation for an optically thick line ($\tau = 5$). Here the modification only influences the radiation field in the inner region as the emergent radiation is entirely separated from the inner region by the line. In the inner region, J is significantly larger than in the old treatment even though the physical conditions cannot cause this increase in intensity (because of the low true opacity). However, in this situation the significant shortcoming of

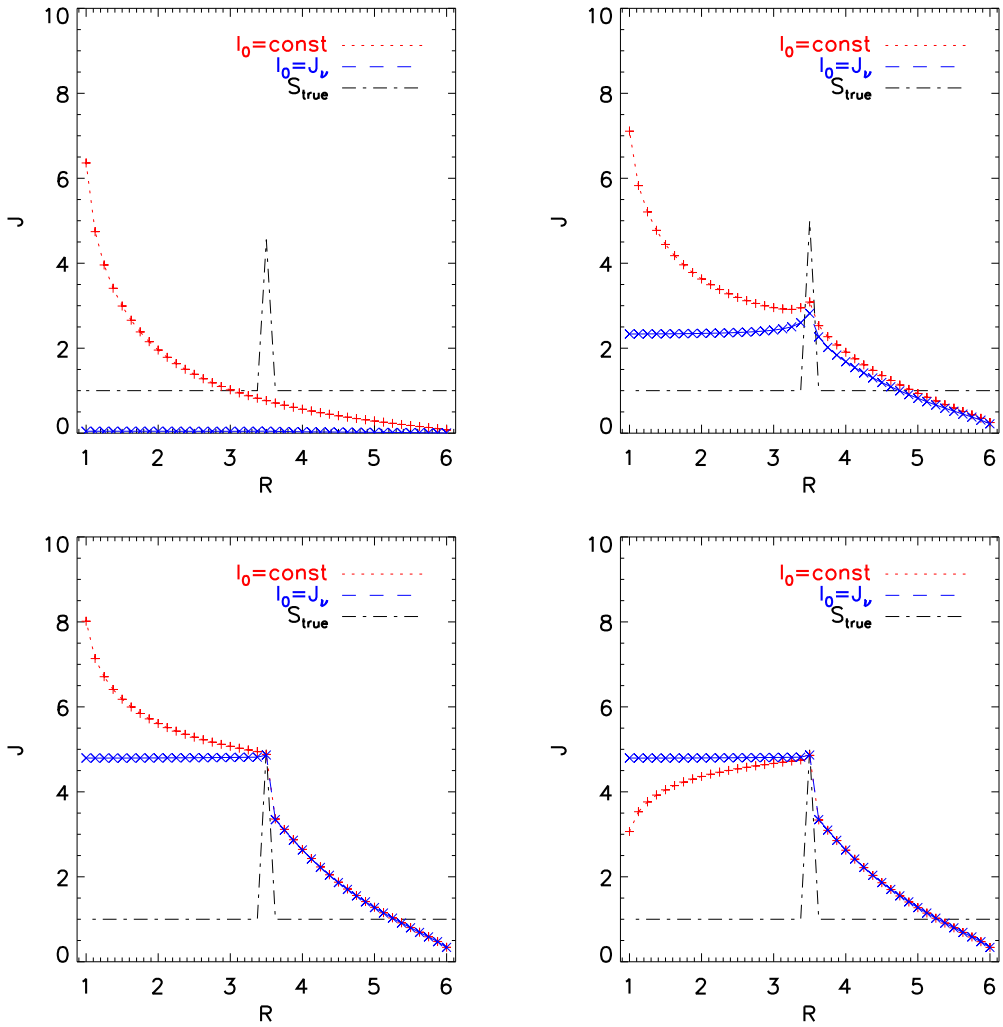

Figure 5.6: Toy model for the new treatment of the zeroth term of I^+ at the inner boundary. The line with "+" symbols shows the traditional setting I^0 = const(= B_ν), the line with diamonds shows the new treatment (see text). The upper left panel shows the case of an optically thin model (line and continuum) where (τ_1 = 0.001). The upper right panel shows an intermediate case (τ_1 = 0.2). The lower left shows the optically thick case (τ_1 = 5). The lower right panel shows a situation where the method would overestimate J in the inner region. (Here S_1 is chosen to be larger than I^0 at the inner boundary.) These are cases where the application of an iterative determination of I^0 fails and is therefore fixed to a value of a previous frequency point (see text).

this method becomes apparent: in reality, J_ν should drop to $\frac{1}{2}S_1$ toward the inner boundary because the absence of emission toward the inner region means that $I^+ \equiv 0$. The model, however, effectively sets $I^+ = I^-$. Unfortunately, this situation occurs quite frequently in SN Ia: at each frequency point where the opacity at the boundary is low but increases outward due to a line being shifted into that frequency by the large velocity gradient. If this is not prevented by an additional correction, the artificial emission builds up in the iteration between the moment equations and the formal ray-by-ray solution. Eventually, it also affects the rate equations and the temperature in the inner region.

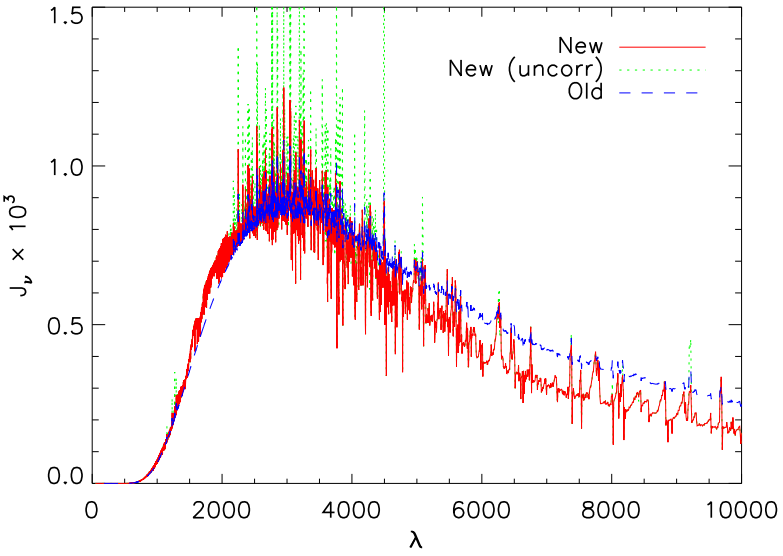

Figure 5.7: The radiation field J_ν at the inner boundary for different treatments of the intensity term in I^+. The dotted green line shows the radiation field for the uncorrected iterative method, which produces large artificial peaks at wavelength points where a line is present further outside within a small τ-interval. The solid red line represents the new method including the correction for those wavelength points. The dashed blue line is calculated with the traditional treatment of the inner boundary. One can see clearly that the new method significantly reduces the radiation field in the red part of the spectrum. For better comparison, all three models are shown after a few iterations before the first temperature update.

As a first step to correct this behavior, criteria have to be established to determine when a correction should be applied. No correction is needed if the continuum is optically thick or if the local opacity at the first two radius points is large (e.g., strong continuum or if a line is present). Another criterion has to include a comparison of the local opacity to an average opacity over a reference ΔR-step. If the average opacity is higher than the local opacity, a line is likely to be present further out. The reference ΔR is chosen according to a step $\Delta\tau_c \geq 3$ for pure continuum opacity (true and Thomson). The exact conditions for

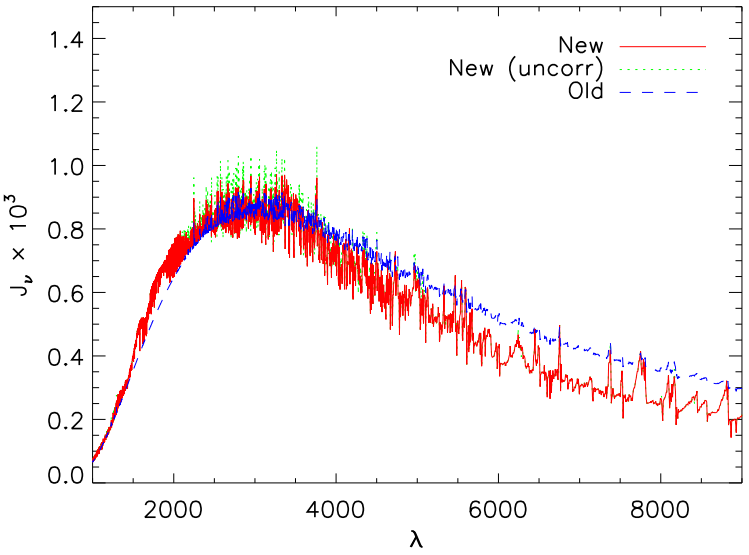

Figure 5.8: As in Figure 5.7, the radiation field J_ν at the inner boundary for different treatments of the intensity term in I^+. In the models shown here, however, the modified Feautrier scheme (see Section 5.3) is applied. In general, this causes the artificial peaks to be smaller.

the correction used in the current implementation are listed in Table 5.1.

Secondly, a suitable correction has to be used for the respective frequency points. We found that a suitable approach was to use a fixed value $I^0_\nu = J_{\nu'}$ with $J_{\nu'}$ being J_ν of the last (redder) uncorrected frequency point. To prevent excessively large values for I^0_ν in frequency regions where many subsequent points have to be corrected, an upper cut-off at B_ν is applied.

Figure 5.7 shows the radiation field J_ν at the inner-most grid point for the case where the new method is used with and without correction (red solid line and green dotted line, respectively). The third model shown in Figure 5.7 uses the standard boundary condition (blue dashed line). One can see that the uncorrected new boundary treatment produces

Continuum:	$\tau_c(R_{\text{ref}})$	$\leq$	10
Local χ:	$\chi(1)(R(2) - R(1))$	$\leq$	6
Comparison line-continuum:	$\tau_{c+l}(R_{\text{ref2}})/\tau_c(R_{\text{ref2}})$	$\geq$	3
Comparison local to average χ:	$\tau_{c+l}/(\chi(1)(R_{\text{ref}} - R(1)))$	$>$	1

Table 5.1: Conditions for the correction of enhanced J_ν at the inner boundary. The reference radius R_{ref} is set to the radius of $\tau_{\text{Ross}} \approx 2/3$. R_{ref2} refers to the radius where $\tau_{c+l} \geq 3$. All τ values are derived radially from the inside outward.

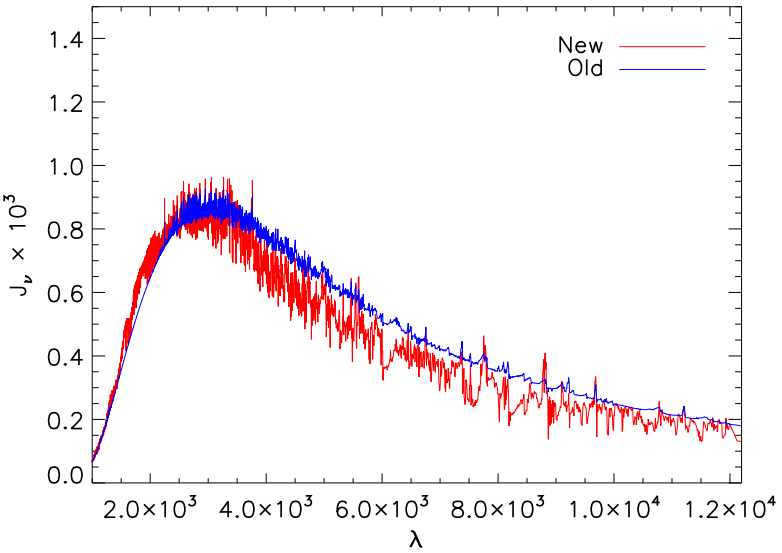

Figure 5.9: As in Figure 5.8 the radiation field J_ν at the inner boundary, but with the full new I^+ treatment (intensity and flux-term) compared to a model using the standard diffusion approximation. Although the modified flux term increases J_ν in the red part, overall it results in a decrease of J_ν compared to the old treatment.

large artificial emission peaks. These peaks occur at wavelengths where a line is present further out within a small τ-interval. The peaks are actually increased by an additional effect caused by the treatment of the line emissions in the Feautrier scheme (discussed in the next section). If the modified treatment proposed there is also applied, the peaks, which are still visible in the corrected model become less severe. (This also applies to the uncorrected model; thus, the correction of the boundary condition has less significance.) Figure 5.8 shows the same models as in Figure 5.7, but calculated with the modified Feautrier coefficients of Section 5.3.

Figure 5.9 shows a model derived with the application of the full new I^+ in comparison to a model using the standard diffusion approximation. Note that the flux-term Eq. (5.30) increases J_ν compared to Figure 5.8; however, the overall effect is still a decrease of radiation in the red wavelength-bands.

Additionally, Figure 5.7 and Figure 5.8 show clearly that the characteristic of the radiation field is far from Planckian, which causes the standard diffusion approximation to be unsuitable. It also can be seen that the new method produces less radiation in the red and infrared region compared to the old boundary treatment.

Figure 5.10 shows a comparison of two test models with the old and the new treatment of the boundary. One can see that in the red wavelength region, the radiation field in the model using the new method is slightly diminished compared to the model using the standard

procedure. A direct comparison, however, is difficult because the treatment has significant influence on the occupation numbers, the ionization, and the temperature structure, as can be seen especially in UV part of the spectrum.

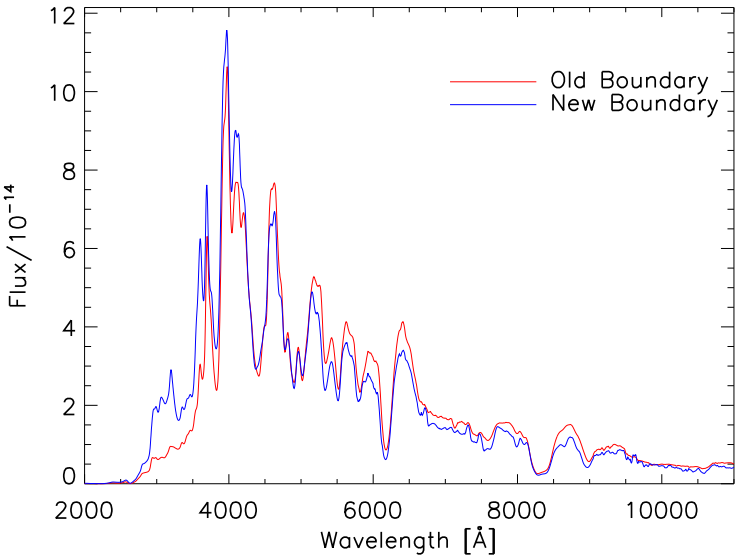

Figure 5.10: Comparison of two test models using the old and the new treatments of the inner boundary. One can see that the flux in the red wavelengths is diminished in the model using the new boundary treatment. Note that the two models are not strictly comparable because the occupation numbers, ionization, and temperature structure adjust differently.

5.3 Self-absorption of lines in the Feautrier scheme

As mentioned in Section 4.1.1, the Feautrier scheme for the solution of the radiative transfer leads to difficulties if used for physical conditions where the opacities and emissivities have strong variations at adjacent depth points.

In the Feautrier scheme, the total source functions are evaluated on the respective radial grid points. This effectively sets the entire emission of an interval on that grid-point, while the transport coefficients contain the absorption over an interval between grid points. Consider the situation where one grid point with low opacity χ_i (which makes the source function S_i at this point meaningless). We further assume that the adjacent point $i-1$ has a large opacity χ_{i-1} and source function S_{i-1} (e.g., by the presence of a strong line). In reality the emission from a line occurs at a distance in r where the line becomes optically thick $\tau > 1$, which means that the low opacity point would "see" the source function of the line at the point where $\Delta\tau \gtrsim 1$ is reached. The numerical solution, however, systematically

underestimates the radiation being transported from the point $i-1$ into the low opacity region i. This effect can be understood as follows: recall the general structure of the equation system solved (cf. Section 4.1.1):

$$a_i u_{i-1} + b_i u_i + c_i u_{i+1} = q_i S_i = k_i \tag{5.34}$$

where the coefficients are such that

$$b_i = q_i - a_i - c_i. \tag{5.35}$$

The coefficients a_i and c_i relate to the transport over the interval $[i, i-1]$ and $[i, i+1]$ respectively, while b_i and q_i describe the local grid point i. Thus the former are functions of the "remote" optical depth interval $\Delta\tau_i^{\pm} = \bar{\chi}_{i,i\pm1}\Delta z_{i,i\pm1}$, while q_i is a function of the "local" optical depth interval $\Delta\tau_i = \chi_i \Delta z_{i+1,i-1}$:

$$a_i = \left(\Delta\tau_i^-\right)^{-1}, \qquad c_i = \left(\Delta\tau_i^+\right)^{-1}, \qquad q_i = \Delta\tau_i, \quad \text{and} \quad b_i = q_i - a_i - c_i. \tag{5.36}$$

Let us now consider the extreme case of a single line in a low opacity environment by setting $S_{i-1} \neq 0$, $\chi_{i-1} \neq 0$, $S_{j\leq i} \to 0$, and $\chi_{j\leq i} \to 0$. For the coefficients in Eq. (5.34) this means that

$$\begin{aligned} \Delta\tau_i^- \gg 1 \quad &\Rightarrow \quad a_i \to 0 \\ \Delta\tau_i^- \ll 1 \quad &\Rightarrow \quad c_i \gg 1 \\ \Delta\tau_i \to 0 \quad &\Rightarrow \quad q_i \to 0 \\ &\Rightarrow \quad b_i = -c_i. \end{aligned} \tag{5.37}$$

Therefore, the equation for u_i is

$$u_i = -\frac{c_i}{b_i} u_{i+1} = u_{i+1}. \tag{5.38}$$

All points $j > i-1$ decouple entirely from the point $i-1$ and accordingly, u_j is determined by whatever else is emitted. Figure 5.11 shows this example; from the left, an incident "core" intensity is assumed, whereas the right boundary has no incoming radiation.

For this example, two models have been derived: one in high resolution where the numerical solution should be close to the exact one because the run of opacities is smooth enough[1], and a second low-resolution model that corresponds more to the conditions present in the radiative transfer solver used for the sampling method (cf. Section 4.1.1). The high-resolution model assumes a Gaussian profile for the line, which is represented by a single grid point in the low-resolution model. The opacity at that point is chosen such that the optical depth through the radial interaction zone is the same as for the highly resolved model. The opacity distribution of both models on the ray are shown in the lower

[1] The condition for the standard Feautrier solution to be accurate is actually that $\Delta\tau \ll 1$.

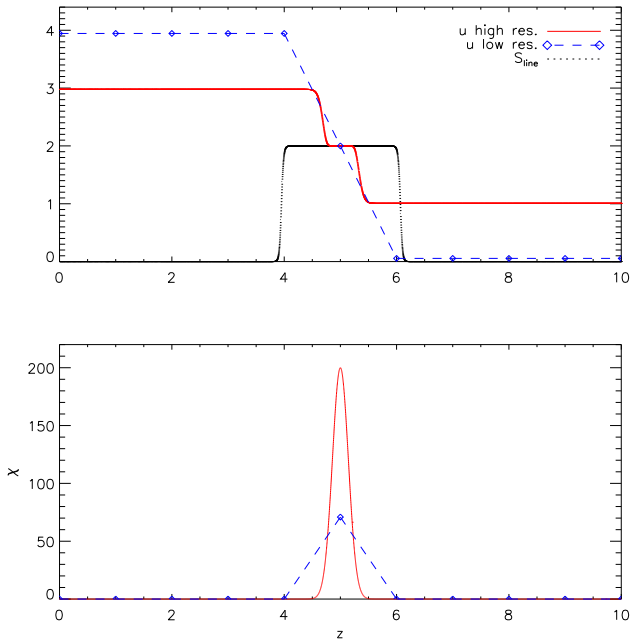

Figure 5.11: Toy model to illustrate the problem of self absorption in the standard Feautrier scheme for a single *p*-ray (see text). The lower panel shows the opacity distribution for this model. The opacities of the models are chosen such that the same total optical depth over the entire radial interaction zone is reached. The upper panel shows the u function derived from the standard Feautrier solution using an incident intensity $I^+ = 4$ from the left side and $I^- = 0$ on the right side. The black lines denote the run of the S_{line}.

panel. The upper panel shows the u-function derived from the Feautrier algorithm described in Section 4.1.1 and the adopted source function $S_{\text{line}} = 2$ in the line for both models (black dashed and dotted lines). For the left side, an incident intensity $I^+ = 4$ was assumed, while the right side had $I^- = 0$. The red line denotes the solution of the highly resolved model and follows what one would expect for that case theoretically: within the optically thick line u approaches S_{line}, while on the right side it reaches $\frac{1}{2}S_{\text{line}}$ because $u = \frac{1}{2}(I^+ + I^-) = \frac{1}{2}(S_{\text{line}}\Delta\tau + 0)$. Accordingly, on the side where an incident I^+ is present, the result is half way between I^+ and S_{line} ($u = \frac{1}{2}(I^+ + S_{\text{line}}\Delta\tau)$). The blue line with the bullet points shows the solution for the model on the coarse grid. (The values are only derived on the grid points as indicated; the connecting lines are just for better visibility.) As can be clearly seen, on both sides of the line the solution significantly underestimates the radiation field compared to the exact solution. Effectively, the line emission is not represented in the transport at all because the solutions outside the line are only coupled to the boundary points. Of course an extreme case like the one presented here will rarely occur in real models because the continuous opacity will usually smooth out the profiles and also prevent zero opacity at some points. However, in particular for supernova where the line opacity dominates the total opacity over almost the entire spectrum, cases similar to this

are more likely to occur. Here the standard solver will systematically underestimate the radiation field in the (radial) gaps between lines and toward the outer boundary, leading to a loss of total radiative energy that is not represented in the rate equations. Note, that this only affects the transport in our method I for the radiative transport. The detailed solution is derived on a micro-grid that resolves the line profiles in small $\Delta\tau$-steps and therefore does *not* suffer from this problem.

5.3.1 New Feautrier coefficients

The correction method should not affect the transport of radiation through a grid point. Additionally, the solution has to remain unchanged for a smooth, continuous run of opacities because these cases are correctly represented by the standard scheme. Additionally, at high grid resolution, both the new and the old scheme should agree on the same solution because in the limit of infinitely small intervals the standard method approaches the exact solution. We found that the first constraint strictly excludes any modification of the transport terms a_i and c_i. Therefore, the only remaining option is to adjust the source terms and the b-coefficient. The concept is to correct the intensity derived at a particular grid point by adding an additional contribution from the emission of adjacent grid points. The amount of correction has to be a function of the local $\Delta\tau_i$ and the respective remote $\Delta\tau_i^{\pm}$. Thus, the following approach for a new coefficient b_i and the right-hand side k_i of Eq. (5.34) has been made:

$$k_i = q_i S_i + \xi_i^+ S_{i+1}^* + \xi_i^- S_{i-1}^* \tag{5.39}$$

$$b_i = q_i - a_i - c_i + \xi_i^+ + \xi_i^- \tag{5.40}$$

with correction functions $\xi_i^{\pm} = \xi_i^{\pm}(\Delta\tau_i, \Delta\tau_i^{\pm})$ to be determined. The source functions S^* are taken to be the (total) line source functions $\eta_{\rm line}/\chi_{\rm line}$ at the respective point to ensure that the correction does not affect the continuum transport. To obtain the original coefficients of Eq. (4.17) in Section 4.1.1, the system Eq. (5.36) has to be divided by q_i. Thus, coefficients A_i and C_i in Eq. (4.24) remain unchanged, while B_i and the right-hand side K_i acquire additional terms:

$$A_i = -\left(\tfrac{1}{2}\chi_i\,(z_{i+1} - z_{i-1})\,\bar{\chi}_{i,i-1}\,(z_i - z_{i-1})\right)^{-1} \tag{5.41}$$

$$C_i = -\left(\tfrac{1}{2}\chi_i\,(z_{i+1} - z_{i-1})\,\bar{\chi}_{i+1,i}\,(z_{i+1} - z_i)\right)^{-1} \tag{5.42}$$

$$B_i = 1 - A_i - C_i + \left(\tfrac{1}{2}\chi_i\,(z_{i+1} - z_{i-1})\right)^{-1}\left(\xi_i^+ + \xi_i^-\right) \tag{5.43}$$

$$K_i = S_i + \left(\tfrac{1}{2}\chi_i\,(z_{i+1} - z_{i-1})\right)^{-1}\left(\xi_i^+ S_{i+1}^* + \xi_i^- S_{i-1}^*\right). \tag{5.44}$$

The coefficients at the boundary conditions have to be adjusted accordingly using the corresponding adjacent interval.

Moment equations

In the solution scheme for the moment equations Eq. (4.49) and Eq. (4.50), a similar method has to be applied. For consistency with the ray-by-ray solution, the correction terms $\xi^{\pm} u_i$ are integrated over $\mu\,\mathrm{d}\mu$ introducing a factor $h'_i = \int u_i(\mu)\mu\,\mathrm{d}\mu / J_i$ analogous to h in Eq. (4.55). Here, however, the numerical integration for h'_i has to be performed using integration weights on the respective grid point instead of the weights on the intermesh points used for the flux integration. Eventually, one derives the new coefficients for the system Eq. (4.49) to be

$$\mathcal{A}_i = -\frac{f_{i+1}q_{i+1}}{\frac{1}{2}\chi_i(r_{i+1}-r_{i-1})\overline{q\chi}_{i+1,i}(r_{i+1}-r_i)} \tag{5.45}$$

$$C_i = -\frac{f_{i-1}q_{i-1}}{\frac{1}{2}\chi_i(r_{i+1}-r_{i-1})\overline{q\chi}_{i,i-1}(r_i-r_{i-1})} \tag{5.46}$$

$$\mathcal{B}_i = \frac{f_i q_i}{\frac{1}{2}\chi_i(r_{i+1}-r_{i-1})}\left(\frac{1}{\overline{q\chi}_{i+1,i}(r_{i+1}-r_i)} - \frac{1}{\overline{q\chi}_{i,i-1}(r_i-r_{i-1})}\right) + \tag{5.47}$$

$$+ (1-\beta) + \left(\tfrac{1}{2}\chi_i(r_{i+1}-r_{i-1})\right)^{-1}\left(\xi_i^+ + \xi_i^-\right) h'_i r_i^2 \tag{5.48}$$

$$\mathcal{K}_i = \tilde{S}^{\dagger} + \tfrac{1}{2}\left(\xi_i^+ S^*_{i+1} + \xi_i^- S^*_{i-1}\right)\left(\tfrac{1}{2}\chi_i(r_{i+1}-r_{i-1})\right)^{-1} r_i^2. \tag{5.49}$$

The first order boundary conditions for the system remain unchanged because no source functions enter here.

Correction functions $\xi^{\pm}$

Now that we know where the correction is to be applied, suitable functions $\xi^{\pm}$ that depend on the opacities in the "local" and "remote" intervals have to be found. Correction is only needed for the case where the respective remote and the local τ-interval are low. In this case, if the line source function S^* of the adjacent point is large, the emission of the local point has to be enhanced. In addition, the correction function has to drop to zero for large "remote" $\Delta\tau$ faster than the $1/\Delta\tau$-terms in the transport coefficients.

A possible choice for the ξ-functions that has been found to provide the desired properties is

$$\begin{aligned} \xi_i^- &= \left(1 - e^{-\bar{\chi}^-_{\mathrm{line}}(z_i - z_{i-1})}\right)^2 e^{-\Delta\tau_i} \\ \xi_i^+ &= \left(1 - e^{-\bar{\chi}^+_{\mathrm{line}}(z_{i+1} - z_i)}\right)^2 e^{-\Delta\tau_i} \end{aligned} \tag{5.50}$$

with the averaged opacities

$$\bar{\chi}^{\pm}_{\mathrm{line}} = \tfrac{1}{2}\left(\chi_i^{\mathrm{line}} + \chi_{i\pm1}^{\mathrm{line}}\right) \tag{5.51}$$

and $\Delta\tau_i = \chi_i \frac{1}{2}(z_{i+1} - z_{i-1})$ as before. The quadratic term in Eq. (5.50) vanishes if the line opacity in the interval is small, indicating the absence of a significant line at the next grid

point. The power of 2 is necessary to ensure that this term drops to zero faster than the corresponding transport coefficient $\sim 1/\Delta\tau_i^{\pm}$. If a line or strong continuum is present at the current grid point, the second term becomes zero avoiding additional emission in a center of the line.

5.3.2 Simple test cases and application of the new Feautrier coefficients

To test the properties of the new coefficients, a variety of different situations have been simulated before the application in the actual transport code. Figure 5.12 shows the same models as in Figure 5.11, but with the correction applied. As can be seen here, the solution on the coarse grid corresponds much better with the high-resolution model, which remained unchanged as desired.

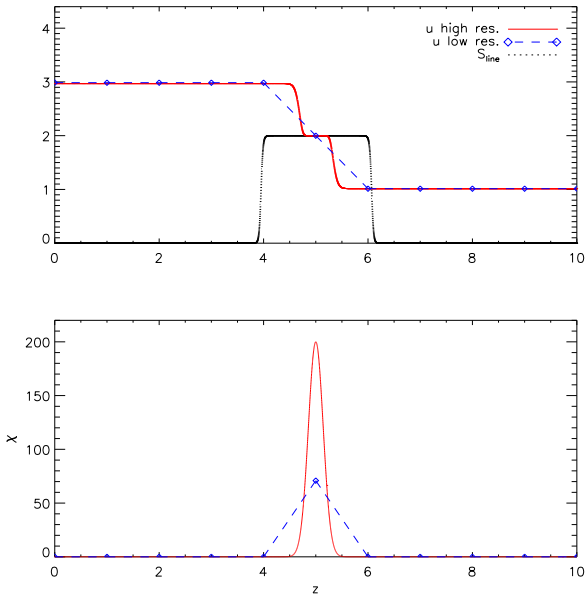

Figure 5.12: Single-ray models corresponding to Figure 5.11 with the ξ-correction applied. While the high-resolution model remains unaffected, the model on the coarse grid now reproduces the analytically expected result much better.

To estimate the quality of the correction in realistic models, situations with continuum opacity (in particular including Thomson-scattering) also had to be investigated. The toy model had to be extended to a spherically symmetric model for two main reasons. First, the determination of the Thomson-emissivity requires the knowledge of the mean intensity J. Second, we wanted to see the effect on the angle-integrated quantities.

Figure 5.13 shows a selection of situations that have been simulated using this extended version. All low-resolution models use a uniformly spaced radial grid with 41 grid points

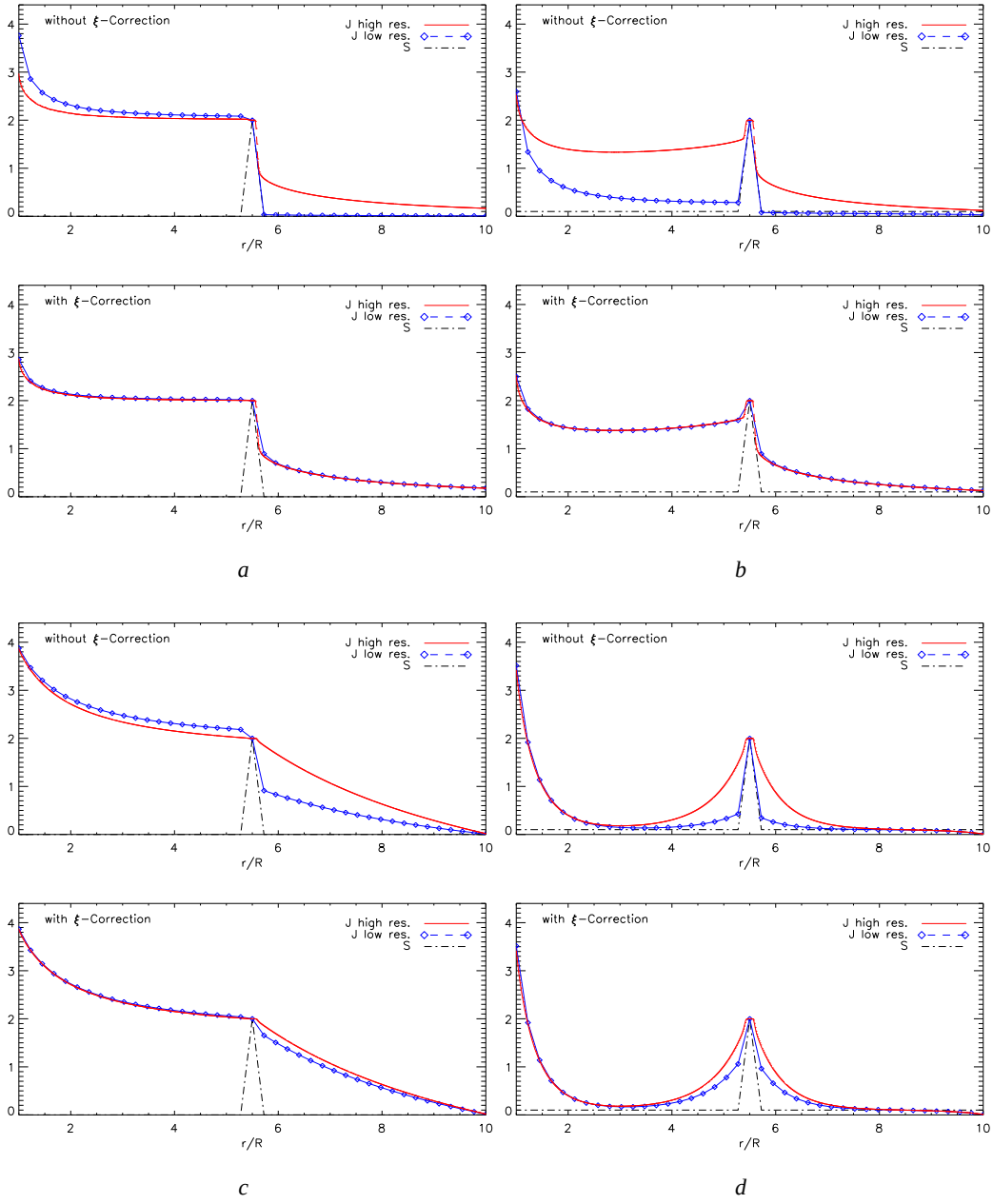

Figure 5.13: Spherically symmetric test models for the corrected Feautrier coefficients. In all models the incident intensity at the core was set to $I^+ = 4$, while at the outer boundary no incoming radiation was assumed. In each figure, the upper panel shows the uncorrected models and the lower panel shows the same setup with the correction applied. *a*: Optically thick line ($\tau_{\text{line}} = 50$) without any background opacity and source function. *b*: Same setup for the line as in *a*, but with a low background opacity and source function. *c* and *d*: Same setup as in *a* and *b*, respectively, but including Thomson opacity and emissivity.

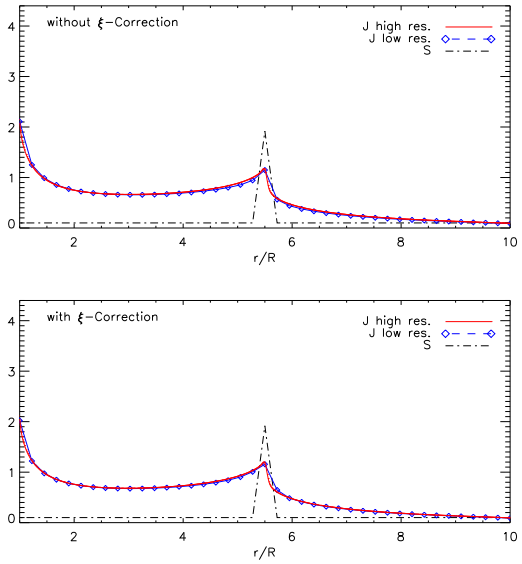

Figure 5.14: Same situation as in Figure 5.13*b*, but for an optically thin line ($\tau_{\text{line}} = 0.5$). Here the old and new method produce very similar results.

and 5 core rays. The high-resolution grid is set up by dividing each interval into 14 sub-intervals and uses 20 core rays. The source function of the line was again set to $S_{\text{line}} = 2$ and the incident intensity at the core to $I^+ = 4$. The opacity of the line has been determined such that a given radial optical depth τ_{line} was reached. In all figures, the upper panel shows the derived mean intensity J without correction and the lower panel shows the respective models with the correction applied. All values of J have been obtained by iterating the ray-by-ray solution with the solution of the moment equation. (The final J from the different methods was in agreement on the level of a few percent, depending on the model.) The setup in Figure 5.13*a* is similar to the single-ray models, an optically thick line ($\tau_{\text{line}} = 50$) without any other opacities or emissivities. Again, in the upper panel, it can be seen that J in the low-resolution model directly couples to the boundary values resulting in excessively large values inside the shell that contains the line and values that are too low in the outer region. In the lower panel, the corrected version of that model is shown. Here the quality of the correction is the same as in the single-ray case. Figure 5.13*b* shows the same setup, but with a low constant background source function and opacity ($S_{\text{bg}} = 0.1$, $\chi_{\text{bg}} = 0.1$). Compared to Figure 5.13*a* this model shows that in the presence of opacity on other grid points, the uncorrected solution outside the line strongly couples to the local source function. The lower two sets in Figure 5.13 show the same models, but include Thomson scattering. Here we found that the proposed correction provides a less accurate solution that is, however, still closer to the high-resolution model than the old Feautrier scheme. Finally in Figure 5.14, the case of an optically thin line ($\tau_{\text{line}} = 0.5$) shows that both the old and new method have very similar results.

Figure 5.15 shows the application of the NLTE code on a test model for a SN II that con-

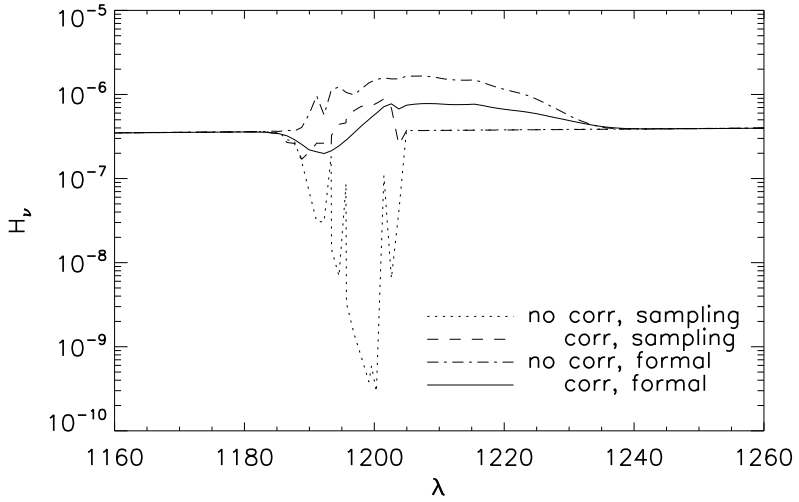

Figure 5.15: Emergent flux in the Lyman-α line of a Type II Supernova model that contained only H and He. For better comparison, both models have been computed neglecting the contribution of these lines to the line blocking in all iterations except the last one. Thus, both models have very similar occupation numbers and temperature structures. The two lines indicated with "sampling" refer to the emergent flux in the last iteration using the opacity sampling technique. The other two lines represent the flux after the first iteration that uses the exact solution. The dotted line and the dash-dotted line belong to the model that uses the standard procedure in the solution of the Feautrier scheme; the dashed line and the solid line refer to the model that had the correction applied.

tained only H and He. For better comparison, both models have been computed neglecting the contribution of these lines to the line blocking in all iterations except the last one. Thus, both models have very similar occupation numbers and temperature structures. Shown in this figure is the emergent flux in the Lyman-α line for two models before and after the first iteration of the detailed solution. The dotted and the dash-dotted line refer to the model that has been calculated using the standard Feautrier scheme described in Section 4.1.1 without correction. The dotted line shows the flux in the last sampling iteration (method I); the dashed-dotted line represents the flux after the first iteration of the detailed solution (method II). The dashed line (method I) and the solid line (method II) represent the flux resulting from the model where the correction has been applied. One can see that the sampling iteration without the correction produces significantly less flux, which also affects the occupation numbers of the corresponding level. This also leads to spurious results in the detailed solution. With the correction included, the flux agrees much better with the detailed solution of method II (exact agreement is not possible due to the limitation of the single *p*-ray approximation; see Section 4.1.1). The detailed solution also shows the absorption and emission part of the P-Cygni profile. The Lyman-α line in this model is an

extreme case. For weaker lines that are blended with other lines, the error introduced is less obvious. Nevertheless, the standard procedure *systematically* underestimates the radiation field, which affects the radiative transition rates and therefore the occupation numbers.

6 Test cases

As a first application of the methods several test calculations have been carried out. In this chapter some preliminary studies of the spectral properties of the 3d-explosion model *f1* recently published by Röpke & Hillebrandt (2005) and the yet unpublished explosion model *inimod4* (Röpke 2005) are presented.

Two different tests cases have been carried out. First an approximate, stratified composition based on explosion model data is used to estimate the influence of the composition of the explosion model on the spectrum. In a second set of test cases, a homogeneous composition has been adjusted independently to obtain a better fit to the observation. From this test the properties of the density profile can be studied.

These models represent the first step of an analysis. The synthetic spectra give an indication of the general properties of the explosion models including the corresponding velocities of line features. For more detailed investigations further refinement of the radiative transfer code is required. In particular, the influence of the single-p-ray approximation in the sampling iteration (see Section 4.1.1) has to be investigated in further detail.

Explosion models

The *f1* model has been discussed in detail in Röpke & Hillebrandt (2005); here only an overview of its properties is given. The calculation considers the entire WD in 4π using a uniform, co-expanding grid with $[512]^3$ cells that tracks the expansion of the WD. The starting condition chosen in this model was an initial distribution of burning bubbles that overlapped in the center of the WD. The total energy released in the explosion was 5.586×10^{50} erg producing $0.579 M_\odot$ iron group elements.

The other model, *inimod4*, was calculated in one octant of the WD using $[256]^3$ cells. This model made use of a hybrid grid with two components. One of the components is set up to track the flame front ensuring a high resolution in the burning region; the other component is co-expanding with the WD where a lower resolution is sufficient. The higher resolution of the burning is particularly important in the very early burning phase. With this approach, it is possible to have a highly resolved initial flame configuration. For the initial condition in this model, a set of 150 separate burning bubbles has been chosen. The intention of this setup was to improve the burning in the central region where the *f1* model shows significant amounts of unburned material.

In both models, the explosion has been followed until 10 s which justifies the assumption

of an homologous expansion (Röpke 2004). In terms of explosion energy, both models are slightly weaker than a normal SN Ia. Figure 6.1 shows the averaged ejecta density of both models. For comparison the 1d-deflagration model W7 by Nomoto et al. (1984) is also shown. As can be seen, the ejecta in W7 have significantly higher kinetic energy.

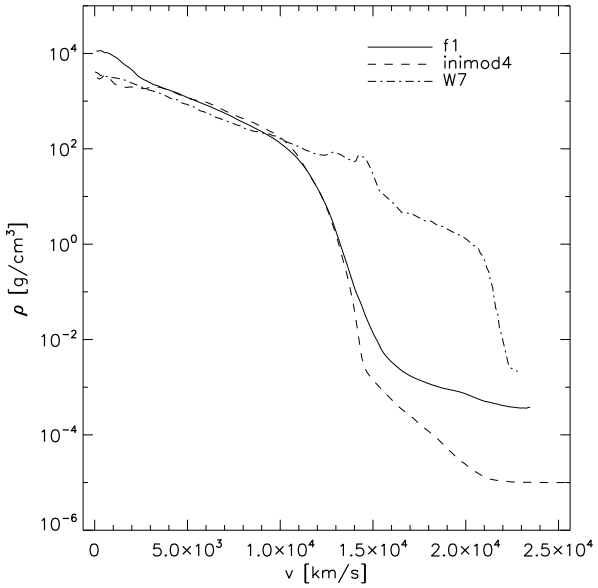

Figure 6.1: Angularly averaged density profiles of the explosion models *f1* and the *inimod4* 10 s after explosion in comparison to the 1d-model W7.

As discussed in Reinecke et al. (2002a), the exact composition of the explosion model is not derived within the hydrodynamic calculation. For efficiency, representative species are chosen such that the energy generation in the burning front is described correctly. Figure 6.2 shows the distribution of these "elements" in velocity space. The detailed nucleosynthesis is determined afterwards from an extensive network calculation (see Travaglio et al. 2004). This calculation, however, has not yet been done for the models under consideration. Here, a rough estimate of the distribution of elements based on the representative species shown in Figure 6.2 has been adopted: the element groups C and O, Ne to Ca, and Ti to Ni are scaled corresponding to the distribution of the "C/O", "Mg", and "Ni" species, respectively. The relative abundance of the elements within a specific group is taken from the model *b30_3d_768* in Travaglio et al. (2004) with consideration of the radioactive decay of ^{56}Ni and ^{56}Co corresponding to the epoch. This approximation is intended to roughly represent the distribution of opacity. It is not expected to result in a detailed and reliable spectrm. Overall, the iron group elements have the largest number of strong lines and therefore dominate the line blocking in the UV. The intermediate mass elements contribute fewer lines, which are visible especially in the optical wavelength bands. Even if the ratios of elements are not completely correct, the corresponding velocities of the sig-

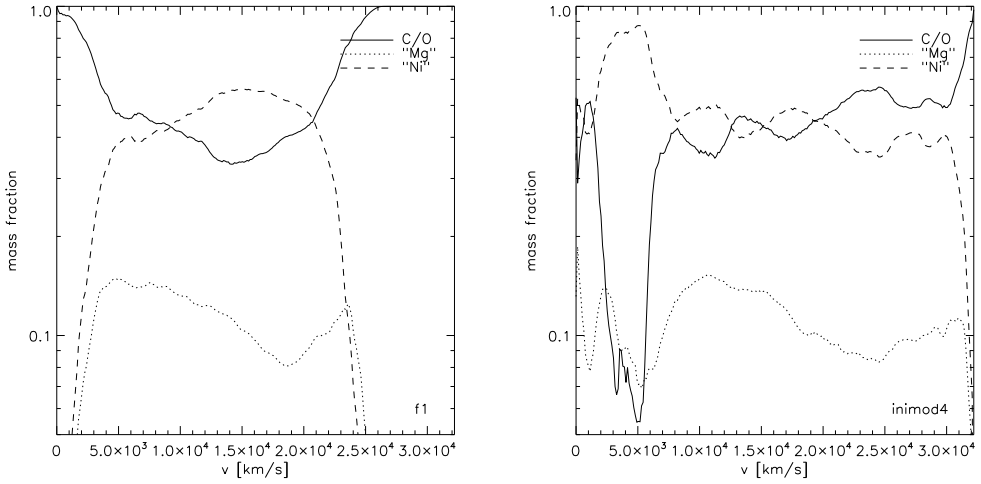

Figure 6.2: Composition of the explosion models *f1* and *inimod4*. Shown here are the "representative" species that are followed in the actual hydrodynamic model. The detailed nucleosynthesis has to be carried out in post-processing with an extensive nucleosynthesis network, which has not yet been done for those models. "C/O" indicates unburned C and O, "Mg" represents all intermediate mass elements, and "Ni" indicates the iron group elements.

nificant line features can be investigated. In the current models the luminosity, which is normally set by the amount of synthesized ^{56}Ni, is set to a typical value independent of the explosion model. The amount of iron group elements generated in the explosion together with the outcome of the nucloesynthesis models in Travaglio et al. (2004) suggests that the explosion models correspond to a dim but still normal SN Ia.

Stratified composition

The first set of calculations was carried out using a stratified composition obtained from the approximation described above.

Figure 6.3 shows the synthetic spectrum obtained from the model *f1* for an epoch 25 days after explosion. The luminosity was set to $\log L/L_\odot = 9.42$ ($1.0 \times 10^{43}\,\mathrm{erg\,s^{-1}}$). For comparison, the observed spectrum of SN1992A (Kirshner et al. 1993) is also shown. The labels indicate some of the ions from which prominent line features originate. (Note that, in the bluer part of the spectrum in particular, the observed features are due to a blend of many different lines. The labels only denote the dominant ion.) The overall shape of the spectrum fits the observation reasonably well. In particular, the prominent features are at roughly the right velocities. The synthetic spectrum, however, also shows prominent line features that are not present in the observation. One can see these especially in the absorption feature at ~ 6500 Å due to C II λ6580; also the absorption in the region around

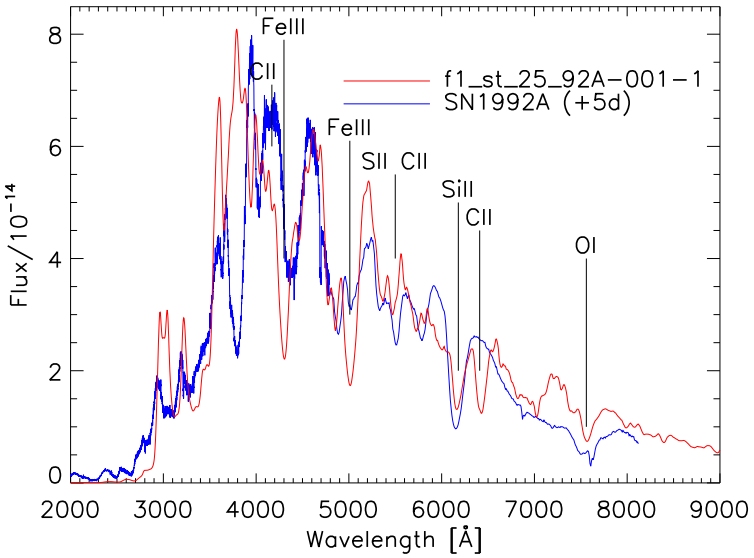

Figure 6.3: Synthetic spectrum for the explosion model *f1* at 25 days after explosion using an approximated stratified composition from the explosion model. For comparison, the observed spectrum of SN1992A at 5 after maximum light is also shown. The synthetic spectrum clearly shows line features (esp. due to C) which are not present in the observation. However, the overall line widths and velocities are reproduced correctly.

4000 Å indicates too much absorption due to C II. The presence of too much unburned material in the ejecta is also suggested by Kozma (2005) who calculated late time nebular spectra for similar explosion models from Travaglio et al. (2004). The position of the photosphere in this model was at approximately 7000 km s^{-1}. As can be seen in Figure 6.1, this corresponds to a region in the density profile where the W7 model roughly agrees with the models under consideration. For those late epochs the impact of the outer low-density regions on the spectrum is small.

Generally, the presence of significant Fe III in the spectrum indicates that the temperature in the region where the lines form is too high for the given epoch. The higher ionization stages are also favored by the fairly shallow density structure in the outer part. The high degree of ionization may be additionally enhanced by the single-*p*-ray approximation in the sampling iterations.

Figure 6.4 shows a comparison between the explosion models *f1* and *inimod4* for the same epoch. The major difference between the two models is the composition in the outer parts. The presence of more iron group elements in the outer region of the model *inimod4* compared to *f1* results in a slightly higher temperature due to the line blanketing effect. This causes a shift in the ionization of the iron group elements toward the doubly ionized species. The smaller number of lines of these species leads to a change in the

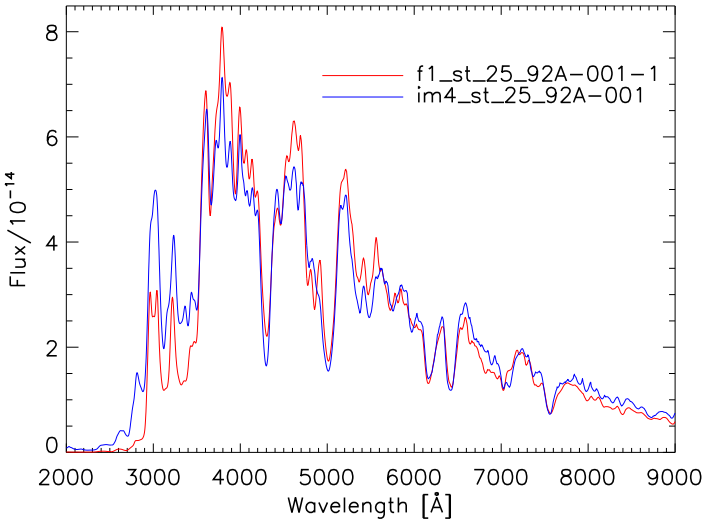

Figure 6.4: Comparison of the synthetic spectra of the explosion models *inimod4* and *f1* for an epoch of 25 days after explosion. The main difference between the spectra is due to the different ionization of iron group elements, which influences the line blocking (see Figure 6.4).

UV flux of the spectrum. In Figure 6.5 the resulting ionization structure in both models is shown for the example of Co. Most line features are formed in radial regions where both models exhibit similar properties. Therefore, the overall appearances of the spectra are similar.

As an example of an early epoch, Figure 6.6 shows a synthetic spectrum for the *f1* model at 5 days after explosion. For comparison, the spectrum of SN1990N at 14 days before maximum light (Leibundgut et al. 1991, P. Mazzali, priv. comm.) is shown. Mazzali et al. (1993) computed synthetic spectra for this object to determine the basic parameters and provide line identifications.

At this epoch the agreement between the synthetic spectrum and the observation is significantly worse. This is probably due to an incorrect composition in the outer region. In early epochs the radial extension of the pseudo-photosphere is much smaller than at later times. Therefore, the composition in those layers has a stronger impact on the spectral features than at later times where the effects of different layers blend together. In this model, most line features form around 11 300 km s^{-1}. The most significant features in the synthetic spectrum are due to C and O plus a contribution of iron group lines. Intermediate mass elements are only marginally represented in this spectrum. In particular, the prominent Si II feature, appearing in the observation at 6000 Å, is far too weak in the model and appears at a too low velocity. Ca is not present in the synthetic spectrum at all. Generally, this suggests that the densities at high velocities are too low (i.e., the kinetic energy of the

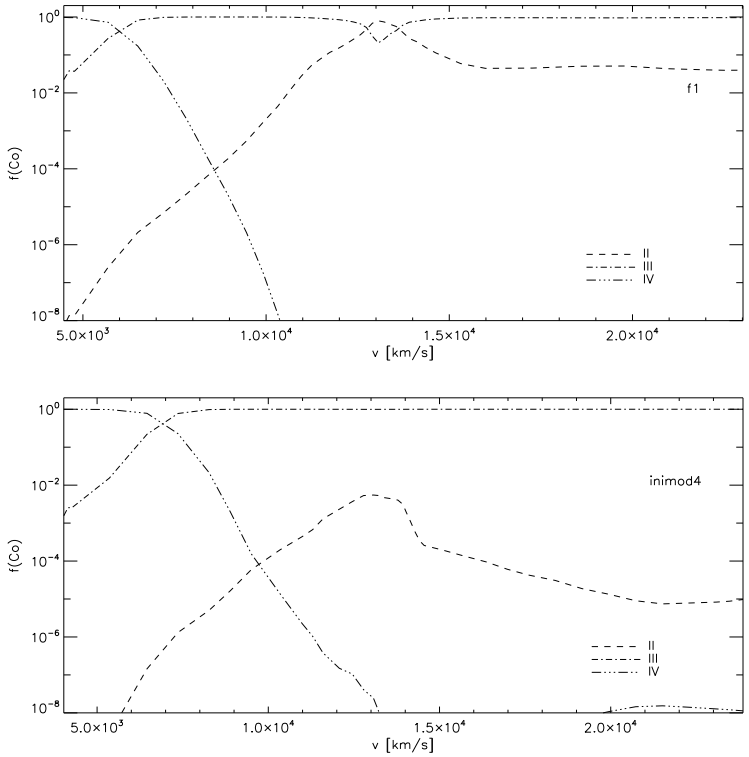

Figure 6.5: Comparison of the ionization structure of Co in the models shown in Figure 6.4. The other iron group elements roughly follow this pattern. The higher fraction of Co II in the upper model corresponds to stronger line blocking in the UV, which can be seen in Figure 6.4.

explosion model is too low). In addition, the production of intermediate mass elements in the outer regions seems to be too small.

Figure 6.7 shows a comparison of the 25 day model previously shown in Figure 6.3 and a model that used the same density profile, but used a homogeneous composition obtained by averaging the element abundances over the mass-shells above the innermost radius of the radiative transfer calculation. As the figure shows in this case the effect of the stratification is only of minor significance, which justifies the general use of a homogenized composition for spectral fits. The stratification will, however, become relevant if certain features originating at velocities above the pseudo-photosphere occur in the spectrum (see, e.g, Kasen et al. 2003). In particular, the correct description of the stratification is important in analyzing a series of subsequent epochs of the same object consistently, as done by Stehle et al. (2004).

Further investigation of these explosion models for later epochs will allow us to see the differences in compositions at low velocities (see Figure 6.2). However, for later epochs the

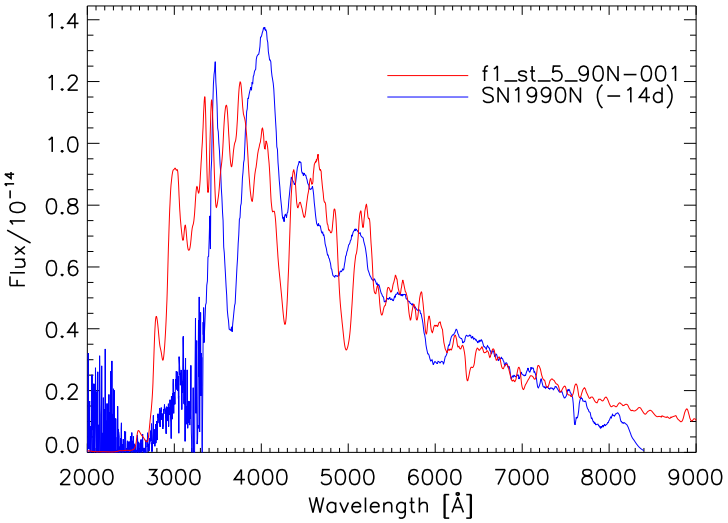

Figure 6.6: Synthetic spectrum for the explosion model *f1* at 5 days after explosion using a stratified composition. For comparison, the observed spectrum of SN1990N at 14 days before maximum light is also shown. Here the composition does not match the observed spectrum and it is also apparent that the line features in the synthetic spectrum occur at significantly lower velocities (i.e., redder wavelengths) than in the observation.

impact of γ-ray energy deposition must be handled properly. These deposition processes have to be implemented into the transfer code before such calculations can be carried out.

Homogeneous composition

As a second test we used the density profiles of the explosion model *f1* and derived synthetic spectra based on a composition that has been determined independent of the explosion model to better fit the observed spectrum. Due to the very similar density profile of the *inimod4* explosion model the resulting spectra are essentially the same as for the *f1* model. Therefore, only models for the *f1* explosion model are presented in this section.

Figure 6.8 shows the synthetic spectrum for the *f1* explosion model 25 days after explosion. This model used a luminosity of $\log L/L_\odot = 9.42$. The photosphere in this model was again at $\sim 6400\,\mathrm{km\,s^{-1}}$, well inside the region where the density follows the behavior of the W7-model.

Although the fit is not perfect, it can be seen that given the correct composition for this epoch, the density structure is able to reproduce the important line features at roughly the right velocities with the correct widths. The missing absorption in the position of the Ca II lines at $\lambda \sim 3900\,\text{Å}$ is, however, not only a problem with composition; the drop of the density at high velocities also causes these lines to become optically thin too velocities

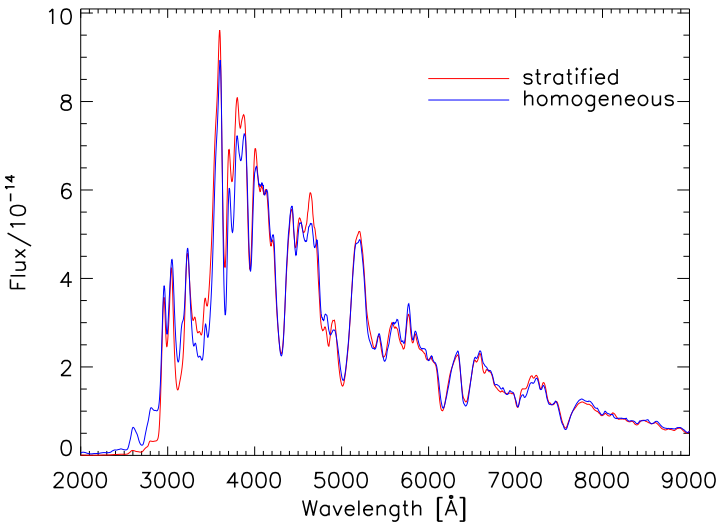

Figure 6.7: Comparison between the model in Figure 6.3 with a stratified abundance and a model using a homogeneous mean abundance. The mean abundance has been obtained by averaging the composition of the explosion model over the mass-shells above the innermost radius of the spectrum calculation. The differences at this epoch are small and the use of the homogenized stratification can be jusified.

that are too low, which introduce a gap in the line blocking through which photons can escape.

Figure 6.9 shows the same model for the epoch 14 days after explosion. The comparison to the observation shows clearly that some line features occur at velocities that are too low. The photospheric velocity in this model was about 9400 km s^{-1}, which is still in the high density region of the model. Some line features are suppressed and too narrow due to the early decline of the density around 12 000 km s^{-1}. As already indicated in the previous model in Figure 6.8, the UV part here also lacks line blocking. This may also be an effect of an incorrect composition. In addition, the overall low kinetic energy of the model may prevent large enough line broadening to efficiently block the radiation in the UV.

In general, these models show that the density profile of the explosion model generates spectra that agree well with the observation at later epochs after maximum light. At early epochs, however, the lack of high velocity material becomes visible in the spectrum. In the spectral region between 3000 and 4000 Å, where the lines are not dense enough to provide a gap-less pseudo-continuum, the missing high-velocity components of strong lines lead to an enhanced flux of photons, which otherwise would be blocked.

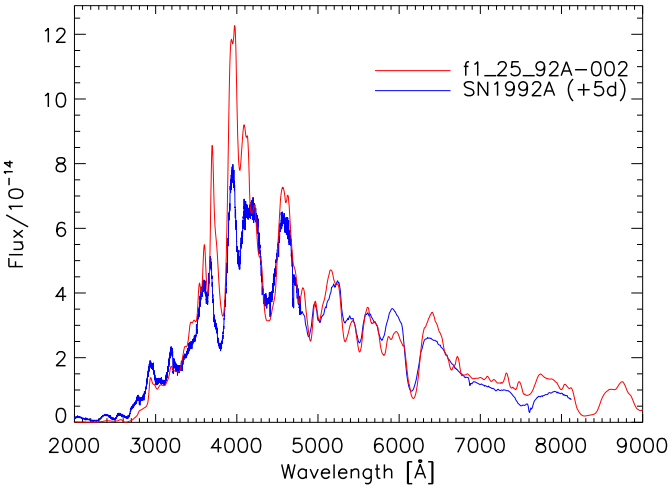

Figure 6.8: Synthetic spectrum for the *f1* explosion model 25 days after explosion. This model used a homogeneous composition, which has been adjusted to match the observed spectrum better. For comparison, the spectrum of SN1992A at 5 days after maximum light is shown. With respect to Figure 6.3, the agreement with the observation is significantly better.

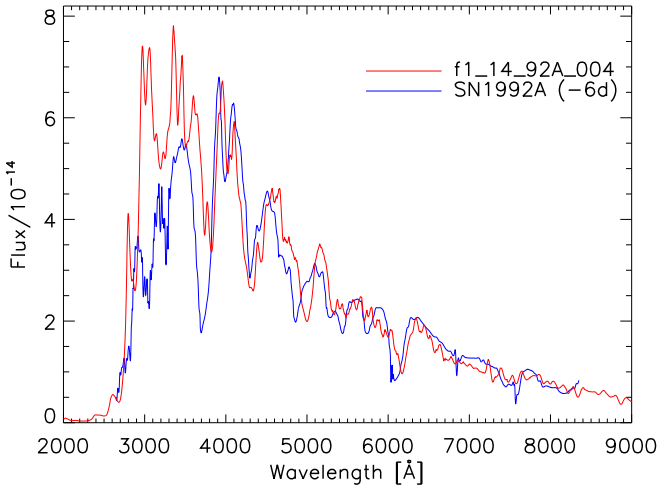

Figure 6.9: Synthetic spectrum for the *f1* explosion model 14 days after explosion. This model used a homogeneous composition, which has been adjusted to match the observed spectrum better. For comparison, the spectrum of SN1992A at 6 days before maximum light is shown. In this model, the lack of high-velocity material in the explosion model can be clearly seen because some spectral features in the synthetic spectrum occur at wavelengths that are significantly too red.

7 Summary, conclusion, and outlook

The aim of this work was to provide a basis for calculating radiative transfer models of supernovae based on a consistent description of the non-equilibrium physics. To reach this goal, the stellar atmosphere code WM-basic that has been developed by the hot-star group of the Universitätssternwarte München has been adapted to the physical conditions in supernova envelopes. The general concept for modeling the radiative transfer adopted in this code is based on an fast, approximate solution employing an opacity sampling method followed by a detailed and exact solution that is equivalent to a solution in comoving frame. This method has been successfully used to model the expanding atmospheres of hot stars. Although the physics treated in SN Ia ejecta and the extended atmospheres of hot stars is similar, significant differences exist that require standard procedures to be revised.

In this work, a special emphasis has been put on the improvement of the inner boundary for the radiative transfer solution because the form commonly used for stellar atmospheres does not sufficiently reflect the non-equilibrium conditions in SN Ia. The lower boundary of stellar atmospheres is clearly defined by the photosphere where the continuum becomes optically thick over the entire spectrum. In SN Ia ejecta, the line opacities dominate over continuum opacity in major parts of the spectrum. In addition, the continuum itself does not accumulate sufficient optical depth to reach thermal conditions. From the standpoint of radiative transfer modeling, SN Ia ejecta have properties between a stellar atmosphere and a gaseous nebula. However, the approximations commonly used to describe those cases are not applicable.

A theoretical basis has been developed that improves the simplifications that enter into the standard diffusive boundary condition and lead to wrong results in SN Ia radiative transfer models. The modifications were necessary because it was found that non-equilibrium effects are important throughout the ejecta even at early epochs where the assumption of a photosphere is generally thought to be justified. In addition, this framework will also allow the consideration of objects at even later epochs, where the photospheric assumption gradually breaks down entirely. To achieve this goal, however, a consistent description of the energy deposition by γ-rays from the radioactive decays of nucleosynthesis products has to be implemented. This topic will be addressed in the near future.

Another aspect of this work was to improve the Feautrier-scheme that is used to solve the radiative transfer in the fast approximate solution for the preliminary iteration cycle. With this modification, the effects of strong line opacities are described more consistently with respect to the final, exact solution of the radiative transfer.

With regard to the preliminary iteration cycle, further work is needed to improve the ap-

proximation used to derive the line opacities and emissivities in the sampling iteration for a single angular ray. Due to the large velocity gradients that are present throughout the supernovae ejecta, this approximation is not as reliable as for stellar atmospheres. A more consistent description of the angular dependence in the opacity sampling method is still needed and will be addressed in the near future of this project.

Some basic test calculations, based on the explosion models recently published by Röpke & Hillebrandt (2005), have been carried out. It was found that the densitiy structure of this explosion model is able to reproduce the correct line widths and velocities at later epochs after maximum light. At earlier epochs, however, the lack of high velocity material is noticable. Using an estimate of the abundances based on the representative species included in the explosion model, the synthetic spectrum indicates the presence of unburned material that is not seen in the observation. These results agree with the findings of Kozma (2005) who derived nebular phase spectra from the previous explosion models in Travaglio et al. (2004). It has to be stressed, however, that a final conclusion is difficult to reach at this stage; the results require a further investigation when more detailed nucleosynthesis data for the explosion model is available. In addition, the uncertainty introduced by the single-p-ray approximation in the sampling-iteration cycles has to be studied in more detail.

The further steps in code development will include incorporating the energy deposition and non-thermal ionization and excitations by γ-rays within the ejecta. The effects introduced by the γ-rays are small in early epochs around maximum, but become significant toward later epochs. A consistent treatment of this energy input will, therefore, allow late epochs extending into the nebular phase of SN Ia to be modeled. For the nebular phase, the atomic data set also has to be extended to include the characteristic forbidden line transitions.

In the short term, systematic quantitiative analysis of observed early time supernova spectra will be carried out. In particular, observed peculiarities and systematic properties will be studied to help establish a theoretical understanding of SN Ia explosions. This theoretical basis is needed to justify the empirical calibration methods that are presently used to make SN Ia a tool for cosmological distance determinations.

Bibliography

Abbott, D. C., Lucy, L. B. (1985): Multiline transfer and the dynamics of stellar winds, *ApJ*, **288**, 679

Aguirre, A. (1999): Intergalactic Dust and Observations of Type IA Supernovae, *ApJ*, **525**, 583

Aldering, G., Adam, G., Antilogus, P., Astier, P., Bacon, R., Bongard, S., Bonnaud, C., Copin, Y., Hardin, D., Henault, F., Howell, D. A., Lemonnier, J., Levy, J., Loken, S. C., Nugent, P. E., Pain, R., Pecontal, A., Pecontal, E., Perlmutter, S., Quimby, R. M., Schahmaneche, K., Smadja, G., Wood-Vasey, W. M. (2002): Overview of the Nearby Supernova Factory. In *Survey and Other Telescope Technologies and Discoveries.*, vol. 4836 of *Proceedings of the SPIE*, p. 61. Sidney

Aller, L. H. (1971): *Atoms, stars, and nebulae*. Harvard University Press, Cambridge

Arnett, W. D. (1980): Analytic solutions for light curves of supernovae of Type II, *ApJ*, **237**, 541

Arnett, W. D. (1982): Type I supernovae. I - Analytic solutions for the early part of the light curve, *ApJ*, **253**, 785

Arnett, W. D. (1996): *Supernovae and nucleosynthesis. An investigation of the history of matter, from the Big Bang to the present*. Princeton series in astrophysics. Princeton University Press, Princeton, NJ

Baade, W., Zwicky, F. (1934a): Cosmic Rays from Super-novae, *Proceedings of the National Academy of Science*, **20**, 259

Baade, W., Zwicky, F. (1934b): On Super-novae, *Proceedings of the National Academy of Science*, **20**, 254

Bartunov, O. S., Tsvetkov, D. Y., Filimonova, I. V. (1994): Distribution of supernovae relative to spiral arms and H II regions, *PASP*, **106**, 1276

Benetti, S., Cappellaro, E., Mazzali, P. A., Turatto, M., Altavilla, G., Bufano, F., Elias-Rosa, N., Kotak, R., Pignata, G., Salvo, M., Stanishev, V. (2004): The diversity of Type Ia Supernovae: evidence for systematics?, *ArXiv Astrophysics e-prints*, . astro-ph/0411059

Benz, W., Cameron, A. G. W., Press, W. H., Bowers, R. L. (1990): Dynamic mass exchange in doubly degenerate binaries. I - 0.9 and 1.2 solar mass stars, *ApJ*, **348**, 647

Brahe, T. (1573): *De nova et nullius aevi memoria prius visa stella, iam pridem anna a NATO Christo 1572, mense Novembri primum conspecta, contemplatio mathematica*. Hafniae, Laurentius, Kopenhagen

Branch, D., Buta, R., Falk, S. W., McCall, M. L., Uomoto, A., Wheeler, J. C., Wills, B. J., Sutherland, P. G. (1982): Interpretation of the maximum light spectrum of a Type I supernova, *ApJ*, **252**, L61

Branch, D., Doggett, J. B., Nomoto, K., Thielemann, F. K. (1985): Accreting white dwarf models for the type I supernovae. IV. The optical spectrum of a carbon-deflagration supernova, *ApJ*, **294**, 619

Branch, D., Livio, M., Yungelson, L. R., Boffi, F. R., Baron, E. (1995): In Search of the Progenitors of Type IA Supernovae, *PASP*, **107**, 1019

Branch, D., Romanishin, W., Baron, E. (1996): Statistical Connections between the Properties of Type IA Supernovae and the B-V Colors of Their Parent Galaxies, and the Value of H_0, *ApJ*, **465**, 73

Burkert, A., Ruiz-Lapuente, P. (1997): Dormant Dwarf Spheroidal Galaxies, Deactivated by Type IA Supernovae, *ApJ*, **480**, 297

Burrows, A., Hayes, J. (1996): Pulsar Recoil and Gravitational Radiation Due to Asymmetrical Stellar Collapse and Explosion, *Physical Review Letters*, **76**, 352

Caldwell, R. R., Dave, R., Steinhardt, P. J. (1998): Cosmological Imprint of an Energy Component with General Equation of State, *Physical Review Letters*, **80**, 1582

Cappellaro, E., Evans, R., Turatto, M. (1999): A new determination of supernova rates and a comparison with indicators for galactic star formation, *A&A*, **351**, 459

Cappellaro, E., Mazzali, P. A., Benetti, S., Danziger, I. J., Turatto, M., della Valle, M., Patat, F. (1997): SN IA light curves and radioactive decay, *A&A*, **328**, 203

Carroll, S. M., Press, W. H., Turner, E. L. (1992): The cosmological constant, *ARA&A*, **30**, 499

Castor, J. I. (1970): Spectral line formation in Wolf-rayet envelopes, *MNRAS*, **149**, 111

Ciotti, L., Pellegrini, S., Renzini, A., D'Ercole, A. (1991): Winds, outflows, and inflows in X-ray elliptical galaxies, *ApJ*, **376**, 380

Colgate, S. A., McKee, C. (1969): Early Supernova Luminosity, *ApJ*, **157**, 623

Colgate, S. A., Petschek, A. G., Kriese, J. T. (1980): The luminosity of type I supernovae, *ApJ*, **237**, L81

Contardo, G., Leibundgut, B., Vacca, W. D. (2000): Epochs of maximum light and bolometric light curves of type Ia supernovae, *A&A*, **359**, 876

Cunto, W., Mendoza, C. (1992): The Opacity Project - the Topbase Atomic Database, *Revista Mexicana de Astronomia y Astrofisica, vol. 23*, **23**, 107

Eastman, R. G., Pinto, P. A. (1993): Spectrum formation in supernovae - Numerical techniques, *ApJ*, **412**, 731

Eissner, W., Jones, M., Nussbaumer, H. (1974): Techniques for the calculation of atomic structures and radiative data including relativistic corrections, *Computer Physics Communications*, **8**, 270

Ferrara, A., Tolstoy, E. (2000): The role of stellar feedback and dark matter in the evolution of dwarf galaxies, *MNRAS*, **313**, 291

Filippenko, A. V. (1988): Supernova 1987K - Type II in youth, type Ib in old age, *AJ*, **96**, 1941

Filippenko, A. V. (1989): Type IA supernovae in elliptical and spiral galaxies - Possible differences in photometric homogeneity, *PASP*, **101**, 588

Filippenko, A. V. (1997): Optical Spectra of Supernovae, *ARA&A*, **35**, 309

Fisher, A., Branch, D., Hatano, K., Baron, E. (1999): On the spectrum and nature of the peculiar Type IA supernova 1991T, *MNRAS*, **304**, 67

Fisher, A., Branch, D., Nugent, P., Baron, E. (1997): Evidence for a High-velocity Carbon-rich Layer in the Type IA SN 1990N, *ApJ*, **481**, L89+

Fisher, A. K. (2000): *Direct analysis of type Ia supernovae spectra*. Ph.D. thesis, University of Oklahoma

Gamezo, V. N., Khokhlov, A. M., Oran, E. S. (2004): Deflagrations and Detonations in Thermonuclear Supernovae, *Physical Review Letters*, **92(21)**, 211102

Gamezo, V. N., Khokhlov, A. M., Oran, E. S., Chtchelkanova, A. Y., Rosenberg, R. O. (2003): Thermonuclear Supernovae: Simulations of the Deflagration Stage and Their Implications, *Science*, **299**, 77

Green, D. A., Stephenson, F. R. (2003): Historical Supernovae, *Lecture Notes in Physics, Berlin Springer Verlag*, **598**, 7

Gustafsson, B. (1971): A Feautrier-Type Method for Model Atmospheres Including Convection, *A&A*, **10**, 187

Hamuy, M., Phillips, M. M., Suntzeff, N. B., Schommer, R. A., Maza, J., Antezan, A. R., Wischnjewsky, M., Valladares, G., Muena, C., Gonzales, L. E., Aviles, R., Wells, L. A., Smith, R. C., Navarrete, M., Covarrubias, R., Williger, G. M., Walker, A. R., Layden, A. C., Elias, J. H., Baldwin, J. A., Hernandez, M., Tirado, H., Ugarte, P., Elston, R., Saavedra, N., Barrientos, F., Costa, E., Lira, P., Ruiz, M. T., Anguita, C., Gomez, X., Ortiz, P., della Valle, M., Danziger, J., Storm, J., Kim, Y.-C., Bailyn, C., Rubenstein, E. P., Tucker, D., Cersosimo, S., Mendez, R. A., Siciliano, L., Sherry, W., Chaboyer, B., Koopmann, R. A., Geisler, D., Sarajedini, A., Dey, A., Tyson, N., Rich, R. M., Gal, R., Lamontagne, R., Caldwell, N., Guhathakurta, P., Phillips, A. C., Szkody, P., Prosser, C., Ho, L. C., McMahan, R., Baggley, G., Cheng, K.-P., Havlen, R., Wakamatsu, K., Janes, K., Malkan, M., Baganoff, F., Seitzer, P., Shara, M., Sturch, C., Hesser, J., Hartig, A. N. P., Hughes, J., Welch, D., Williams, T. B., Ferguson, H., Francis, P. J., French, L., Bolte, M., Roth, J., Odewahn, S., Howell, S., Krzeminski, W. (1996a): BVRI Light Curves for 29 Type IA Supernovae, *AJ*, **112**, 2408

Hamuy, M., Phillips, M. M., Suntzeff, N. B., Schommer, R. A., Maza, J., Smith, R. C., Lira, P., Aviles, R. (1996b): The Morphology of Type IA Supernovae Light Curves, *AJ*, **112**, 2438

Han, Z., Podsiadlowski, P. (2004): The single-degenerate channel for the progenitors of Type Ia supernovae, *MNRAS*, **350**, 1301

Hartwig, E. (1898): Über den grossen Andromedanebel, *Astronomische Nachrichten*, **148**, 11

Hauschildt, P., Baron, E. (1999): Numerical solution of the expanding stellar atmosphere problem, *J. Comp. Applied Math.*, **109**, 41

Hillebrandt, W., Niemeyer, J. C. (2000): Type Ia Supernova Explosion Models, *ARA&A*, **38**, 191

Hoffmann, T. (2004): *Synthetic spectra of massive stars as a tool for the spectral analysis of stars and stellar clusters*. Ph.D. thesis, Ludwigs-Maximilians-Universität München. URL: `http://edoc.ub.uni-muenchen.de/archive/00002719/`

Höflich, P., Gerardy, C. L., Nomoto, K., Motohara, K., Fesen, R. A., Maeda, K., Ohkubo, T., Tominaga, N. (2004): Signature of Electron Capture in Iron-rich Ejecta of SN 2003du, *ApJ*, **617**, 1258

Höflich, P., Khokhlov, A. M., Wheeler, J. C. (1995): Delayed detonation models for normal and subluminous type IA sueprnovae: Absolute brightness, light curves, and molecule formation, *ApJ*, **444**, 831

Hoyle, F., Fowler, W. A. (1960): Nucleosynthesis in Supernovae, *ApJ*, **132**, 565

Hummer, D. G. (1963): The ionization structure of planetary nebulae, II. Collisional cooling of pure hydrogen nebulae, *MNRAS*, **125**, 461

Hummer, D. G., Berrington, K. A., Eissner, W., Pradhan, A. K., Saraph, H. E., Tully, J. A. (1993): Atomic data from the IRON Project. 1: Goals and methods, *A&A*, **279**, 298

Hummer, D. G., Rybicki, G. B. (1985): The Sobolev approximation for line formation with continuous opacity, *ApJ*, **293**, 258

Hummer, D. G., Seaton, M. J. (1963): The ionization structure of planetary nebulae, I. Pure hydrogen nebulae, *MNRAS*, **125**, 437

Iben, I., Tutukov, A. V. (1984): Supernovae of type I as end products of the evolution of binaries with components of moderate initial mass (M not greater than about 9 solar masses), *ApJS*, **54**, 335

Iben, I. J., Tutukov, A. V. (1994): Helium-accreting degenerate dwarfs as presupernovae and scenarios for the ultrasoft x-ray sources, *ApJ*, **431**, 264

Iben, I. J., Tutukov, A. V. (1999): On the Evolution of Close Triple Stars That Produce Type IA Supernovae, *ApJ*, **511**, 324

Iwamoto, K., Mazzali, P. A., Nomoto, K., Umeda, H., Nakamura, T., Patat, F., Danziger, I. J., Young, T. R., Suzuki, T., Shigeyama, T., Augusteijn, T., Doublier, V., Gonzalez, J.-F., Boehnhardt, H., Brewer, J., Hainaut, O. R., Lidman, C., Leibundgut, B., Cappellaro, E., Turatto, M., Galama, T. J., Vreeswijk, P. M., Kouveliotou, C., van Paradijs, J., Pian, E., Palazzi, E., Frontera, F. (1998): A hypernova model for the supernova associated with the gamma-ray burst of 25 April 1998, *Nature*, **395**, 672

Janka, H.-T., Scheck, L., Kifonidis, K., Mueller, E., Plewa, T. (2004): Supernova Asymmetries and Pulsar Kicks – Views on Controversial Issues, *ArXiv Astrophysics e-prints*, . astro-ph/0408439

Karp, A. H., Lasher, G., Chan, K. L., Salpeter, E. E. (1977): The opacity of expanding media - The effect of spectral lines, *ApJ*, **214**, 161

Kasen, D. (2004): *Aspherical Supernovae*. Ph.D. thesis, University of California, Berkeley

Kasen, D., Nugent, P., Wang, L., Howell, D. A., Wheeler, J. C., Höflich, P., Baade, D., Baron, E., Hauschildt, P. H. (2003): Analysis of the Flux and Polarization Spectra of the Type Ia Supernova SN 2001el: Exploring the Geometry of the High-Velocity Ejecta, *ApJ*, **593**, 788

Kifonidis, K., Plewa, T., Janka, H.-T., Müller, E. (2003): Non-spherical core collapse supernovae. I. Neutrino-driven convection, Rayleigh-Taylor instabilities, and the formation and propagation of metal clumps, *A&A*, **408**, 621

Kirshner, R. P., Jeffery, D. J., Leibundgut, B., Challis, P. M., Sonneborn, G., Phillips, M. M., Suntzeff, N. B., Smith, R. C., Winkler, P. F., Winge, C., Hamuy, M., Hunter, D. A., Roth, K. C., Blades, J. C., Branch, D., Chevalier, R. A., Fransson, C., Panagia,

N., Wagoner, R. V., Wheeler, J. C., Harkness, R. P. (1993): SN 1992A: Ultraviolet and Optical Studies Based on HST, IUE, and CTIO Observations, *ApJ*, **415**, 589

Kozma, C. (2005): In preparation

Kozma, C., Fransson, C. (1992): Gamma-ray deposition and nonthermal excitation in supernovae, *ApJ*, **390**, 602

Kubát, J., Puls, J., Pauldrach, A. W. A. (1999): Thermal balance of electrons in calculations of model stellar atmospheres, *A&A*, **341**, 587

Kuchner, M. J., Kirshner, R. P., Pinto, P. A., Leibundgut, B. (1994): Evidence for Ni-56 yields Co-56 yields Fe-56 decay in type IA supernovae, *ApJ*, **426**, L89

Kurucz, R. L. (1992): Atomic and Molecular Data for Opacity Calculations, *Revista Mexicana de Astronomia y Astrofisica, vol. 23*, **23**, 45

Leibundgut, B. (2000): Type Ia Supernovae, *A&A Rev.*, **10**, 179

Leibundgut, B. (2001): Cosmological Implications from Observations of Type Ia Supernovae, *ARA&A*, **39**, 67

Leibundgut, B. (2004): Are Type Ia Supernovae Standard Candles?, *Ap&SS*, **290**, 29

Leibundgut, B., Kirshner, R. P., Filippenko, A. V., Shields, J. C., Foltz, C. B., Phillips, M. M., Sonneborn, G. (1991): Premaximum observations of the type IA SN 1990N, *ApJ*, **371**, L23

Lentz, E. J., Baron, E., Branch, D., Hauschildt, P. H. (2001): Non-LTE Synthetic Spectral Fits to the Type Ia Supernova 1994D in NGC 4526, *ApJ*, **557**, 266

Livio, M. (2000): The Progenitors of Type Ia Supernovae. In *Type Ia Supernovae, Theory and Cosmology*, edited by J. C. Niemeyer, J. W. Truran, p. 33. Cambridge University Press

Livne, E., Arnett, D. (1993): On the Instability of Deflagration Fronts in White Dwarfs, *ApJ*, **415**, L107

Lucy, L. B. (1964): A Temperature-Correction Procedure, *SAO Special Report*, **167**, 93

Lucy, L. B. (2005): Monte Carlo techniques for time-dependent radiative transfer in 3-D supernovae, *A&A*, **429**, 19

Lundmark, K. (1920): *Svenska Vetenkapsakad.Handl.*, **80**, 8

Mészáros, P. (2003): γ-ray bursts: The supernova connection, *Nature*, **423**, 809

Mazzali, P. A., Cappellaro, E., Danziger, I. J., Turatto, M., Benetti, S. (1998): Nebular Velocities in Type IA Supernovae and Their Relationship to Light Curves, *ApJ*, **499**, L49

Mazzali, P. A., Lucy, L. B. (1993): The application of Monte Carlo methods to the synthesis of early-time supernovae spectra, *A&A*, **279**, 447

Mazzali, P. A., Lucy, L. B., Danziger, I. J., Gouiffes, C., Cappellaro, E., Turatto, M. (1993): Models for the early-time spectral evolution of the 'standard' type IA supernova 1990N, *A&A*, **269**, 423

Meikle, W. P. S. (2000): The absolute infrared magnitudes of type Ia supernovae, *MNRAS*, **314**, 782

Mihalas, D. (1978): *Stellar atmospheres*. W. H. Freeman and Co., San Francisco, 2nd edn.

Mihalas, D., Hummer, D. G. (1973): Analyses of light-ion spectra in stellar atmospheres. III. Nitrogen in the O stars., *ApJ*, **179**, 827

Mihalas, D., Weibel-Mihalas, B. (1984): *Foundations of radiation hydrodynamics*. Oxford University Press, New York

Minkowski, R. (1941): Spectra of Supernovae, *PASP*, **53**, 224

Mochkovitch, R., Guerrero, J., Segretain, L. (1997): The merging of white dwarfs. In *NATO ASIC Proc. 486: Thermonuclear Supernovae*, p. 187

Müller, E., Arnett, W. D. (1982): Numerical studies of nonspherical carbon combustion models, *ApJ*, **261**, L109

Niemeyer, J. C., Hillebrandt, W. (1995): Turbulent Nuclear Flames in Type IA Supernovae, *ApJ*, **452**, 769

Nomoto, K. (1982a): Accreting white dwarf models for type 1 supernovae. II - Off-center detonation supernovae, *ApJ*, **257**, 780

Nomoto, K. (1982b): Accreting white dwarf models for type I supernovae. I - Presupernova evolution and triggering mechanisms, *ApJ*, **253**, 798

Nomoto, K., Iben, I. (1985): Carbon ignition in a rapidly accreting degenerate dwarf - A clue to the nature of the merging process in close binaries, *ApJ*, **297**, 531

Nomoto, K., Iwamoto, K., Suzuki, T. (1995): The evolution and explosion of massive binary stars and Type Ib-Ic-IIb-IIL supernovae, *Phys. Rep.*, **256**, 173

Nomoto, K., Kondo, Y. (1991): Conditions for accretion-induced collapse of white dwarfs, *ApJ*, **367**, L19

Nomoto, K., Thielemann, F.-K., Yokoi, K. (1984): Accreting white dwarf models of Type I supernovae. III - Carbon deflagration supernovae, *ApJ*, **286**, 644

Nomoto, K., Uenishi, T., Kobayashi, C., Umeda, H., Ohkubo, T., Hachisu, I., Kato, M. (2003): Type Ia Supernovae: Progenitors and Diversities. In *From Twilight to Highlight: The Physics of Supernovae*, p. 115

Nomoto, K., Yamaoka, H., Shigeyama, T., Kumagai, S., Tsujimoto, T. (1994): Type I supernovae and evolution of interacting binaries. In *Supernovae*, edited by J. Audouze, S. Bludman, R. Mochovitch, J. Zin-Justin, Les Houches Session LIV, p. 199. Elsevier, Amsterdam

Nugent, P., Baron, E., Branch, D., Fisher, A., Hauschildt, P. H. (1997): Synthetic Spectra of Hydrodynamic Models of Type IA Supernovae, *ApJ*, **485**, 812

Nugent, P., Baron, E., Hauschildt, P. H., Branch, D. (1995a): Spectrum synthesis of the Type IA supernovae SN 1992A and SN 1981B, *ApJ*, **441**, L33

Nugent, P., Phillips, M., Baron, E., Branch, D., Hauschildt, P. (1995b): Evidence for a Spectroscopic Sequence among Type 1a Supernovae, *ApJ*, **455**, L147

Nussbaumer, H., Storey, P. J. (1978): The C III transition probabilities, *A&A*, **64**, 139

Osterbrock, D. E. (1989): *Astrophysics of gaseous nebulae and active galactic nuclei*. University Science Books, Sausalito, CA

Pauldrach, A. (1987): Radiation driven winds of hot luminous stars. III - Detailed statistical equilibrium calculations for hydrogen to zinc, *A&A*, **183**, 295

Pauldrach, A. W. A. (2003): Hot Stars: Old-Fashioned or Trendy?, *Reviews of Modern Astronomy*, **16**, 133

Pauldrach, A. W. A., Duschinger, M., Mazzali, P. A., Puls, J., Lennon, M., Miller, D. L. (1996): NLTE models for synthetic spectra of type IA supernovae. The influence of line blocking, *A&A*, **312**, 525

Pauldrach, A. W. A., Hoffmann, T. L., Lennon, M. (2001): Radiation-driven winds of hot luminous stars. XIII. A description of NLTE line blocking and blanketing towards realistic models for expanding atmospheres, *A&A*, **375**, 161

Pauldrach, A. W. A., Hoffmann, T. L., Méndez, R. H. (2004): Radiation-driven winds of hot luminous stars. XV. Constraints on the mass-luminosity relation of central stars of planetary nebulae, *A&A*, **419**, 1111

Pauldrach, A. W. A., Kudritzki, R. P., Puls, J., Butler, K. (1990): Radiation driven winds of hot luminous stars. VII - The evolution of massive stars and the morphology of stellar wind spectra, *A&A*, **228**, 125

Pauldrach, A. W. A., Lennon, M., Hoffmann, T. L., Sellmaier, F., Kudritzki, R.-P., Puls, J. (1998): Realistic Models for Expanding Atmospheres. In *ASP Conf. Ser. 131: Properties of Hot Luminous Stars*, p. 258

Percival, W. J., Baugh, C. M., Bland-Hawthorn, J., Bridges, T., Cannon, R., Cole, S., Colless, M., Collins, C., Couch, W., Dalton, G., De Propris, R., Driver, S. P., Efstathiou, G., Ellis, R. S., Frenk, C. S., Glazebrook, K., Jackson, C., Lahav, O., Lewis, I., Lumsden, S., Maddox, S., Moody, S., Norberg, P., Peacock, J. A., Peterson, B. A., Sutherland, W., Taylor, K. (2001): The 2dF Galaxy Redshift Survey: the power spectrum and the matter content of the Universe, *MNRAS*, **327**, 1297

Perlmutter, S., Aldering, G., Goldhaber, G., Knop, R. A., Nugent, P., Castro, P. G., Deustua, S., Fabbro, S., Goobar, A., Groom, D. E., Hook, I. M., Kim, A. G., Kim, M. Y., Lee, J. C., Nunes, N. J., Pain, R., Pennypacker, C. R., Quimby, R., Lidman, C., Ellis, R. S., Irwin, M., McMahon, R. G., Ruiz-Lapuente, P., Walton, N., Schaefer, B., Boyle, B. J., Filippenko, A. V., Matheson, T., Fruchter, A. S., Panagia, N., Newberg, H. J. M., Couch, W. J., The Supernova Cosmology Project (1999): Measurements of Omega and Lambda from 42 High-Redshift Supernovae, *ApJ*, **517**, 565

Perlmutter, S., Gabi, S., Goldhaber, G., Goobar, A., Groom, D. E., Hook, I. M., Kim, A. G., Kim, M. Y., Lee, J. C., Pain, R., Pennypacker, C. R., Small, I. A., Ellis, R. S., McMahon, R. G., Boyle, B. J., Bunclark, P. S., Carter, D., Irwin, M. J., Glazebrook, K., Newberg, H. J. M., Filippenko, A. V., Matheson, T., Dopita, M., Couch, W. J., The Supernova Cosmology Project (1997): Measurements of the Cosmological Parameters Omega and Lambda from the First Seven Supernovae at $Z > 0.35$, *ApJ*, **483**, 565

Perlmutter, S., Schmidt, B. P. (2003): Measuring Cosmology with Supernovae, *Lecture Notes in Physics, Berlin Springer Verlag*, **598**, 195

Phillips, M. M. (1993): The absolute magnitudes of Type IA supernovae, *ApJ*, **413**, L105

Phillips, M. M., Lira, P., Suntzeff, N. B., Schommer, R. A., Hamuy, M., Maza, J. (1999): The Reddening-Free Decline Rate Versus Luminosity Relationship for Type IA Supernovae, *AJ*, **118**, 1766

Pignata, G., Patat, F., Benetti, S., Blinnikov, S., Hillebrandt, W., Kotak, R., Leibundgut, B., Mazzali, P. A., Meikle, P., Qiu, Y., Ruiz-Lapuente, P., Smartt, S. J., Sorokina, E., Stritzinger, M., Stehle, M., Turatto, M., Marsh, T., Martin-Luis, F., McBride, N., Mendez, J., Morales-Rueda, L., Narbutis, D., Street, R. (2004): Photometric observations of the Type Ia SN 2002er in UGC 10743, *MNRAS*, **355**, 178

Pinto, P. A., Eastman, R. G. (2000a): The Physics of Type IA Supernova Light Curves. I. Analytic Results and Time Dependence, *ApJ*, **530**, 744

Pinto, P. A., Eastman, R. G. (2000b): The Physics of Type IA Supernova Light Curves. II. Opacity and Diffusion, *ApJ*, **530**, 757

Pomraning, G. C. (1973): *The equations of radiation hydrodynamics*. International Series of Monographs in Natural Philosophy, Oxford: Pergamon Press, 1973

Puls, J., Hummer, D. G. (1988): The Sobolev approximation for the line force and line source function in a spherically-symmetrical stellar wind with continuum opacity, *A&A*, **191**, 87

Reinecke, M., Hillebrandt, W., Niemeyer, J. C. (2002a): Refined numerical models for multidimensional type Ia supernova simulations, *A&A*, **386**, 936

Reinecke, M., Hillebrandt, W., Niemeyer, J. C. (2002b): Three-dimensional simulations of type Ia supernovae, *A&A*, **391**, 1167

Renzini, A. (1999): Chemical Evolution on the Scale of Clusters of Galaxies, and Beyond. In *Chemical Evolution from Zero to High Redshift*, p. 185

Riess, A. G., Filippenko, A. V., Challis, P., Clocchiatti, A., Diercks, A., Garnavich, P. M., Gilliland, R. L., Hogan, C. J., Jha, S., Kirshner, R. P., Leibundgut, B., Phillips, M. M., Reiss, D., Schmidt, B. P., Schommer, R. A., Smith, R. C., Spyromilio, J., Stubbs, C., Suntzeff, N. B., Tonry, J. (1998): Observational Evidence from Supernovae for an Accelerating Universe and a Cosmological Constant, *AJ*, **116**, 1009

Riess, A. G., Filippenko, A. V., Li, W., Treffers, R. R., Schmidt, B. P., Qiu, Y., Hu, J., Armstrong, M., Faranda, C., Thouvenot, E., Buil, C. (1999a): The Rise Time of Nearby Type IA Supernovae, *AJ*, **118**, 2675

Riess, A. G., Kirshner, R. P., Schmidt, B. P., Jha, S., Challis, P., Garnavich, P. M., Esin, A. A., Carpenter, C., Grashius, R., Schild, R. E., Berlind, P. L., Huchra, J. P., Prosser, C. F., Falco, E. E., Benson, P. J., Briceño, C., Brown, W. R., Caldwell, N., dell'Antonio, I. P., Filippenko, A. V., Goodman, A. A., Grogin, N. A., Groner, T., Hughes, J. P., Green, P. J., Jansen, R. A., Kleyna, J. T., Luu, J. X., Macri, L. M., McLeod, B. A., McLeod, K. K., McNamara, B. R., McLean, B., Milone, A. A. E., Mohr, J. J., Moraru, D., Peng, C., Peters, J., Prestwich, A. H., Stanek, K. Z., Szentgyorgyi, A., Zhao, P. (1999b): BVRI Light Curves for 22 Type IA Supernovae, *AJ*, **117**, 707

Riess, A. G., Press, W. H., Kirshner, R. P. (1996): Is the Dust Obscuring Supernovae in Distant Galaxies the Same as Dust in the Milky Way?, *ApJ*, **473**, 588

Riess, A. G., Strolger, L., Tonry, J., Casertano, S., Ferguson, H. C., Mobasher, B., Challis, P., Filippenko, A. V., Jha, S., Li, W., Chornock, R., Kirshner, R. P., Leibundgut, B., Dickinson, M., Livio, M., Giavalisco, M., Steidel, C. C., Benítez, T., Tsvetanov, Z. (2004): Type Ia Supernova Discoveries at z > 1 from the Hubble Space Telescope: Evidence for Past Deceleration and Constraints on Dark Energy Evolution, *ApJ*, **607**, 665

Röpke, F. K. (2004): Following multi-dimensional Type Ia supernova explosion models to homologous expansion, *ArXiv Astrophysics e-prints*, . `astro-ph/0408296`

Röpke, F. K. (2005): In preparation

Röpke, F. K., Hillebrandt, W. (2004): The case against the progenitor's carbon-to-oxygen ratio as a source of peak luminosity variations in type Ia supernovae, *A&A*, **420**, L1

Röpke, F. K., Hillebrandt, W. (2005): Full-star type Ia supernova explosion models, *A&A*, **431**, 635

Röpke, F. K., Hillebrandt, W., Niemeyer, J. C. (2004a): The cellular burning regime in type Ia supernova explosions. I. Flame propagation into quiescent fuel, *A&A*, **420**, 411

Röpke, F. K., Hillebrandt, W., Niemeyer, J. C. (2004b): The cellular burning regime in type Ia supernova explosions. II. Flame propagation into vortical fuel, *A&A*, **421**, 783

Röpke, F. K., Niemeyer, J. C., Hillebrandt, W. (2003): On the Small-Scale Stability of Thermonuclear Flames in Type Ia Supernovae, *ApJ*, **588**, 952

Ruiz-Lapuente, P., Canal, R. (1998): Type IA Supernova Counts at High z: Signatures of Cosmological Models and Progenitors, *ApJ*, **497**, L57

Ruiz-Lapuente, P., Comeron, F., Méndez, J., Canal, R., Smartt, S. J., Filippenko, A. V., Kurucz, R. L., Chornock, R., Foley, R. J., Stanishev, V., Ibata, R. (2004): The binary progenitor of Tycho Brahe's 1572 supernova, *Nature*, **431**, 1069

Rybicki, G. B. (1971): A modified Feautrier method, *Journal of Quantitative Spectroscopy and Radiative Transfer*, **11**, 589

Rybicki, G. B., Hummer, D. G. (1994): An accelerated lambda iteration method for multilevel radiative transfer. III. Noncoherent electron scattering, *A&A*, **290**, 553

Rybicki, G. B., Lightman, A. P. (1979): *Radiative processes in astrophysics*. New York, Wiley-Interscience, 1979. 393 p.

Salvo, M. E., Cappellaro, E., Mazzali, P. A., Benetti, S., Danziger, I. J., Patat, F., Turatto, M. (2001): The template type Ia supernova 1996X, *MNRAS*, **321**, 254

Santolaya-Rey, A. E., Puls, J., Herrero, A. (1997): Atmospheric NLTE-models for the spectroscopic analysis of luminous blue stars with winds, *A&A*, **323**, 488

Scheck, L., Plewa, T., Janka, H.-T., Kifonidis, K., Müller, E. (2004): Pulsar Recoil by Large-Scale Anisotropies in Supernova Explosions, *Physical Review Letters*, **92(1)**, 011103

Schmidt, B. P., Suntzeff, N. B., Phillips, M. M., Schommer, R. A., Clocchiatti, A., Kirshner, R. P., Garnavich, P., Challis, P., Leibundgut, B., Spyromilio, J., Riess, A. G., Filippenko, A. V., Hamuy, M., Smith, R. C., Hogan, C., Stubbs, C., Diercks, A., Reiss, D., Gilliland, R., Tonry, J., Maza, J., Dressler, A., Walsh, J., Ciardullo, R. (1998): The High-Z Supernova Search: Measuring Cosmic Deceleration and Global Curvature of the Universe Using Type IA Supernovae, *ApJ*, **507**, 46

Schmidt, W., Hillebrandt, W., Niemeyer, J. C. (2004): On self-similarity properties of isotropic turbulence in numerical simulations of the compressible Euler equations, *ArXiv Astrophysics e-prints*, . astro-ph/0406083

Seaton, M. J., Yan, Y., Mihalas, D., Pradhan, A. K. (1994): Opacities for Stellar Envelopes, *MNRAS*, **266**, 805

Sellmaier, F. (1996): Ph.D. thesis, Ludwigs-Maximilians-Universität München

Sellmaier, F., Puls, J., Kudritzki, R. P., Gabler, A., Gabler, R., Voels, S. A. (1993): Unified NLTE Model Atmospheres Including Spherical Extension and Stellar Winds - Part Four - Improved Line Transfer and Wind Contamination of H he Profiles, *A&A*, **273**, 533

Sobolev, V. V. (1957): The Diffusion of Lα Radiation in Nebulae and Stellar Envelopes., *Soviet Astronomy*, **1**, 678

Sorokina, E., Blinnikov, S. (2003): Light Curves of Type Ia Supernovae as a Probe for an Explosion Model. In *From Twilight to Highlight: The Physics of Supernovae*, edited by W. Hillebrandt, B. Leibundgut, ESO Astrophysics Symposia, p. 268. Springer, Berlin

Spergel, D. N., Verde, L., Peiris, H. V., Komatsu, E., Nolta, M. R., Bennett, C. L., Halpern, M., Hinshaw, G., Jarosik, N., Kogut, A., Limon, M., Meyer, S. S., Page, L., Tucker, G. S., Weiland, J. L., Wollack, E., Wright, E. L. (2003): First-Year Wilkinson Microwave Anisotropy Probe (WMAP) Observations: Determination of Cosmological Parameters, *ApJS*, **148**, 175

Stanishev, V. (2005): SN2003du. In preparation

Stehle, M. (2004): *Abundance Tomography of Type Ia Supernovae*. Ph.D. thesis, Ludwigs-Maximilians-Universität München

Stehle, M., Mazzali, P. A., Benetti, S., Hillebrandt, W. (2004): Abundance Tomography of Type Ia Supernovae: I. The Case of SN 2002bo, *ArXiv Astrophysics e-prints*, . astro-ph/0409342

Stephenson, F. R., Green, D. A. (2002): *Historical supernovae and their remnants, by F. Richard Stephenson and David A. Green. International series in astronomy and astrophysics, vol. 5. Oxford: Clarendon Press, 2002, ISBN 0198507666*

Suntzeff, N. B. (1996): Observations of Type Ia Supernovae. In *IAU Colloq. 145: Supernovae and Supernova Remnants*, p. 41

Sutherland, P. G., Wheeler, J. C. (1984): Models for Type I supernovae - Partially incinerated white dwarfs, *ApJ*, **280**, 282

Taresch, G., Kudritzki, R. P., Hurwitz, M., Bowyer, S., Pauldrach, A. W. A., Puls, J., Butler, K., Lennon, D. J., Haser, S. M. (1997): Quantitative analysis of the FUV, UV and optical spectrum of the O3 star HD 93129A, *A&A*, **321**, 531

Thielemann, F.-K., Nomoto, K., Yokoi, K. (1986): Explosive nucleosynthesis in carbon deflagration models of Type I supernovae, *A&A*, **158**, 17

Tonry, J. L., Schmidt, B. P., Barris, B., Candia, P., Challis, P., Clocchiatti, A., Coil, A. L., Filippenko, A. V., Garnavich, P., Hogan, C., Holland, S. T., Jha, S., Kirshner, R. P., Krisciunas, K., Leibundgut, B., Li, W., Matheson, T., Phillips, M. M., Riess, A. G., Schommer, R., Smith, R. C., Sollerman, J., Spyromilio, J., Stubbs, C. W., Suntzeff, N. B. (2003): Cosmological Results from High-z Supernovae, *ApJ*, **594**, 1

Travaglio, C., Hillebrandt, W., Reinecke, M., Thielemann, F.-K. (2004): Nucleosynthesis in multi-dimensional SN Ia explosions, *A&A*, **425**, 1029

Truran, J. W., Arnett, D., Cameron, A. G. W. (1967): Nucleosynthesis in supernova shock waves, *Canad. J. Physics*, **45(7)**, 2315

Tuli, J. K. (2000): *Nuclear Wallet Cards*. National Nuclear Data Center, Brookhaven National Laboratory, Upton, NY, USA. URL: `http://www.nndc.bnl.gov/wallet/`

Turatto, M., Benetti, S., Cappellaro, E., Danziger, I. J., della Valle, M., Gouiffes, C., Mazzali, P. A., Patat, F. (1996): The properties of the peculiar type IA supernova 1991bg. I. Analysis and discussion of two years of observations., *MNRAS*, **283**, 1

Unsöld, A. (1955): *Physik der Sternatmosphären, mit besonderer Berücksichtigung der Sonne*. Berlin, Springer, 1955. 2. Aufl.

Vacca, W. D., Leibundgut, B. (1996): The Rise Times and Bolometric Light Curve of SN 1994D: Constraints on Models of Type IA Supernovae, *ApJ*, **471**, L37

Webbink, R. F. (1984): Double white dwarfs as progenitors of R Coronae Borealis stars and Type I supernovae, *ApJ*, **277**, 355

Weinberg, S. (1989): The cosmological constant problem, *Reviews of Modern Physics*, **61**, 1

Wheeler, J. C., Benetti, S. (2000): *Supernovae*, chap. 18, pp. 451–469. AIP Press; Springer, New York, forth edn.

Wheeler, J. C., Harkness, R. P. (1990): Type I supernovae, *Reports of Progress in Physics*, **53**, 1467

Whelan, J., Iben, I. J. (1973): Binaries and Supernovae of Type I, *ApJ*, **186**, 1007

Wilson, O. C. (1939): Possible Applications of Supernovae to the Study of the Nebular Red Shifts, *ApJ*, **90**, 634

Woosley, S. E., Taam, R. E., Weaver, T. A. (1986): Models for Type I supernova. I - Detonations in white dwarfs, *ApJ*, **301**, 601

Woosley, S. E., Weaver, T. A. (1986): The physics of supernova explosions, *ARA&A*, **24**, 205

Woosley, S. E., Weaver, T. A. (1994): Sub-Chandrasekhar mass models for Type IA supernovae, *ApJ*, **423**, 371

Woosley, S. E., Wunsch, S., Kuhlen, M. (2004): Carbon Ignition in Type Ia Supernovae: An Analytic Model, *ApJ*, **607**, 921

Zwicky, F. (1939): On the Theory and Observation of Highly Collapsed Stars, *Physical Review*, **55**, 726

Acknowledgements

I would like to thank all the people who helped and supported me during the last few years. In particular, my special thanks go to my advisor Wolfgang Hillebrandt at the MPA, who not only shared his scientific expertise, but also provided the opportunity to work on this project, cultivated a great atmosphere at the MPA, and made it possible for me to meet many people in the supernova community. Special thanks also go to my advisor, Adi Pauldrach at the USM for providing the stellar atmosphere code, a challenging project, and the undying optimism needed to see it through. Our extensive discussions gave me a solid foundation concerning radiative transfer.

For many discussions about radiative transfer, computer problems, and many other things, my sincere thanks go to the rest of the hot-star group at USM: Joachim Puls, Keith Butler who shared his office and tea with me, Philip Hultzsch, and, in particular, Tadziu Hoffmann who was very often my unresting guide through the dark jungle of the transfer code. My special thanks also go to Paolo Mazzali, who not only shared his experience and knowledge of supernova physics, but also his enthusiasm for future projects.

At both institutes, many people contributed to the good atmosphere and supported my work. In addition to those mentioned above, I want to thank Tobias, Leonhard, Felix, Martin, Fritz, Matthias, Wolfram, Robi, Jens, Max, Jan, Gerti, and the lunch crew Arno, Andre, Michael, Marc, and Tamara. I am grateful to have excellent colleagues, many of whom have also become good friends.

In addition, there are many people beyond the physics world who made it possible for me to reach this point. Here, I especially want to thank my parents, Monika and Bernward, who supported and helped me all the way through my life, my sister Elizabeth and my brother Jonathan (who especially made the last weeks much easier). I also want to express my gratitude to Maria and Joachim for the inspirational afternoon teas. Thanks also to my friends, especially Deliah, Pätti, Sina and Levin, Katrin, Schüssel and Johanna, for the moral support, dinners, and distraction that was now and again necessary. I especially want to thank Sheridon, not only for prove-reading and many helpful comments, but especially for her unresting support, patience, and help in the last years. Thank you for believing in me.